Master's thesis

NTNU
Norwegian University of Science and Technology
Faculty of Natural Sciences
Department of Physics

Jenny Sandgren Østenstad

Multiphysical modeling of a next generation PEM electrolyser

Master's thesis in Applied Physics and Mathematics
Supervisor: Alejandro Oyarce Barnett (Hystar)
Co-supervisor: Michael Gerhardt (SINTEF), Jon Andreas Støvneng
July 2023

NTNU
Norwegian University of
Science and Technology

Jenny Sandgren Østenstad

Multiphysical modeling of a next generation PEM electrolyser

Master's thesis in Applied Physics and Mathematics
Supervisor: Alejandro Oyarce Barnett (Hystar)
Co-supervisor: Michael Gerhardt (SINTEF), Jon Andreas Støvneng
July 2023

Norwegian University of Science and Technology
Faculty of Natural Sciences
Department of Physics

NTNU
Norwegian University of
Science and Technology

Preface

The work on this thesis was carried out at the Norwegian University of Science and Technology (NTNU) under the supervision of Alejandro Oyarce Barnett[I], Michael Gerhardt[II] and Jon Andreas Støvneng[III].

The thesis is a continuation of the project thesis "Multiphysical modeling approaches for proton exchange membrane electrolysis" written in the fall of 2022, in which a comprehensive review of many of the available published PEM electrolyser models was performed with a basis in physics-based criteria for multiphysical modeling.

Modeling of the electrolysis process requires insight into a wide range of complex genres of physics and chemistry and their interplay, such as electrochemistry, fluid dynamics, thermodynamics, materials science, and various coupled transport mechanisms such as diffusion, electroosmosis, and advection. As such, emphasis has been placed not only on modeling of specific phenomena, but on developing a comprehensive physics based understanding of electrochemical systems as a whole.

I would like to express my gratitude towards my three supervisors for the opportunity to work on this project, and hope that this thesis will contribute to the advancement of electrochemical systems modeling, and to the development of sustainable hydrogen fuel systems. Further thanks are extended to the Norwegian Fuel Cell and Hydrogen Centre at SINTEF for experimental data, and to the creators and developers of FiPy at NIST for making their software publicly available.

Jenny Sandgren Østenstad
Trondheim, Norway
June 2023

[I] Hystar
[II] SINTEF
[III] NTNU

Disclaimer

As the thesis work is a continuation of the literature review performed in the project thesis of 2022, the present document contains selected chapters and excerpts from the project thesis.

Specifically, a considerable part of the introduction and theoretical foundations in chapter 2 was first presented in the project thesis, and is for the most part repeated. However, some modifications and added materials are included for completeness and to adjust the text to the focus of the master thesis. Furthermore, the analysis in chapter 3 relies on the material presented in the review, and while this chapter was written for the master thesis it may contain formulations and brief excerpts from the review.

Abstract

The utilization of hydrogen as an energy carrier is an important technology to satisfy the world's increasing energy demands in a non-carbonized way. A sustainable method to produce hydrogen is by electrolysis of water, however this field is presently lagging behind the field of hydrogen fuel cells. Computational modeling by a multiphysical approach provides the key to increased insight into processes within the electrolyser, and to accelerating development of new technology for a commercially viable green energy transition.

Comprehensive modeling frameworks have been developed for the field of proton exchange membrane (PEM) fuel cells, but are applied to highly varying degree in state of the art PEM electrolyser models. Such a framework is in this thesis applied in a computational model of a PEM electrolyser of a novel thin-membrane design. A model system for both steady-state and transient simulations is presented, and is implemented using open-source software in order to throw light on the applicability of the most accessible computational modeling tools to modeling of complex electrochemical systems.

The model is validated against in-house experimental data, and used to gain insights into phenomena internal to the electrolyser. Sensitivity studies of the impact of varying operational conditions on local phenomena such as water penetration and transport resistances are performed, and the system response to a sudden step perturbation is simulated.

Sammendrag

Anvendelse av hydrogen som energibærer er en viktig teknologi for å møte verdens økende energibehov på en måte frigjort fra karbon. Elektrolyse av vann er en bærekraftig metode å produsere hydrogen på, men fagfeltet ligger foreløpig bak i forhold til hydrogen-brenselceller. Modellering med en multifysisk tilnærming er nøkkelen til økt innsikt i prosesser som foregår inni elektrolysecellen, og til å akselerere forskning på ny teknologi for et kommersielt levedyktig grønt skifte.

Omfattende rammeverk for modellering er utviklet for proton exchange-membran-(PEM)-brenselceller, men er anvendt i varierende grad i eksisterende PEM-elektrolysemodeller. Et slikt rammeverk blir i denne avhandlingen anvendt i en modell av en ny type PEM-electrolysecelle med tynnere membran. En modell for elektrolysecellen under både steady-state og dynamisk drift blir presentert, og implemenert ved bruk av utelukkende open-source-programvare for å belyse anvendbarheten av åpent tilgjengelige modelleringsverktøy til modellering av komplekse elektrokjemiske systemer.

Modellen valideres mot interne eksperimentelle data, og brukes til å oppnå innsikt i interne fenomen i elektrolysecellen. Sensitivitetsstudier gjennomføres for virkningen av varierende driftsparametre på lokale fenomen som vanngjennomtrengning og motstand mot transport, og systemrespons på en step-perturbasjon simuleres.

Contents

List of Figures

List of Tables

Chapter 1

Introduction

One of the most promising solutions to meet the world's increasing energy demands in a sustainable, non-hydrocarbon-based way is the utilization of hydrogen as an energy bearer. Recently, hydrogen has been gaining momentum, with emerging potential hydrogen based technology in aviation, shipping, industry and transport. Demand is projected to reach unprecedented heights in the course of the next decade, from 94 Mt in 2021 to around 180 Mt by 2030. [12]

The greenest, most environmentally friendly way to produce hydrogen is by electrolysis of water using renewable sources of energy. Several methods exist for electrolysis of water, and this thesis will focus on proton exchange membrane (PEM) water electrolysers. In the general water electrolysis process, water is split into hydrogen and oxygen in an electrolysis cell, or a stack consisting of multiple cells, and the hydrogen is stored for later use in e.g. a hydrogen fuel cell.

Computational modeling of electrolyser operation is one of the most important ways to further research and development, as it can be difficult or even impossible to experimentally measure processes within the electrolyser affecting operation and efficiency. Computational models provide a means of diagnostics for where and why efficiency is lost, predicting operation upon component and material modifications or replacements, increasing system lifetime by minimizing component degradation, and optimizing operational conditions, based on physical understanding of processes in the electrolyser. PEM electrolysers are especially interesting as a means of energy storage for intermittent renewable energy sources, adding further complexity to modeling as a transient model allowing for variable operational conditions is then required.

Hydrogen fuel cells have been in commercial use since the 1930s, and the field is thoroughly researched both with regards to technology and modeling. The similar but reversed process of hydrogen production by water electrolysis however, has seen far less research, with the first PEM electrolyser developed in the late 1960s to early 70s [58] and the first modeling paper being published as late as 2002. [63] The rate of publication of new modeling papers has lately gained momentum, however only a select few actually model the internal phenomena necessary to provide the aforementioned diagnostics. Progress in the field of computational modeling of electrolyser operation in the near future is thus a prerequisite for accelerating the rate of development and improvement of electrolysis technology, for the demand for hydrogen to be met.

The baseline for this thesis, describing the development of a computational PEM electrolyser model, will be the argument that computational modeling of the complex electrolysis process requires treatment rooted in multiphysics, i.e. simulation of the many simultaneous and coupled interdisciplinary phenomena [45] that occur within the electrolyser and affect its performance. Such treatment has been thoroughly developed for PEM fuel cells, and has recently begun to see more application to electrolysers. With inspiration from fuel cell models, the concepts are applied in this thesis to a 1D multiphysical computational model of a novel thin-membrane cathode-feed PEM electrolyser. Furthermore, the model is developed using exclusively open-source software in order to examine the limitations of currently available software for modeling of complex electrochemical systems.

In chapter 2, key thermodynamcial and electrochemical foundations for understanding the complex processes occurring within the electrolyser are presented, and their application to specific electrolyser components according to their structure and properties is discussed. Chapter 3 presents an analysis of the state of the art of PEM electrolysis modeling, in which various approaches are discussed with respect to each other and to the theoretical foundations. Key takeaways from the two chapters serve as a foundation for the development of a computational model in chapter 4, where a modeling framework for both a steady-state and transient model is described.

Modeling is performed for both steady-state and dynamic electrolyser operation. The computational model is first validated against experimental data for the steady-state case, and steady-state model behavior in terms of local operating conditions under varying operating conditions is studied. Then, simulation is performed for a small discrete step perturbation to the operating current, in order to examine the system response.

Chapter 2

Physical, thermodynamical, and electrochemical foundations

The PEM electrolyser is a complex electrochemical reactor in which many physical phenomena occur, such as chemical reactions, absorption and desorption, and various coupled transport phenomena such as transport of charge, heat and mass. Additionally, these phenomena are dynamic multiphase phenomena occurring at length scales ranging from the nm to m scale, and different time scales ranging from the µs to s scale. The advanced and highly coupled physical nature of the system makes computational modeling of the process complex and computationally expensive.

In the last decade, some thorough PEM electrolysis reviews have been published that warrant a mention: a comprehensive review by Carmo et al. [15] focusing on the state of the art and research needs of PEM electrolysis technology itself, including a chapter on modeling; a thorough review on low-temperature electrolysis systems modeling by Olivier et al., [62]; and a modeling review by Falcão & Pinto [22] aimed at providing guidelines for beginners in the field. In the latter, the authors remark that while the two former are of great importance to the research community, a comprehensive theoretical description of the operational principles of PEM electrolysers is lacking.

The theoretical material presented in these reviews consists mainly of empirical relations, while advanced phenomena such as dynamic behaviour and multiphase flow are discussed purely conceptually. While sufficient for beginners and simple models for systems engineering purposes, a more thorough representation of the physical processes involved is required to achieve the complexity and predictive qualities necessary for research and development purposes.

In this chapter the theoretical foundations for understanding PEM electrolyser operation are presented in greater detail, to provide a solid foundation upon which to evaluate existing published models, as well as for developing new multiphysical models. An introduction is given to the basics of the process of water electrolysis, and thermodynamics and general conservation laws are presented. Particular consideration is then given to central components of the PEM electrolyser, wherein application of the presented theory to relevant phenomena in each component is discussed.

2.1 Hydrogen production by PEM water electrolysis

Hydrogen production by PEM electrolysis is based on the principle that an applied voltage splits water into hydrogen and oxygen following the reaction equation

$$\mathrm{H_2O} \longrightarrow \mathrm{H_2} + \frac{1}{2}\mathrm{O_2} \quad \text{(cell)}, \tag{2.1}$$

resulting from the combined cathode and anode half-reaction equations

$$\mathrm{H_2O} \longrightarrow 2\mathrm{H^+} + 2\mathrm{e^-} + \frac{1}{2}\mathrm{O_2} \quad \text{(anode)}, \tag{2.2}$$

$$2\mathrm{H^+} + 2\mathrm{e^-} \longrightarrow \mathrm{H_2} \quad \text{(cathode)}. \tag{2.3}$$

A state of the art PEM electrolyser cell consists of a sandwich setup, as shown in figure 2.1. The center of the cell is the solid polymer electrolyte (SPE) PEM which is permeable to protons. Adjacent to the membrane on either side is a thin porous catalyst layer (CL), usually deposited directly onto the membrane. The membrane-catalyst sandwich is termed the membrane electrode assembly (MEA), and is often referred to as a catalyst-coated membrane (CCM) or catalyst-coated substrate (CCS), depending on the method of deposition of the CLs. [36] On each side there is then a porous transport layer (PTL) which connects the MEA to the bipolar plates (BPP) separating the individual cells in a stack. The term current collector (CC) is often used interchangeably with porous transport layer in literature. To ensure good contact between the CL and PTL, which consist of particles of different length scales (nano- and micro-scale, respectively), a layer known as a micro-porous layer (MPL) is often added to smooth the transition. Water can be fed to the electrolyser either on the anode or cathode side, in liquid or vapor form, with anode liquid feed being the most common as this is the side where water is consumed in the electrolyser. [15]

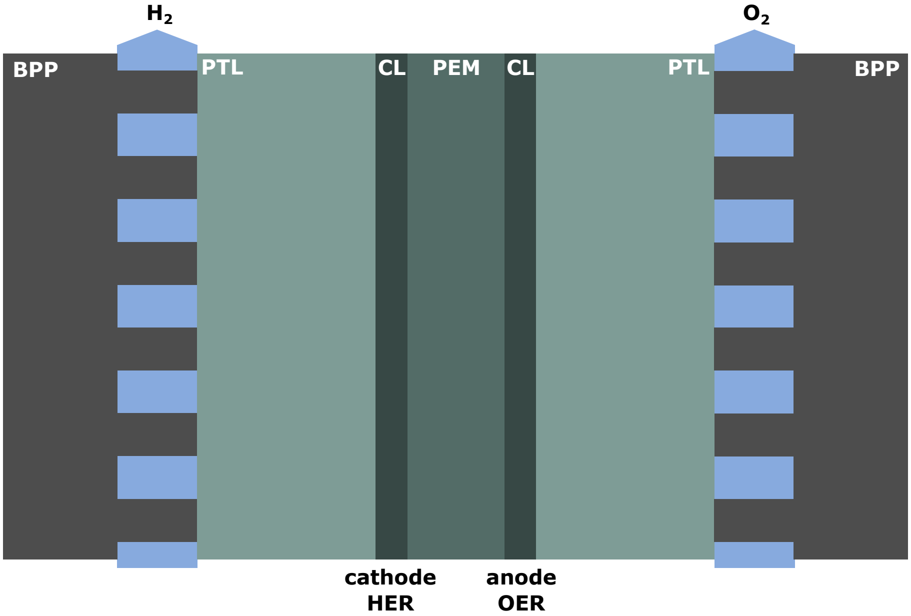

Figure 2.1: Schematic of the components of a typical PEM electrolyser (not to scale). The components of the electrolyser are indicated with their abbreviations, as well as the reactions taking place on each electrode and produced gas flows out of the cell.

The anode and cathode reactions are termed the oxygen evolution reaction (OER) and the hydrogen evolution reaction (HER) respectively, and take place on the membrane-catalyst boundaries. At the anode water is split into protons, electrons and oxygen gas. The protons travel through the membrane, the electrons travel through an external circuit, and the oxygen gas is transported out of the cell with the flow field in the anode BPP. The protons travelling through the membrane cause a flux of water molecules through the membrane, an effect known as electroosmotic drag, [13] increasing the water concentration towards the cathode. The electroosmotic flux, combined with the decrease in water concentration resulting from consumption of water by the OER at the anode, gives rise to a water concentration gradient which causes diffusion of water back to the anode side. On the cathode side, protons are reunited with electrons to form hydrogen gas, which is led out of the cell by the flow field. Since the membrane is permeable to gas, there is also some crossover of hydrogen from the cathode to the anode, and of oxygen from the anode to the cathode.

The PEM electrolyser has advantages compared to other electrolysis technologies related to its thin SPE membrane, which with its structural integrity allows for simultaneously durable and compact system design allowing for high pressure operation. The solid electrolyte impedes diffusion of the produced gases through the membrane, yielding high purity hydrogen and alleviating issues of potentially explosive hydrogen-oxygen mixtures.

Although it is a promising technology, PEM electrolysis has several challenges which must be overcome by researchers in order to achieve widespread commercial viability. One significant challenge is that the pressure gradient of high pressure operation results in increased crossover of hydrogen to the anode, which can, if the concentration is high enough, result in an explosive mixture with oxygen. To alleviate the issue of crossover, thicker membranes or added fillers to the membrane are often introduced, both resulting in higher ohmic resistance and thus negating the advantages which are desirable to keep in a PEM electrolyser. [15]

Product gas crossover also leads to increased rate of degradation, by reacting to form corrosive hydrogen peroxide. [16] Studies have demonstrated that hydrogen peroxide formation is more prevalent on the cathode side due to oxygen crossover, than on the anode side due to hydrogen crossover. [16, 40]

Another challenge is the corrosive regime produced by the PEM, requiring the use of materials with not only satisfactory properties for their intended function, but also a resilience to low pH and high applied voltage, in the PEM-adjacent components. [15] Such materials are rare and expensive, accounting for a major part of production costs, thus making hydrogen an expensive and inaccessible fuel.

A common method for comparison of one electrolyser to another is to compare of the polarization curves of the electrolysers. A polarization curve gives the relation between current density and voltage loss of the electrolyser, and can be viewed as a global indication of efficiency and overall health of the electrolyser. It can be easily measured with an experimental setup, by measuring the voltage loss in the membrane for a given applied current or vice versa, and by comparison to polarization curves for other electrolyser setups it can be readily seen which is the better performing electrolyser.

2.2 Thermodynamics

The open circuit voltage of the electrolyser is the voltage necessary to operate under reversible, i.e. ideal, non-dissipative, conditions. The open circuit voltage is related to the Gibbs energy of the electrolysis process by

$$E_h = -\frac{\Delta G_h}{n_h F}, \tag{2.4}$$

where E is the open circuit voltage of reaction h, n is the number of electrons transferred in the reaction, and F is the Faraday constant. ΔG is the electrode reaction Gibbs energy

$$\Delta G_h = \Delta H_h - T\Delta S_h, \tag{2.5}$$

where H is the molar enthalpy and S the molar entropy of the reaction, and T is the temperature. As operational conditions of electrolysers can vary greatly from standard conditions with regards to e.g. temperature and pressure, it is common to use a Nernst equation for the reversible cell voltage [11]

$$E_h = E_{0,h} + \frac{RT}{n_h F} \ln \left(\prod_{\text{reactants}} a_h^{\nu_h} \prod_{\text{products}} a_h^{-\nu_h} \right), \tag{2.6}$$

which gives a measure of the open circuit voltage in non-standard conditions in terms of the activities of the reactants and products. R is the molar gas constant,

a represents the activities of the species and ν the stochiometric coefficients. The subscript 0 denotes standard state conditions, reactants are the reacting species, and products the species produced by reaction h.

Additional voltage losses in the cell occur due to irreversibilities, and efforts to reduce the energy consumption of the electrolyser involve mitigating measures for these losses. The irreversible losses are associated with, and implicitly defined by, the many complex processes in the electrolyser, and it is therefore difficult to interpret unambiguously exactly where and why these losses occur. [27] Mathematically and physically, these processes can be described using conservation laws and balance equations that are presented in the following.

2.3 Conserved quantities

Modeling the various components with a basis in relevant physical processes requires knowledge of electrochemical kinetics, thermo- and fluid dynamics, and conservation laws at play, while further complexity is added by the determination of boundary conditions, effective properties, and related transfer equations. [82] General mathematical descriptions of conservation and transport equations for mass, charge, momentum and energy were derived by Weber & Newman [83] and Weber et al. [82] for hydrogen fuel cells, and can be adapted to electrolysers. Their derivations are summarized in the remainder of the current section, while comprehensive treatment can be found in Weber et al.. [82]

The conservation equations take the general form

$$\frac{\partial \psi}{\partial t} = -\nabla \cdot \boldsymbol{N}_{\psi} + S_{\psi} \tag{2.7}$$

where ψ represents the property, $\boldsymbol{N}_{\psi}$ is the flux of ψ, and S_{ψ} is a source term representing generation or consumption. For steady-state models the left hand side term is zero, as there is no transient variation of the property. The remaining terms on the right hand side represents the change in the property due to the divergence of its flux through the domain, and sources or sinks of the property including reactions, phase-change terms, and coupling to other conservation equations.

2.3.1 Conservation of mass

The conservation balance of chemical species must be determined for each component i in each thermodynamic phase k, and can be written on a general form as

$$\frac{\partial\left(\varepsilon_k c_{i,k}\right)}{\partial t} = -\nabla \cdot \boldsymbol{N}_{i,k} + S_{i,k}, \tag{2.8}$$

where ε is the volume fraction of phase k, c is the concentration of species i, and the source term consists of contributions from reactions producing or consuming the species

$$S_{i,k} = -\sum_h \mathsf{a}_{1,k}\nu_{i,k,h}\frac{i_{h,1\to k}}{n_h F} + \sum_l \nu_{i,k,l}\sum_{p\neq k}\mathsf{a}_{k,p}\mathsf{r}_{l,k\to p} + \sum_g \nu_{i,k,g}\varepsilon_k\mathcal{R}_{g,k}. \tag{2.9}$$

Here, a is the volumetric interfacial surface area between the electron conducting phase and phase k, i is the reaction transfer current density from the electron conducting phase to phase k, r is the interfacial area reaction rate and $\mathcal{R}$ is the homogeneous reaction rate.

To solve equation (2.8) an equation for the species flux $\boldsymbol{N}$ is required. Two cases are often considered in order to determine the correct form of $\boldsymbol{N}$, namely the dilute-solution case where interpecies interactions are considered negligible, and the concentrated-solution case that takes into account interactions between the species present. In the case that interspecies interactions are not of importance, i.e. dilute-solution theory applies, species flux can be represented by interactions with the solvent only. A diffusion flux according to Fick's law combined with advective flux gives

$$\boldsymbol{N}_{i,k} = -\varepsilon_k D_i \nabla c_{i,k} + c_{i,k}\boldsymbol{v}_k, \tag{2.10}$$

where the first term on the right hand side represents diffusion down the species' concentration gradient in the solvent proportional to a diffusion coefficient D, and the second term represents particles carried by the solvent flow with velocity $\boldsymbol{v}$. If, however, interactions are to be taken into consideration, i.e. concentrated-solution theory applies, the multicomponent Stefan-Maxwell equation which implicitly defines the species flux [81]

$$\nabla x_{i,k} = -\frac{x_{i,k}}{RT}\left(\bar{V}_i - \frac{\bar{M}_i}{\rho_k}\right)\nabla p_k + \sum_{j\neq i} \frac{x_{i,k}\boldsymbol{N}_{j,k} - x_{j,k}\boldsymbol{N}_{i,k}}{\varepsilon_k c_{T,k} D_{i,j}} - \frac{\boldsymbol{N}_{i,k}}{\varepsilon_k c_{T,k} D_{K_i}} \tag{2.11}$$

can be used to account for binary interactions between species. Here, x is the mole fraction, $\bar{V}$ is the species partial molar volume, and M is the molar mass of species i, and ρ is the density, and p is the pressure of phase k.

If there can be assumed to be no accumulation or chemical reactions involving the species, a mass balance yields [84]

$$\sum_k \nabla \cdot \boldsymbol{N}_{i,k} = 0, \tag{2.12}$$

a common assumption in modeling which greatly simplifies the governing equations and complexity of the problem.

2.3.2 Conservation of charge

The general mass conservation principle is also applicable to the subgroup of charged species. As all reactions are charge balanced, the general charge balance becomes

$$\frac{\partial \rho_\mathrm{e}}{\partial t} = -\nabla \cdot \sum_k \boldsymbol{i}_k, \tag{2.13}$$

where ρ_e is the volumetric charge density defined as

$$\rho_\mathrm{e} = F \sum_k \varepsilon_k \sum_i z_i c_{i,k}, \tag{2.14}$$

and the current density $\boldsymbol{i}$ is equal to the electrical charge carried by the flux of each charged species, proportional to its charge number z,

$$\boldsymbol{i}_k = F \sum_i z_i \boldsymbol{N}_{i,k}. \tag{2.15}$$

In most cases, the basis for modeling of charge conservation is the physical assumption that there is no accumulation of charge in the electrolyser. The balance in equation (2.13) then simplifies to

$$\sum_k \nabla \cdot \boldsymbol{i}_k = 0. \tag{2.16}$$

Similarly to equation (2.12), equation (2.16) is a common simplification which greatly simplifies modeling efforts. For domains or processes where electroneutrality cannot be assumed, such as double layer charging, charge conservation is given by Poisson's equation

$$\nabla^2 \Phi = -\frac{\rho_\mathrm{e}}{\epsilon_0}, \tag{2.17}$$

where Φ denotes the electric potential and ϵ the permittivity, or dielectric constant, of the medium.

Again, either dilute-solution or concentrated-solution theory may be used to obtain the charged species transport equations. For the dilute-solution approach, which does not account for intermolecular interactions, the Nernst-Planck equation

$$\boldsymbol{N}_{i,k} = -z_i u_{i,k} \varepsilon_k F c_{i,k} \nabla \Phi_k - \varepsilon_k D_i \nabla c_{i,k} + c_{i,k} \boldsymbol{v}_k \tag{2.18}$$

may be combined with the definition of current density in equation (2.15) to obtain

$$\boldsymbol{i}_k = -\kappa_k \nabla \Phi_k - F \sum_i z_i \varepsilon_k D_i \nabla c_{i,k}. \tag{2.19}$$

In equation (2.18) u denotes mobility, and in equation (2.19) κ is the ionic conductivity. The Nernst-Planck equation (2.18) is an extension of Fick's law of diffusion for charged species, that additionally describes diffusion due to electrostatic forces with respect to the solvent.

For the concentrated-solution approach, binary interactions between the species are taken into consideration. Introducing the chemical potential μ accounting for both migration and diffusion, the flux equation becomes

$$\boldsymbol{N}_{i,k} = -\frac{D_{i,0}}{RT} c_{i,k} \nabla \mu_{i,k} + c_{i,k} \boldsymbol{v}_0. \tag{2.20}$$

2.3.3 Conservation of momentum

Assuming that the reactants and products can be described as Newtonian fluids, conservation of momentum can be expressed with the Navier-Stokes equation

$$\frac{\partial\left(\rho_k \boldsymbol{v}_k\right)}{\partial t} + \boldsymbol{v}_k \cdot \nabla\left(\rho_k \boldsymbol{v}_k\right) = -\nabla p_k + \upmu_k \nabla^2 \boldsymbol{v}_k + S_m, \tag{2.21}$$

where the kinematic viscosity $\upmu$ must not be confused with the chemical potential μ. Typical momentum sources include gravitational or magnetic body forces, and are often considered to be negligible.

Another way of obtaining a conservation equation is by considering Darcy's law for flow in porous materials and multiphase flow,

$$\boldsymbol{v}_k = -\frac{k_k}{\upmu_k}\nabla p_k, \tag{2.22}$$

where k is the effective hydraulic permeability. Combined with the material balance in equation (2.8), equation (2.22) gives

$$\frac{\partial\left(\rho_k \varepsilon_k\right)}{\partial t} = \nabla \cdot \left(-\rho_k \frac{k_k}{\upmu_k}\nabla p_k\right) + S_m. \tag{2.23}$$

2.3.4 Conservation of energy

General conservation of thermal energy in the electrolyser is given by

$$\begin{aligned}\rho_k \bar{C}_{p_k,k}\left(\frac{\partial T_k}{\partial t} + \boldsymbol{v}_k \cdot \nabla T_k\right) + \left(\frac{\partial \ln \rho_k}{\partial \ln T_k}\right)_{p_k, x_{i,k}}\left(\frac{\partial p_k}{\partial t} + \boldsymbol{v}_k \cdot \nabla p_k\right) = \\ Q_{k\rightarrow p} - \nabla \cdot \boldsymbol{q}_k - \boldsymbol{\tau} : \nabla \boldsymbol{v}_k + \sum_i \bar{H}_{i,k}\left(\nabla \cdot \boldsymbol{J}_{i,k} - \Re_{i,k}\right),\end{aligned} \tag{2.24}$$

where $\bar{C}$ is the heat capacity, Q is the heat flux transferred between phases k and p, $\boldsymbol{q}$ is the superficial heat flux, $\boldsymbol{\tau}$ is the viscous stress tensor, $\bar{H}$ is the partial molar enthalpy, $\boldsymbol{J}$ is a flux density and $\Re$ is the total reaction rate. The first term on the left hand side represents accumulation of enthalpy and convective enthalpy transport, and the second term represents the energy due to reversible work and is negligible. [82] On the right hand side, the first two terms represent interphase transfer and conduction of heat, the third represents heat generation by viscous forces, and the fourth term represents the change in enthalpy due to diffusion and reactions in the electrolyser. Assuming local equilibrium, equation (2.24) can be written

$$\sum_k \rho_k \bar{C}_{p_k,k} \frac{\partial T}{\partial t} = -\sum_k \rho_k \bar{C}_{p_k,k} \boldsymbol{v}_k \cdot \nabla T + \nabla \cdot (k_T \nabla T) - \boldsymbol{i}_k \cdot \nabla \Phi + \sum_h i_h \left(\eta_h + \Pi_h\right) - \sum_h \Delta H_h \mathsf{r}_h, \tag{2.25}$$

where there is no longer any phase dependence of the temperature. In equation (2.25), k_T is the thermal conductivity, η is the electrode overpotential, and Π is the Peltier coefficient. The first and second terms on the right hand side describe energy transport due to convection and thermal conduction, the third and fourth terms represent ohmic and reaction heating, and the fifth term represents bulk reactions, e.g. phase changes. Heat lost to surroundings should be included at the boundaries of the cell.

2.4 Component-specific considerations

The general concepts described above are applied to varying degree in published electrolyser modeling efforts. Implementing them all in their complete form is however time-consuming, complex, and computationally costly. Thus, the set of equations is usually simplified in their application to the specific focus area under consideration, by making assumptions deemed appropriate by the authors. For accurate computational representation, and justifying the simplifications of the problem, a thorough knowledge of what physical, electrochemical and thermal effects are prevalent in each cell component, and how they interact, is required.

In this section, three components governing important aspects of PEM electrolyser performance, namely the membrane, CLs and PTLs, will be discussed in light of the material presented in sections 2.2 and 2.3 to identify the principles that should be considered. The identified phenomena will further be used as a framework for evaluating published models and for creating a computational model in parts 3 and 4.

The PEM, CLs, and PTLs all generally consist of porous media. Studies have linked the degree of hydration of these types of media to important phenomena such as conductivity/resistivity, distribution uniformities, deformation, and interfacial contact, [72] all of which impact the performance of the electrolyser.

There are many possible approaches for modeling of porous media, varying from macro- to atom-scale, continuum- or discrete-particle-based, volume-averaged or geometry-resolved models. A common feature of macroscopic models is that properties and transport are volume-averaged, while microscale (and smaller-scale) models rely on a numerical reconstruction of the geometry of the porous micro-structure itself, making use of numerical methods such as the lattice Boltzmann and kinetic Monte Carlo method, as well as incorporating elements from other fields such as quantum mechanics and molecular dynamics. [75]

In the following, some detail on macroscopic methods for modeling of the PEM, CLs and PTLs will be provided. Some model types falling under the category of macroscopic as defined above are porous electrode and agglomerate models, [75] which shall be discussed further later in the chapter. Details on microscopic methods are considered outside the scope of the thesis, however Sui et al. [75] give a rather comprehensive introduction to several methods along with further references.

2.4.1 Proton exchange membrane

The PEM is at the heart of the electrolyser, and thus of great importance in computational modeling of electrolyser performance. The PEM is responsible for many of the advantages associated with PEM electrolysis, such as high structural integrity even at elevated pressures, low gas permeability resulting in high purity hydrogen, and a wide range of possible power input. [77] Important phenomena in the PEM include multi-phase transport of water, transport of protons, diffusion of produced hydrogen and oxygen gas, heat generation and transport, and degradation as a result of corrosive chemical reactions. Degradation phenomena are discussed in section 2.4.4.

Penetration of water in the membrane can be quantified in various ways, e.g. the saturation (the fraction of pores filled with liquid water, often denoted S) or water content (water molecules per sulfonic acid group, often denoted λ) are commonly used. Furthermore, a phenomenon known as Schroeder's paradox is known to occur, in which a PEM is more hydrated in contact with liquid water than with fully saturated water vapor under otherwise the same conditions. [78]

Transport of water and protons in the membrane is coupled, and may occur as a result of several driving forces: Concentration gradients giving rise to diffusive transport, and pressure gradients giving rise to pressure-driven transport, and electroosmotic driving forces, where the moving protons bond to water molecules, giving rise to a flux of water.

The most popular type of PEM for electrolysers are perfluorinated sulfonic acid (PFSA) Nafion membranes. [77] Weber & Newman [85] cite experimental evidence that the PFSA membrane consists of an ionic electrolyte phase with fixed, negatively charged, sulfonic acid sites and a non-ionic polymer matrix phase that provides structure and integrity. Some also consider a third interfacial phase. [69, 70, 90] At low hydration the ionic electrolyte phase is assumed to take the form of inverted micelles, while at increasing hydration the clusters reorganize resulting in an agglomerate porous structure with larger pore size. [85]

The membrane is assumed to be electroneutral on the macro scale, and there is no accumulation or reactions involving water in the membrane. Thus, the charge balance in equation (2.16) applies for the flux of protons, and the mass balance in equation (2.12) applies for the flux of water. Due to interactions between the various species present, transport in the membrane should be described using concentrated-solution theory.

In addition to water and protons, some of the produced gas travels through the membrane instead of out to the flow field as a result of the diffusion and advective electroosmotic flow. Gas transport is reported to increase with membrane saturation, as the permeabilities of the gases are significantly larger in water than in the dry membrane. [70] When hydrogen gas reaches the anode it is usually assumed to either be oxidised back into protons leading to a parasitic proton current, or it enters the stream together with the produced oxygen gas. Oxygen gas that reaches the cathode is often assumed to be reduced back to water, travel out of the cell with the stream, or enter into corrosive reactions. A model investigating one or more of these phenomena will often consider the "worst case" scenario of maximum possible crossover, degradation or hydrogen stream contamination, and neglect the other phenomena.

2.4.2 Catalyst layers

The electrode reactions in the electrolyser occur in the CLs, which are generally porous electrodes consisting of an electron conducting phase (matrix) with interconnected pores partially filled with an ion conducting phase (electrolyte), as is shown in figure 2.2. The thermodynamic potential of electrolysis following equation (2.1) is 1.23 V, but due to high activation overpotentials needed to form intermediates at the electrode surface, an additional overpotential is needed. [77] The catalyst lowers the activation overpotentials necessary to drive the reactions. The solid structure of the CLs may include both non-conducting reactive and electron conducting materials, and the porous structure gives a larger available catalyst surface area for the electrode reactions. As water and gas flow through the porous electrodes, there is a three-phase boundary between the solid electrolyte and water-gas mixture.

The CLs are especially challenging to model as they combine all the phenomena occurring in the electrolyser: multi-phase mass and charge transport, electrochemical reactions, phase equilibria, thermal energy transport, and degradation. Macroscopic modeling methods are well developed in fuel cell literature, where e.g. porous electrode, pore network, and pore agglomerate models can be found. [51, 88, 89] Porous electrode theory is described below. Pore network models assume a porous geometric structure consisting of a network of pores connected by throats. [42] Pore agglomerate models include the matrix agglomerate structure as well as the electrolytic ionomer. [51] Methods such as the three mentioned here are advantageous since they, though they are based on volume averages, allow for a spatial distribution of

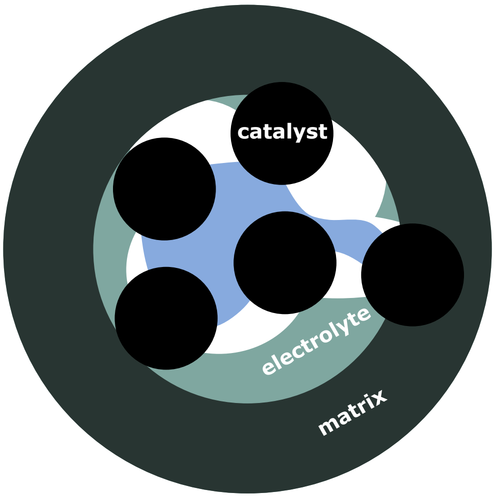

Figure 2.2: Generalized porous electrode principle. The electrode consists of a porous electron conducting phase (matrix), where the pore is filled with a proton conducting phase (electrolyte) and distributed catalyst particles. On the anode, the water stream flows through the pores and reacts on the catalyst sites. Protons then travel in the ion conducting phase to the membrane, electrons travel through the electron conducting phase, and the produced oxygen gas travels back through the pores and out with the stream. On the cathode, protons and electrons meet on the three-phase catalyst/ion conducting/electron conducting phase interface and react to form hydrogen gas on the catalyst sites, which then travels out through the pores. Figure adapted from Xing, 2018 [88].

reactions within the volume of the CL, and by incorporating experimental porosity data, examination of species transport and interactions within specific materials can be achieved.

Porous electrode theory is a large and complex scientific field. The derivations found in this section are based on Newman & Thomas-Alyea [54] and Newman & Tiedemann [56], and describes the central principles, mechanisms and governing equations for mass and charge transfer, as well as double layer charging. The first challenge in modeling the porous electrodes lies in describing physical properties of the specific electrode in terms of relevant and measurable parameters, as these have a large impact on the rate of the reactions on the electrode surface. Examples of parameters that are often used are porosity, average volumetric surface area, and volumetric resistivity. Averages should be taken at appropriate length scales compared to both the pore structure and geometry of the electrode. [54]

In porous electrode theory, the CLs are considered to consist of two phases – an electron conducting solid matrix, here denoted with subscript 1 following the practice of Newman & Tiedemann [56] and others [9, 54, 82, 91], and an ion conducting electrolyte filling the pores, denoted with subscript 2. The phases are assumed to coexist at each point in space.

The flux of each species in each phase is determined by the net rate of reaction producing or consuming the species in question, which can be described by Faraday's law in terms of the transfer current density i and the stochiometry of the reaction equation,

$$\boldsymbol{N}_{i,k} = \sum_h \nu_{i,k,h} \frac{i_h}{n_h F}. \tag{2.26}$$

Charge conservation dictates that any charge leaving the matrix phase must enter the electrolyte phase and vice versa, so that

$$\nabla \cdot \boldsymbol{i}_1 + \nabla \cdot \boldsymbol{i}_2 = 0. \tag{2.27}$$

Furthermore, the rate of charge exchange between the phases must be equal to the volumetric charge transfer density $i_{h,1\to 2}$,

$$\nabla \cdot \boldsymbol{i}_1 = -\nabla \cdot \boldsymbol{i}_2 = -i_{h,1\to 2} = -\mathsf{a}_{1,2} i_h. \tag{2.28}$$

As the matrix phase is assumed to hold no water and be conductive only to electrons, [54, 56] Ohm's law holds as a transport equation for the matrix phase, with an electronic conductivity σ,

$$\boldsymbol{i}_1 = -\sigma \nabla \Phi_1. \tag{2.29}$$

Equations (2.28) and (2.29) may be combined to produce a charge conservation equation for the matrix phase providing double layer charging can be neglected,

$$\nabla \cdot (-\sigma \nabla \Phi_1) = -i_{h,1\to 2}. \tag{2.30}$$

The electrolyte is permeable to water and conductive to protons, so by comparison to the mass conservation equation (2.8) and the source term (2.9), the conservation equation for the electrolyte phase becomes

$$\frac{\partial\left(\varepsilon_2 c_{i,2}\right)}{\partial t} = -\nabla\cdot\boldsymbol{N}_{i,2} - \frac{\nu_{i,2,h}}{n_h F}\nabla\cdot\boldsymbol{i}_2, \tag{2.31}$$

where the second term on the right hand side takes the form of a source term describing consumption or production of species i by the chemical reaction on either electrode.

The rate of reaction on the electrode surface, and thus the transfer current, is a strong non-linear function of potential, [11] and in order to model the electrochemical kinetics there is a need to express this dependence mathematically. A range of different approaches for expressing the transfer current density exist in terms of the potential, often expressed by the electrode overpotential. With reference electrode chosen such that the reference is exposed to the reaction site conditions, the electrode surface overpotential is [82]

$$\eta_h = \Phi_1 - \Phi_2 - E_h, \tag{2.32}$$

where the Φ are the electrostatic potentials of each phase, and E_h is the reaction activation potential relative to surface conditions.

In the low-current case the current is mainly determined by interfacial dynamics, with little dependence on mass transport. For low surface overpotentials, a linear approximation of the transfer current density is valid, [55]

$$i_h = i_{0,h}\frac{\left(\alpha_\mathrm{a}+\alpha_\mathrm{c}\right)F}{RT}\eta_h, \tag{2.33}$$

where α are anodic and cathodic charge transfer coefficients and $i_{0,h}$ is the reference transfer current density for reaction h, equal to the charge transfer rate at standard state, [10] and analogous to a rate constant. $i_{0,h}$ is also commonly referred to as the exchange current density. In fact, i_0 can be defined with a power-law dependence on the rate constants of the electrode reactions, [14]

$$i_{0,h} = n_h F k_\mathrm{a}^{\alpha_\mathrm{a}} k_\mathrm{c}^{\alpha_\mathrm{c}} \prod_{\substack{i\\ \text{reactants}}}^{\text{anode}} \left(a_i\right)^{\nu_{i,2,h}\left(\alpha_\mathrm{a}\right)} \prod_{\substack{i\\ \text{products}}}^{\text{cathode}} \left(a_i\right)^{\nu_{i,2,h}\left(\alpha_\mathrm{c}\right)}, \tag{2.34}$$

where k_a and k_c are rate constants of the anodic and cathodic direction, respectively.

Another common way of expressing the charge transfer coefficients α_{a} and α_{c} is through a symmetry factor β

$$\alpha_{\mathrm{a}} = n_h \beta, \qquad \alpha_{\mathrm{c}} = n_h (1 - \beta) . \tag{2.35}$$

A Tafel equation (a and b are here arbitrary constants)

$$\eta_h = a + b \log i_h \tag{2.36}$$

has been found to provide a wide ranger of validity, [11] while another common approach is to use the semi-empirical Butler-Volmer equation [82]

$$\dot{i}_h = \dot{i}_{0,h} \left(\exp\left[\frac{\alpha_{\mathrm{a}} F}{RT} \eta_h \right] \prod_{\substack{i \\ \text{anode}}} \left(\frac{a_i}{a_i^{\mathrm{ref}}} \right)^{\nu_{i,2,h}} - \exp\left[\frac{\alpha_{\mathrm{c}} F}{RT} \eta_h \right] \prod_{\substack{i \\ \text{cathode}}} \left(\frac{a_i}{a_i^{\mathrm{ref}}} \right)^{-\nu_{i,2,h}} \right) \tag{2.37}$$

to describe the activation losses. The charge transfer coefficient α in the Butler-Volmer equation is a measure of the symmetry of the energy barrier of the reaction. [11] α is usually assumed constant, however recent results have demonstrated that the anodic charge transfer coefficient is not constant for low temperatures. [26]

A wide range of different values for the reference transfer current density i_0 have been reported in the literature, and i_0 is therefore often chosen as a fitting parameter for models. [22] It should be noted that both the Butler-Volmer equation and the Tafel equation are semi-empirical relations that are sensitive to the choice of reference potential.

Due to the capacitive nature of the membrane-electrode interface, double layer charging may occur, giving the electrolyser as a whole a capacitive electrical response to changes in applied current density or voltage. The capacitive electrical response of the electrolyser presents a challenge for dynamic electrolyser modeling, and is as a whole usually neglected in published modeling efforts. The general mass conservation equation (2.8) can be expressed in the electrolyte phase, following the derivations of Newman & Thomas-Alyea [54], for a single electrode reaction including double layer charging

$$\frac{\partial\left(\varepsilon_2 c_{i,2}\right)}{\partial t} = -\nabla\cdot\boldsymbol{N}_{i,2} - \frac{\nu_{i,2,h}}{n_h F}\left(\mathsf{a}_{1,2} i_{h,\text{faradaic}} + \frac{\partial\left(\mathsf{a}_{1,2} q\right)}{\partial t}\right), \tag{2.38}$$

where $i_{h,\text{faradaic}}$ is the current associated with mass or charge specifically transported through the interface or involved in a reaction, and q is the surface charge density of the double layer.

Similarly to the membrane, hydration of the CL is of great importance for electrolyser performance via its relation to various material properties, and so water transport should be a focus of modeling efforts. Hydration of the electrolyte phase may be modeled in a similar fashion as the membrane, while the matrix phase is assumed to hold no water. Gas bubbles formed at the electrode surface may become problematic if they accumulate on the surface instead of moving out with the water flow, as they then limit water transport, reduce interfacial contact and reaction rate, and cause reaction and current distribution non-uniformities. The physics behind bubble formation and transport will not be derived in detail in this thesis.

A rigorous balance of mass in the electrolyte phase includes water and gases that are consumed, generated, and depart the CL into either the PTL or back through the membrane, including the formation, growth, accumulation and transport of gas bubbles on either side through the CL to the PTL and out of the cell. Boundary conditions must reflect the continuity of the physical system, and should account for state change of water between vapor, liquid and electrolyte-bound form.

The state of the art catalyst materials are considered to be iridium oxide (IrO_2) for the OER and highly dispersed platinum on high surface area carbon for the HER. [77] The search for sustainable and cheaper alternatives to the current expensive state of the art materials, and ways to reduce the necessary catalyst loading without compromising electrolyser performance, are research areas in which computational modeling may be of assistance.

2.4.3 Porous transport layers

As the name implies, the main purpose of the PTLs are to provide a pathway for reactants and products in and out of the electrolyser cell, between the CLs and flow channels in the BPPs. Additionally, they serve as a structural element adding mechanical strength to the cell. PTLs typically consist of porous media with high electrical conductivity and porosity to facilitate current, water and gas transport. The choice of material depends on the specifics of the reactants and products. If reactants are gases and products are liquid a gas diffusion layer (GDL) of a hydrophobic type of porous media is used, and in the opposite case a hydrophilic type. The hydrophobicity in the first case facilitates gas transport towards the membrane by making the gas phase the wetting phase, while the hydrophilia in the second case facilitates transport of liquid water by making the liquid phase the wetting phase. [66]

PTLs are often modeled as random structures with given pore characteristics, and evaluated by use of computational fluid dynamics (CFD). Geometric parameters related to the pore structure such as pore density distribution and throat size are often used to characterize the PTL. [5] Principles from fuel cell modeling may be applicable, with the important distinction that the carbon materials commonly used in PEM fuel cells are not usable in electrolysers as the high overpotential would cause corrosion by the formation of CO_2, [15] so care must be taken to incorporate appropriate material-specific characteristics for electrolyser PTLs.

Ineffective permeation of gas into the PTLs from the CL side can lead to a blockage of the catalyst, which as previously discussed inhibits interfacial contact and blocks the water to the catalyst site. In addition to hindering the reactant water from reaching the catalyst, the blockage also prevents effective removal of heat from the system. [5] These effects provide motivation for detailed investigation of PTL phenomena by computational modeling.

Rajora et al. [66] derived an extensive analytical modeling framework for the two-phase transport in PTLs. Care should be taken as these derivations are only valid for the case of fully humidified gas phase with no net phase change, and for negligible differential pressure. Thus the modeling framework is not applicable in the case of differential pressure operation, which as stated can have favorable effects on efficiency. The framework by Rajora et al. [66] is nonetheless a solid foundation upon which to build understanding of PTL phenomena and further development of PTL modeling.

2.4.4 Degradation

Component degradation is an important field of research which has been lacking in attention until recently. Few modeling studies exist for the effect of degradation on electrolyser performance, and the effect of operational conditions on the rate of degradation. Better understanding of the mechanisms governing degradation is key in identifying mitigating measures, which can increase the lifespan of the electrolyser.

Degradation phenomena occur in the membrane, CLs, MEAs, PTLs and bipolar plates, but as performance and durability issues have been mainly associated with membrane degradation, [16] the few electrolyser degradation studies that exist usually focus their efforts in this area. Studies of degradation of PEM electrolysers are furthermore largely based on fuel cell literature, though care must be taken as the two not necessarily directly applicable as the two are not exact opposites. [74] For example, degradation in PEM fuel cells is reported to occur on either side, while some experimental studies for PEM electrolysers indicate that both the anode membrane-CL interface and the bulk of the membrane on the anode side take less damage while the cathode side takes damage. [16]

Membrane degradation in PEM electrolysers occurs via the formation of hydrogen peroxide, H_2O_2, in the CLs, which then diffuses into the membrane, decomposes into free radicals and attack the membrane. As previously mentioned, crossover of oxygen gas from the anode to cathode has a large impact on crossover as it enters into the hydrogen peroxide formation reaction. Temperature and current density also have strong influences on the degradation rate. [16] Furthermore, poor interfacial contact between PTLs and CLs resulting in a non-homogeneous electric current distribution can cause the arisal of hot spots, which may cause deformation of the membrane. [15]

Other degradation phenomena in the electrolyser are largely associated with the acidic environment produced by the SPE. Very few catalyst materials exist that are resilient enough to withstand this environment, especially on the anode side, requiring the use of rare and expensive materials. Reduction of catalyst loading is thus an important factor in lowering the overall cost of the electrolyser, but a too large reduction could lead to increased membrane corrosion.

Degradation of the CL itself has been found to be less prevalent than membrane degradation, [71] but not necessarily negligible. Spöri et al. [73] present a thorough description of degradation mechanisms for anode CLs and how they may be mitigated. In the cathode PTL and BPP, a process known as hydrogen embrittlement, wherein the material deteriorates due to the hydrogen that is produced, occurs causing the components to lose their structural integrity and increasing resistances.

BPPs, typically made of titanium, corrode to develop oxide layers that increase contact resistance and decrease thermal conductivity. [77] Alternative BPP materials include graphite or stainless steel, but these also cannot withstand the corrosive environment in the electrolyser, causing worsening interfacial contact with the CLs over time. [15] In stainless steel BPPs, corrosion leads not only to an oxide layer, but also the release of metallic ions which displace protons in the membrane and reduce conductivity. [77]

2.4.5 Interfacial effects

At interfaces between components there is the potential for resistances and capacitances of various nature, such as contact resistances, double layer charging, and distribution non-uniformities as a result of component geometry and unfavorable corrosive reactions. Experimentally, design of electrolyser components is aimed at minimizing the hindrance to flow through and between components, leading to the selection of materials with high conductivities and permeabilities for the desired transport.

Assuming the success of interfacial optimization efforts, interfacial resistances are usually neglected between both components in a cell, and cells in a stack, in modeling efforts. Such approximations may agree well in a laboratory setting, however in industrial electrolysers where speed of assembly is prioritized higher, the cell assembly is usually somewhat less precise than in the lab setting, resulting in higher parasitic losses between layers. [15]

For the efficiency of industrial electrolysers to match that found through modeling, research efforts should address either improvement of assembly accuracy, [8] improvement of model accuracy through inclusion of realistic contact resistances in models, or both. Weber et al. [82] present a thorough description of the complex interfaces, their morphological properties and the causes of interfacial losses for each component interface.

Chapter 3

Multiphysical modeling approaches in literature

Different approaches to electrolyser modeling are taken in literature, with varying degrees of basis in theoretical physics and electrochemistry, versus empirical relations. In this chapter, approaches of previously published models to modeling of central phenomena in the electrolyser are discussed. The objective is to contrast and compare the most common methodologies, in order to develop an understanding of how and why decisions are made to select one method over another. This understanding will be put to use in the next chapter which describes the development of a computational PEM electrolyser model.

Details about each model will not be presented, as the chapter builds on the literature review. However, table 3.1, which gives an overview of models reviewed and their main approaches to electrolyser modeling, is included to provide a summary. Purely empirical models are outside the scope of this paper, as are balance-of-plant[1] models and equivalent circuit models.

---

[1] Some models discussed contain selected balance-of-plant components.

Table 3.1: Selection of published PEM electrolyser models, and their modeling approach. 0D refers to a lumped parameters model without spatial resolution, while 1D, 2D and 3D indicate a spatial resolution associated with distributions of various kinds within the model domain. Additional phenomena modeled are indicated by abbreviations: XO - crossover, TH - thermal, DP - differential pressure, DG - degradation, FF - flow field, also the notable analysis of exergy efficiency - EX. The table is reproduced with minor changes from the project thesis of the fall of 2022.

Author	**Year**	**Dimensionality of key phenomena and transience**				**Ref.**
		Species transport	**Voltage**	**Additional**	**Transient**	
Abdin et al.	2015	0D	0D	DP	No	[1]
Abomazid & Farag	2022		0D	DP	No	[2]
Agbli et al.	2011	0D EMR	0D	TH	Yes[2]	[3]
Aouali et al.	2017	0D	0D	TH	Yes[2]	[4]
Arbabi et al.	2016	3D two-phase CFD			Yes[2]	[5]
Aubras et al.	2017	2D+1D micro two-phase	0D+1D	TH	No	[6]
Awasthi et al.	2011	0D	0D		Yes[2]	[7]
Chandesris et al.	2015	1D		XO, DG	Yes[2]	[16]
Chen et al.	2022	3D two-phase	3D	TH, FF	No	[18]
Corengia & Torres	2018	0D two-phase	0D		Yes[2]	[19]
Correa et al	2022	0D	0D	TH, DP	Yes[2]	[20]
Dang et al.	2022	0D	0D	XO, TH, DP	Yes[2]	[21]
Fornaciari et al.	2020	2D	2D		No	[23]
García-Valverde et al.	2012	0D	0D	TH	Yes[2]	[26]
Görgün	2005	0D two-phase	0D		Yes[2]	[29]
Grigoriev et al.	2010	1D two-phase	0D	XO, TH, DP	No	[31]
Han et al.	2017	1D two-phase	0D	DP	No	[33]
Kalinnikov et al.	2021	1D two-phase	1D		No	[38]
Kim et al.	2013	0D two-phase	0D	XO, TH, DP	Yes[2]	[39]
Lebbal & Lecœuche	2009		0D	TH	Yes[2]	[41]
Lee et al.	2019	3D pore network			No	[42]
Lin & Zausch	2022	1D two-phase	1D		Yes	[43]
Liso et al.	2018	0D two-phase	0D	EX	Yes[2]	[44]
Marangio et al.	2009	0D two-phase	0D	circular MEA	No	[48]
Moradi Nafchi et al.	2019	0D	0D	DP, EX	No	[52]
Myles et al.	2012	1D two-phase DFM	1D	DP	No	[53]
Ni et al.	2008	1D	0D	EX	No	[57]
Ojong et al	2017	2D+3D micro two-phase	0D	TH	Yes[2]	[59]
Oliveira et al.	2013	1D+0D micro+nano	1D		Yes	[60]
Olivier et al.	2017	0D bond graph	0D	TH	Yes[2]	[61]
Sartory et al.	2017	0D two-phase	0D		No	[68]

---

[2] Does not contain an electrical capacitive mechanism, [1] see section 3.2.

3.1 Model dimensionality and multiphysics

Modeling approaches are in this thesis categorized as one of two main types, either zero-dimensional (0D) or multi-dimensional (1D, 2D, or 3D), with regards to the spatial resolution of their modeled phenomena. The different dimensionalities may also be combined for different parts of one electrolyser model. A 0D approach corresponds to modeling by lumped parameters where fluxes are often determined as input-output balances and the voltage is modeled by independent contributions from non-coupled processes,

$$V_{\text{cell}}(i) = \sum_n V_n(i) = E + V_{\text{kinetic}}(i) + V_{\text{mass transport}}(i) + V_{\text{ohmic}}(i). \tag{3.1}$$

As is evident from table 3.1, the vast majority of models take the 0D approach to cell voltage modeling, whereas only a few model the spatial resolution of the potential within the electrolyser.

As previously stated, voltage losses are greatly affected by processes occurring within the various components, which are highly coupled in nature and also depend heavily on parameters with a high spatial dependence on local saturation, pressure and temperature variations. With the 0D modeling approach it is not possible to simulate local variations, and thus the models provide much less insight into the dominant mechanisms of voltage loss and how they are affected by local conditions.

In higher-dimensional voltage modeling methods, the cell voltage is implicitly defined via the electric potential, which appears in coupling with other properties. When modeled in this way, it becomes possible for the voltage losses to take the same spatial resolution. Then, by comparing simulations of e.g. local conditions, species transport, and potential, information may be obtained about not only what processes cause resistance, but why.

Species transport is modeled as either single-phase or multi-phase. In order to qualify as multi-phase, the models must include simultaneous flow of more than one thermodynamic phase within the same component, e.g. PTLs where product gases are evacuated and water flows to the reaction sites, or PEM where product gases diffuse to the opposite side. Multi-phase transport is most often implemented in the porous media, and often described as driven by capillary forces, where the capillary pressure is defined as the pressure difference between the gaseous and liquid phases. [66, 80, 82, 83] The capillary pressure can be further related to a pore size distribution, as performed by Rajora et al., [66]

$$p_{\mathrm{C}} = p_{\mathrm{L}} - p_{\mathrm{G}} = -S_{\mathrm{wetting}}^{1/\lambda} \frac{2\gamma \cos\theta}{r}, \tag{3.2}$$

where the second equality follows from the Young-Laplace equation, [66] S is the saturation of the wetting phase, λ is the pore size distribution index, γ is the water surface tension, θ is the contact angle between a drop of water and solid, and r is the pore radius. Multi-phase modeling is relevant when modeling gas transport specifically, or for studying molecular interactions and phase equilibria. Around half of the models consider a biphasial flow, and product gas crossover is only simulated in models that are aimed specifically at investigating crossover effects.

In some areas there is a general consensus regarding modeling approach. For example, generated fluxes are modeled by Faraday's law, equation (2.26), and the open circuit potential is modeled by the Nernst equation (2.6), relations which are based in thermodynamics and electrochemistry. The same does not apply to modeling of the majority of the electrolyser phenomena, for which there are several methods in circulation. some methods appear more frequently in literature than others. The approach of Marangio et al. [48] for transport modeling is for example heavily referenced, but does by no means constitute a definite template for electrolyser modeling, and is in fact a 0D approach, albeit a rather comprehensive one.

The difference between approaches usually lies in what processes are considered to occur on a significant scale, and which can be neglected, in order to simplify the expressions. For example, some authors consider flow in the membrane to occur only via diffusion, some only pressure-driven flow, and some electroosmotic drag, or combinations thereof. Simplifications are found to be made both to the parts of the model that do not directly relate to the specific focus of the authors, and to the model as a whole. Specific investigation of bubble effects might require modeling of water as vapor on the catalyst boundary to simulate the liquid water blockage by the produced gas bubbles, [6] while models that are more concerned with efficiency and hydrogen output usually do not account for the existence of product gas within the membrane. Whether or not a discussion of simplifying assumptions and their implications is included is found to be highly variant in literature.

The material structure of each component can be a deciding factor in limiting or facilitating transport through the electrolyser. Though components are designed in such a way that they inhibit transport as little as possible in order to minimize unnecessary losses, the effect of structure is not negligible. While not possible in 0D and 1D models, the possibility arises in 2D and 3D models to resolve the geometry of the micro-structure as discussed in section 2.4, instead of using volume-averaged properties. Micro-structural resolution is performed for some of the higher-dimensional models in table 3.1. [5, 42] Interfacial effects were not modeled specifically in any of the models, but some were IR-corrected with experimental results to account for these effects in the cell voltage models.

In order to implement transport equations for the various species in the model, certain transport parameters determining the rate of different modes of transport must be defined. Many parameters do not have established analytical expressions due to the complexity of the phenomena they are related to. The value of transport parameters often greatly impact electrolyser performance, and their identification under varying conditions is therefore necessary in order to accurately predict electrolyser behaviour. For example, species transport coefficients such as conductivities and diffusivities are famously dependent on the saturation of the membrane and the temperature.

Common assumed relations for parameters which vary with temperature are Arrhenius dependencies (proportionality to the exponential of the negative inverse temperature), as this dependence matches well that observed experimentally. For reaction kinetics, expressions such as the Butler-Volmer equation (2.37) are often used. Dependencies are sometimes simplified by incorporating a model dependence based only the most prominent factors, but equally often models consider a dependency on several factors at once. To model a parameter as accurately as possible would entail including the effects of all operating conditions and phenomena that such as local pressure, temperature, activity, saturation, etc., but data for the relationship of each parameter with all of these conditions are not necessarily available, especially not for all ranges of possible conditions. Thus, models require some curve fitting of the transport parameters in order to match experimental results for a specific experimental electrolyser.

3.2 Transient and steady-state models

A common simplification of the electrolyser system is to consider steady-state operation. However for simulation of points of interest, such as startup and shutdown, coupling to renewable power sources, or stack temperature control, modeling of transient electrolyser behaviour is of interest. Table 3.1 shows that several such models have been developed. It is customary in most models to assume immediate electrical response, so that electrical equilibrium is instantaneously achieved also for dynamic electrolyser operation. In many applications this assumption is sufficient for the purpose of the model, since the electrical response of the system is much faster than the total system time response. [62]

In reality, the electrical response is not instantaneous, due to phenomena such as double layer capacitance, species diffusion limitation and accumulation. [62] Furthermore, for PEM electrolysers to be able to run in connection to renewable power sources, they must operate dynamically on-demand, further increasing the need and interest for more dynamic modeling.

The first papers of dynamic PEM electrolyser models were published in 2005. [15] Two notable early models for simulation of dynamic PEM electrolyser operation are those of Görgün [29] and Awasthi et al. [7]. However, these and most other models claiming to be dynamic, assume immediate electrical response of the electrolyser, neglecting the electrical capacitance mechanism due to its short characteristic time as described above.

To distinguish the fact that this type of model does not satisfy the criteria for a transient model, [1] such models are in this paper termed “dynamic steady-state” models. These models are usually steady-state electrochemical models with immediate time response that are coupled to dynamic external balance-of-plant components, thermal models, or power/current sources. The term is admittedly self-contradictory as "dynamic" and "steady-state" are somewhat opposite descriptions, but is introduced in order to acknowledge that some effects of dynamic modeling at larger time scales are included in the model. Thus, these "dynamic steady-state" models should be included to some degree in a discussion of transient electrolyser modeling, if only to emphasize the criteria for a truly transient model. Models incorporating capacitive electrical response are termed transient, and of these it is required that capacitive effects are modeled according to the principles outlined in chapter 2.

Based on the overview in table 3.1, thermal modeling is clearly further ahead than electrical modeling when it comes to transient electrolyser operation. Especially with the emerging use of PEM electrolysers in connection with intermittent energy sources, it would be interesting to see more research on modeling of the impacts of frequently varying current, intermittent shut-off periods, etc. on efficiency, lifetime and degradation. Some work on transient electrical modeling has already been performed in the PEM fuel cell community, e.g. by Jaouen & Lindbergh [37] and Wiezell et al. [86, 87].

3.3 Software and methods

The complexity of the phenomena means that detailed numerical modeling of electrolyser operation quickly increases in difficulty and computational cost with each new phenomena taken into consideration. Specialized software such as COMSOL Multiphysics, Modelica, Simulink, and others exist that are optimized to solve highly multiphysical, multidimensional, and complex systems of equations such as is required for electrolyser modeling. They can also greatly simplify the implementation, which is beneficial as researchers are not necessarily highly experienced in the inner workings of numerical methods.

However, though specialized software can be a powerful tool, it is usually expensive. The advantage of reducing the difficulty of modeling that is somewhat negated by loss of transparency, and by increased difficulty in validating and comparing models against each other, sharing and developing improved methods, and troubleshooting code. [82] Nonetheless, most of the models in table 3.1 were implemented using such specialized software.

Due to the high cost and lack of transparency, it can be desirable instead to use open-source software which is freely available. Open-source software with similar functionality to the specialized software does exist, such as OpenPNM for pore network simulations, and OpenFOAM, a computational fluid dynamics platform. Open-source modeling approaches do not suffer the same drawbacks as specialized software, but are however not without their own: Usually there is no easy-to-read graphical interface so that one is at the mercy of the thoroughness of the documentation, and higher demands are placed on the researcher in terms of a more in-depth understanding of both programming and the physical phenomena to be modeled. Very few of the reviewed models were implemented using open-source software for the entire process, but OpenPNM was used in several models to resolve the porous structure of CLs and PTLs.

3.4 Key takeaways

This chapter has presented a discussion of some key points of interest regarding the state of the art of PEM electrolysis modeling. Notably, it is rather uncommon among electrolyser models to incorporate the effects of the coupled transport processes within, with cell voltage usually modeled by 0D expressions, and multi-phase transport, especially within the PEM, less frequently modeled. Fundamental relations for thermodynamics and transport parameters estimation appear regularly, but beyond this there appears to be no general consensus for electrolyser modeling.

In general, the 0D approach of most models is sufficient to describe input/output relations, but will not be too helpful in order to conduct research on several aspects of electrolyser design such as components and materials. They may however be sufficient in some cases also for research of more complete systems, where heat production and efficiency losses are seen as part of a bigger system and a “black box” is all that is needed.

Another interesting feature is transient electrical effects, or lack thereof, in most models. Many models claiming to be dynamic or transient fail to attempt to capture transient electrical phenomena such as double layer charging, due to their short characteristic time scale. It is concluded that transient PEM electrolyser modeling is an area of research which would benefit from more research in the future, specifically with regards to modeling of transient electrical effects.

While advanced models incorporating more phenomena have the ability to better predict performance and suggest potential issues of electrolyser operation, the complexity of the physical processes in the electrolyser will always require some level of tradeoff between necessity, model accuracy, computational and theoretical difficulty, and available resources such as computation power and time. The conclusion is therefore not that models must necessarily include as many phenomena as theoretically possible, but that future researchers should note the importance of physical reasoning when justifying simplifications, and take care to practice transparency regarding their range of validity and in what ways they may cause erroneous results.

It is finally noted that while more accessible, open-source software may add computational difficulty compared to specialized software, and is much less frequently used. For the next chapter, which describes the development of a multiphysical computational PEM electrolyser, the following key points will be carried forward from the present discussion:

- Coupled multi-phase transport phenomena and voltage modeling are to be included with a spatial resolution in order to give the model diagnostic capabilities.
- In order to qualify as transient, the model must incorporate both electrical and inertial effects associated with the transport of charged and neutral species.
- Properties such as porosity, conductivity, diffusivity, etc. shall where possible be represented with a spatial dependence on the local value of thermodynamic properties, and water penetration in the electrolyser, to capture the effects of the presence and state of water, instead of averaged values.
- Though the argument has been made several times in this thesis that properties should be modeled with a higher degree of physical arguments, using as few empirical relations as possible, certain parameters must necessarily be provided

by experimental data as they so far do not have a definitive physics-based explanation.

- The model shall be implemented using exclusively open-source software, in order to examine the extent of limitations or advantages for multiphysical modeling associated with available software.
- In addition to the theoretical material presented, the model shall draw inspiration from the more developed field of hydrogen fuel cell modeling, which has overcome several of the challenges currently faced in electrolysis modeling research.

Chapter 4

Computational model

In this chapter, the derivation and implementation of a system of governing equations for a computational PEM electrolyser model is described, in line with the conclusions drawn in chapter 3. First, the physical system to be modeled is described and the model domain defined, followed by references to key PEM fuel cell modeling work which will serve as a basis for the present modeling work. Then, a system of governing equations for the model are derived for the steady-state case, and conversion to a transient system is described. Following the derivation of model equations, numerical methods are presented before moving on to the presentation of validation and simulation results in chapter 5.

Researchers [76] have identified beneficial effects of supplying liquid water on the cathode side, while flowing humidified air on the anode. The benefits include mitigation of some crossover issues through better control over the hydrogen-in-oxygen concentration on the anode side by increasing air flow if near-critical concentrations are detected. With the crossover issues alleviated, the use of much thinner membranes similarly to in hydrogen fuel cells, and high-pressure operation with far lesser safety concerns, becomes possible. The thinner membrane leads to correspondingly lower ohmic and mass-transport losses, and more compact system design. The modeling efforts shall be concerned with modeling an electrolyser of this configuration, with a thin PEM, liquid-water cathode feed and humidified air anode feed, by applying the concepts described in part 2.

The model electrolyser was assumed to fit the descriptions given in chapter 2.4 in terms of typical materials and structure for each component. The physical dimensions of the model electrolyser are given in table 4.1, and the modeling domain is indicated with a solid orange line in figure 4.1. With the x axis in the through-membrane direction (left to right in figure 4.1), the membrane is modeled from $0 < x < L_\mathrm{M}$ and indicated with a solid line, the CLs are situated at $x = 0$ and $x = L_\mathrm{M}$ indicated by the dots, and the anode PTL is modeled on $L_\mathrm{M} < x < L_\mathrm{M} + L_\mathrm{PTL}$, indicated by a stippled line.

Table 4.1: Model electrolyser dimensions and non-variable operating conditions. Anode and cathode thickness is equal for CLs and PTLs.

Symbol	**Value**	**Unit**	**Description**
L_M	15	µm	PEM thickness
L_CL	0	µm	CL thickness
L_PTL	200	µm	PTL thickness
T	333	K	Operating temperature
p_a	1	bar	Anode/ambient pressure

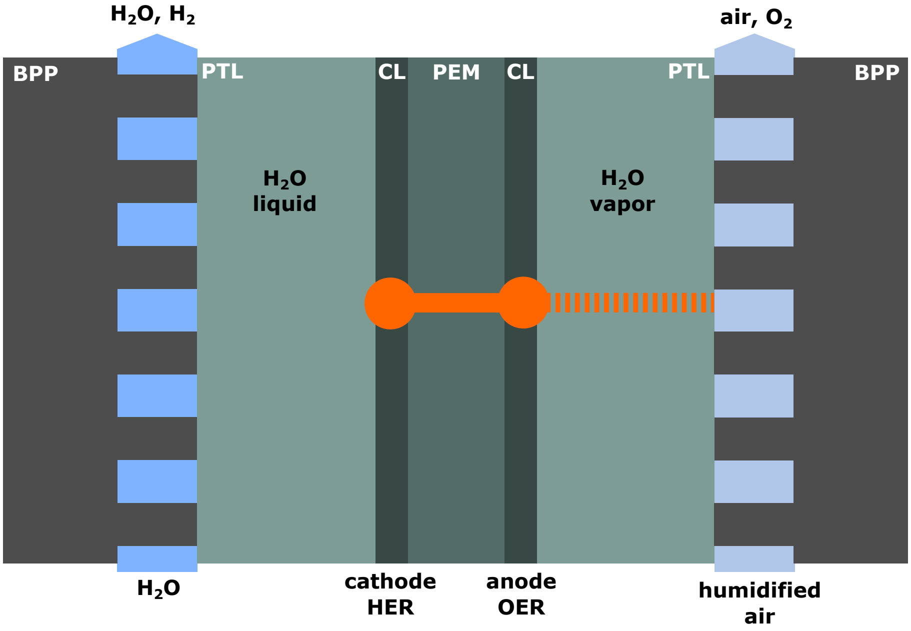

Figure 4.1: Modeling domain for computational model of the cathode liquid-, anode vapor-fed PEM electrolyser (not to scale). The orange solid line indicates the 1D PEM model domain, the dots indicate the 0D CLs, and the stippled line indicates the anode PTL.

To limit the complexity of the modeling efforts for the thesis, the electrolyser model components were constrained to include the PEM and CLs, with an additional simple sub-model for water vapor transport through the anode PTL. As the objective of the modeling efforts are to apply some of the discussed principles of multiphysical modeling to the PEM electrolyser, the PEM and simple anode PTL are modeled as a 1D domain in space. The CLs are not given as comprehensive a treatment, and are modeled as 0D boundaries between the PEM and PTLs.

Due to the simplifications made to the CLs and PTLs, the model is expected to be valid for the case where processes within the CLs and PTLs are not rate-limiting, assuming e.g. uniform reaction rates, perfect interfacial contact between components, and full saturation of the cathode PTL with liquid water at all times. Further details regarding assumptions and simplifications made for each component are provided in the upcoming sections describing modeling approaches for each component.

4.1 Notable fuel cell research

Throughout the modeling work, a great deal of inspiration has been taken from existing modeling work performed by the PEM fuel cell research and modeling community. Particularily notable models include those of Weber & Newman [84, 85], Zenyuk et al. [91], and Wiezell et al. [86, 87], which already have been, and will continue to be, referenced frequently in this thesis.

Another important work is the dissertation of Balliet [9], which contains thermodynamics-based derivations of equations for the chemical potential of water in each state of matter. For the liquid and vapor phase,

$$\mu_{\mathrm{L}} = \bar{H}_{\mathrm{L,t}}\left(1 - \frac{T}{T_{\mathrm{t}}}\right) + \bar{C}_{p_{\mathrm{L}},\mathrm{L}}\left(T - T_{\mathrm{t}} - T\ln\left[\frac{T}{T_{\mathrm{t}}}\right]\right) + \bar{V}_{\mathrm{L}}\left(p_{\mathrm{L}} - p_{\mathrm{t}}\right), \tag{4.1}$$

$$\mu_{\mathrm{V}} = \bar{H}_{\mathrm{V,t}}\left(1 - \frac{T}{T_{\mathrm{t}}}\right) + \bar{C}_{p_{\mathrm{V}},\mathrm{V}}\left(T - T_{\mathrm{t}} - T\ln\left[\frac{T}{T_{\mathrm{t}}}\right]\right) + RT\ln\left[\frac{px_{\mathrm{V}}}{p_{\mathrm{t}}}\right], \tag{4.2}$$

where $\bar{V}$, $\bar{C}_p$, and $\bar{H}$ are the molar volume, heat capacity, and enthalpy of liquid or vapor water at the given operating conditions of the electrolyser, and the subscript t denotes that the reference value is the value at the triple point of water. These relations are assumed to hold for the modeling work.

4.2 Membrane

The PEM model consists of a set of conservation equations discretized on an equally-spaced 1D grid. Several of the most important phenomena present in the membrane are included in the model, such as coupled transport of protons and water in the PEM by means of diffusion and electroosmotic drag, capillary action, local water saturation influence on the structural and electrochemical properties of the PEM, and elevated pressure effects on product gas crossover. The structural properties of the model membrane are assumed to be comparable to Nafion.

Taking a macro-homogeneous continuum modeling approach where void space and electrolyte is assumed to coexist at each point in space, the membrane model is based on the modeling work by Weber & Newman [84, 85] which has been observed to accurately describe observed behaviour, including Schroeder's paradox, in hydrogen fuel cells. [85] A great deal of inspiration is also taken from the model of Zenyuk et al. [91].

4.2.1 Governing equations

Two main transport phenomena are treated in the membrane model – coupled transport of water and protons, and product gas crossover. Transport equations for these phenomena were derived by Weber & Newman [84, 85], which are presented in this section, and also summarized in table 4.2.

As discussed in section 2.4.1, the most accurate representation of transport in the membrane is arrived at using concentrated-solution theory for interacting species, which yields expressions for the flux of protons and water [82, 84, 91]

$$\boldsymbol{i} = F\boldsymbol{N}_{\mathrm{H}^+} = -\kappa\nabla\Phi_{\mathrm{M}} - \frac{\kappa\xi}{F}\nabla\mu_{\mathrm{M}}, \tag{4.3}$$

$$\boldsymbol{N}_{\mathrm{H_2O}} = -\frac{\kappa\xi}{F}\nabla\Phi_{\mathrm{M}} - \left(\alpha + \frac{\kappa\xi^2}{F^2}\right)\nabla\mu_{\mathrm{M}}. \tag{4.4}$$

The subscript M denotes that the variables are evaluated for species associated with the membrane, in contrast to species in either the gas or liquid phase, and the subscript to denote water in the chemical potential μ is omitted for brevity of notation. Definitions of the transport coefficients κ, ξ and α are described in the next section.

Equations (4.3) and (4.4) indicate that protons and water move through the membrane as a joint result of gradients in electric potential and the chemical potential of water. In an electrolyser such as the one modeled here, where there is liquid water on the cathode side ($x = 0$) and water vapor on the anode side ($x = L_{\mathrm{M}}$), the chemical potential gradient is higher on the cathode than anode side, while the electrical potential is higher on the anode than cathode side. Thus the difference in chemical potential between anode and cathode presents impedes transport of protons from anode to cathode, due to water molecules bound to the protons in the electroosmotic flow.

Within the thickness of the membrane ($0 < x < L_{\mathrm{M}}$) there are assumed to be no chemical reactions or phase changes, so that equations (2.12) and (2.16) hold. On the PEM/CL boundaries however, where reactions producing and consuming water and protons take place, they do not hold, and the transport of water and protons between the electrodes ($0 \leq x \leq L_{\mathrm{M}}$) can be expressed as

$$\nabla \cdot \boldsymbol{i} = S_{\mathrm{H}^+}, \tag{4.5}$$

$$\nabla \cdot \boldsymbol{N}_{\mathrm{H_2O}} = S_{\mathrm{H_2O}}, \tag{4.6}$$

where S_{H^+} and $S_{\mathrm{H_2O}}$ are only non-zero at the boundary.

Combining equation (4.3) with (4.5) and (4.4) with (4.6) yields the governing partial differential equations (PDEs) for water and protons in the membrane model,

$$\nabla \cdot (-\kappa \nabla \Phi_{\mathrm{M}}) - \nabla \cdot \left(\frac{\kappa \xi}{F} \nabla \mu_{\mathrm{M}} \right) = S_{\mathrm{H}^+}, \tag{4.7}$$

$$\nabla \cdot \left(-\frac{\kappa \xi}{F} \nabla \Phi_{\mathrm{M}} \right) + \nabla \cdot \left(- \left(\alpha + \frac{\kappa \xi^2}{F^2} \right) \nabla \mu_{\mathrm{M}} \right) = S_{\mathrm{H_2O}}. \tag{4.8}$$

For gas crossover modeling, the product gases are assumed to be non-interacting with the water and protons. Transport is then assumed to occur via Fickian diffusion, and Henry's law stating that the amount of dissolved gas is proportional to its partial pressure above the liquid in which it is dissolved [93] is assumed to hold. The flux of hydrogen and oxygen in the membrane can then be expressed as [84]

$$\boldsymbol{N}_{\mathrm{H_2}} = -\Psi_{\mathrm{H_2}} \nabla p_{\mathrm{H_2}}, \tag{4.9}$$

$$\boldsymbol{N}_{\mathrm{O_2}} = -\Psi_{\mathrm{O_2}} \nabla p_{\mathrm{O_2}}, \tag{4.10}$$

where Ψ_i is the permeability of gas i in the PEM. By conservation of mass similarly to for water, the result is the governing equations

$$\nabla \cdot \left(-\Psi_{\mathrm{H_2}} \nabla p_{\mathrm{H_2}} \right) = S_{\mathrm{H_2}}, \tag{4.11}$$

$$\nabla \cdot \left(-\Psi_{\mathrm{O_2}} \nabla p_{\mathrm{O_2}} \right) = S_{\mathrm{O_2}}, \tag{4.12}$$

for product gas cross-diffusion through the membrane. Here, too, the source term is only non-zero at the boundary where the electrochemical reactions take place.

In the following, expressions for the various transport coefficients in equations (4.7), (4.8), (4.11), and (4.12) are presented. Source terms and boundary conditions for the PDEs are defined in section 4.5.

4.2.2 Transport parameters identification

The next problem is determining how to represent the various material and transport parameters of the components, and the impact of the presence and state of water. This section describes the derivation of relations for the various transport parameters. Values of constants and other membrane properties are given in table 4.4, and expressions used to calculate thermodynamic parameters are given in B.

The PEM structure described in section 2.4.1 is assumed to hold for the model, i.e. the membrane is mainly hydrophobic except for the sulfonic sites which can bond to protons released in the OER. The assumed effect of water penetration on membrane structure is visualized in figure 4.2, and is the same as was suggested by Weber & Newman [85]. As the membrane absorbs water, inverted micelles are formed at the sites, connected by so-called "collapsed channels". If there is no water in the membrane, $\lambda = 0$, there are assumed to be no connections between the active sites, but at a water content of around $\lambda = 2$, channels start to form. The hydration point $\lambda = 2$ is therefore termed the "percolation threshold". At a water content of around $\lambda = 14$, corresponding to the maximum water uptake for a membrane in contact with fully saturated water vapor, a complete network of collapsed channels is formed. [85] If the membrane instead is in contact with liquid water, there is enough pressure to expand the channels and fill them with water.

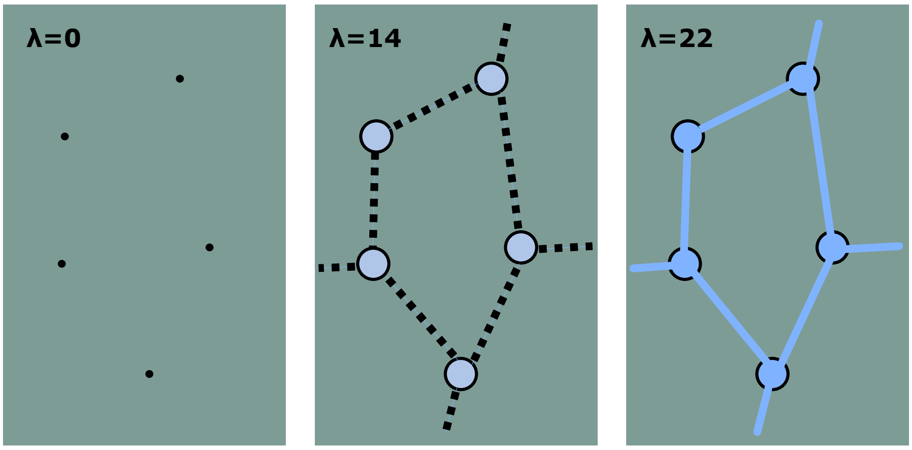

Figure 4.2: Visualization of PEM water uptake modeling principle. Water vapor content peaks at a value of around $\lambda = 14$, while liquid water has enough pressure to expand the channels between active sites in the membrane and can reach a water content of around $\lambda = 22$. Figure adapted from Weber & Newman [85].

Throughout the thickness of the membrane, the degree to which the water is able to penetrate varies. Modeling parameters and variables in the membrane are generally considered to be superpositions between the liquid-equilibrated and vapor-equilibrated case, weighted by the local water saturation of the membrane. For a generalized parameter ψ, the weighted superposition takes the form

$$\psi_{\mathrm{M}} = S\psi_{\mathrm{L}} + (1 - S)\psi_{\mathrm{V}}. \tag{4.13}$$

where S is the saturation, or fraction of expanded channels, and the subscripts L and V denote the liquid- and vapor-equilibrated case respectively. The subscript M in the weighted parameter is omitted in the transport equations derived below, for brevity of notation and as there are no parameters in other components or phases with which they may be confused.

In the case of a liquid-equilibrated membrane, the chemical potential of membrane-bound water is equal to the chemical potential of liquid water, $\mu_{\mathrm{M}} = \mu_{\mathrm{L}}$. In the model, the liquid-equilibrated membrane transport mode is considered to be that of a non-interacting medium, and the fully expanded channels in the membrane provide a pathway for water and proton transport. [85] Transport in the liquid-equilibrated case is assumed to occur via a hydraulic pressure gradient according to Darcy's law, combined with electroosmotic drag.

For the vapor-equilibrated case, the chemical potential of membrane-bound water is equal to the chemical potential of water in the vapor phase, $\mu_{\mathrm{M}} = \mu_{\mathrm{V}}$. As there is no continuous pathway, water is considered dissolved the membrane, and transport is modeled to occur via diffusion and electroosmotic drag. [85]

Water saturation

The membrane water saturation is calculated by assuming that all channels with a radius less than a critical radius r_c are collapsed, and all channels with radius larger than r_c are expanded with liquid water. The critical radius r_c is calculated from the local liquid water pressure, [84]

$$r_c = -\frac{2\gamma \cos\theta}{p_{\mathrm{L}}}, \tag{4.14}$$

where γ is the water surface tension, θ is the contact angle, and the local liquid water pressure p_{L} is expressed following equation (4.1) in terms of a correction to the triple point pressure p_t

$$p_\mathrm{L} = p_\mathrm{t} + \bar{V}_{\mathrm{H_2O}}^{-1}\left[\mu_\mathrm{L} + \bar{H}_\mathrm{L,t}\left(1 - \frac{T}{T_\mathrm{t}}\right) - \bar{C}_\mathrm{p,L}\left(T - T_\mathrm{t} - T\ln\frac{T}{T_\mathrm{t}}\right)\right]. \tag{4.15}$$

Equation (4.14) is equivalent to equation (3.2), and accounts for capillary action in the membrane.

The saturation S is finally calculated with [84]

$$S = \frac{1}{2}\mathrm{erfc}\left(\frac{\ln r_c - \ln 1.25}{0.3\sqrt{2}}\right) \tag{4.16}$$

where $\mathrm{erfc}(z) = 1 - \mathrm{erf}(z)$ is the complementary error function. Equation (4.16) results from integrating a log-normal fit of experimental Nafion microstructure channel-size distribution data, where 1.25 nm is the average pore radious and r_c also has units of nm. [84]

Water content, activity and volume fraction

Various ways of quantifying water in the membrane are used in addition to the saturation, to express the transport parameters. The choice of quantification parameter varies depending on practicality, as some parameters result in expressions on a simpler form than another, and convention, as parameter variations are often represented and measured in certain ways in literature.

The activity of water is calculated using equation (4.2), where the fraction in the final term on the right hand side can be simplified as

$$\frac{p x_\mathrm{V}}{p_\mathrm{t}} = \frac{p\,(p_\mathrm{V}/p)}{p_\mathrm{t}} = \frac{p_\mathrm{V}}{p_\mathrm{t}} = \frac{a p_\mathrm{sat}}{p_\mathrm{t}}. \tag{4.17}$$

With substitutions performed according to equation (4.17), solving equation (4.2) for the water vapor activity yields

$$a = \frac{p_\mathrm{t}}{p_\mathrm{sat}}\exp\left[\frac{\mu_\mathrm{M} - \bar{H}_\mathrm{V,t}(1 - T/T_\mathrm{t}) - \bar{C}_\mathrm{p,V}(T - T_\mathrm{t} - T\ln[T/T_\mathrm{t}])}{RT}\right]. \tag{4.18}$$

The activity of pure liquid water is assumed to have a constant value of 1, and the saturation water pressure p_sat is calculated based on the operating temperature of the electrolyser using the same expression as was used in determining the CIPM-2007 equation, which is recognised by the International Committee for Weights and Measures (CIPM). [65] The expression is given in appendix B.

The water content in the membrane is the number of water molecules associated with each sulfonic site, and is in the model expressed as a superposition following equation (4.13),

$$\lambda = S\lambda_{\mathrm{L}} + (1 - S)\lambda_{\mathrm{V}}. \tag{4.19}$$

The liquid-equilibrated value λ_{L} is assumed to have a constant value of 22 as this is the maximum water uptake of Nafion. [85] The vapor-equilibrated λ_{V} is calculated using an empirical fit of experimental for water uptake–activity data, [24]

$$\lambda_V = C_1 a^3 + C_2 a^2 + C_3 a, \tag{4.20}$$

where the empirical coefficients C_1, C_2, and C_3 hold the values presented in appendix B.1.

The water volume fraction f is then calculated from the water content [84]

$$f = \frac{\lambda \bar{V}_{\mathrm{H_2O}}}{\bar{V}_{\mathrm{M,dry}} + \lambda \bar{V}_{\mathrm{H_2O}}}, \tag{4.21}$$

where $\bar{V}_{\mathrm{H_2O}}$ and $\bar{V}_{\mathrm{M,dry}}$ are the molar volume of water and the dry membrane, respectively. Equation (4.21) is based on the assumption that the membrane can swell freely within the electrolyser. In reality, the swelling of the membrane is constrained by the adjacent components and clamping pressure, but for simplicity swelling was neglected in the present work. The water volume fraction can also be expressed as

$$f = S f_{\mathrm{L}} + (1 - S)\, f_{\mathrm{V}}, \tag{4.22}$$

where f_{L} and f_{V} are calculated by inserting the values of λ_{L} and λ_{V} into equation (4.21), respectively, in place of λ.

Protonic conductivity κ

The protonic conductivity κ is a measure of the membrane's ability to conduct protons, and is defined through Ohm's law for transport of protons in the absence of a concentration gradient, [82]

$$\boldsymbol{i} = -\kappa \nabla \Phi_{\mathrm{M}}. \tag{4.23}$$

The conductivity is modeled using a single functional form for both the liquid- and vapor-equilibrated case, as argued by Weber & Newman [84], which is dependent on the porosity ε_{M} of the membrane and the local temperature. The conductivity has been shown to vary with the porosity with a power of 1.5, and with an Arrhenius dependence on temperature. [84, 91] If the porosity ε_{M} of the membrane is taken to be equal to the water volume fraction f,

$$\kappa = \begin{cases} \kappa_0 \, (f - 0.06)^{1.5} \exp\left[\frac{E_{a,\kappa}}{R}\left(\frac{1}{T_{\mathrm{ref}}} - \frac{1}{T}\right)\right] & \text{for } f < 0.45, \\ \kappa_0 \, 0.39^{1.5} \exp\left[\frac{E_{a,\kappa}}{R}\left(\frac{1}{T_{\mathrm{ref}}} - \frac{1}{T}\right)\right] & \text{for } f \geq 0.45, \end{cases} \tag{4.24}$$

where $E_{a,\kappa}$ is the activation energy for proton conduction in the membrane. The physical reasoning behind the conductivity being constant with water for a volume fraction above 45 % is that beyond that point all of the channels in the membrane are fully expanded. [84] The prefactor κ_0 depends on the microscopic structure of the membrane, and is used as a fitting coefficient to obtain agreement with experimental data in chapter 5.

Electroosmotic drag coefficient ξ

The electroosmotic drag coefficient ξ is defined as as the number of water molecules transported across the membrane along with each proton, [85]

$$\xi = \frac{\boldsymbol{N}_{\mathrm{H_2O}}}{\boldsymbol{N}_{\mathrm{H^+}}}; \tag{4.25}$$

It is modeled according to equation (4.13) by a weighted superposition

$$\xi = S\xi_{\mathrm{L}} + (1 - S)\xi_{\mathrm{V}}. \tag{4.26}$$

The value of the electroosmotic drag coefficient is necessarily affected by the amount of protons traveling across the membrane, which is closely connected to the water content of the membrane. As the liquid-equilibrated membrane has a constant water content of 22, the liquid-equilibrated electroosmotic drag coefficient can be modeled only by its temperature dependence, here expressed by an Arrhenius dependence [84]

$$\xi_{\mathrm{L}} = 2.55 \exp\left[\frac{E_{a,\xi}}{R}\left(\frac{1}{T_{\mathrm{ref}}} - \frac{1}{T}\right)\right], \tag{4.27}$$

where $E_{a,\xi}$ is the activation for electroosmotic transport in the membrane.

The vapor-equilibrated electroosmotic drag coefficient has been found experimentally to be equal to 1 so long as the percolation threshold is reached, and is assumed to vary linearly with the water content λ for a water content below 1, as $\xi < \lambda$ must necessarily be fulfilled. [84] The resulting expression for ξ_{V} is

$$\xi_{\mathrm{V}} = \begin{cases} \lambda & \text{for } \lambda < 1, \\ 1 & \text{for } \lambda \geq 1. \end{cases} \tag{4.28}$$

Water transport coefficient α

The water transport coefficient α relates the gradient of the chemical potential and the flux of water in the absence of current, [84]

$$\boldsymbol{N}_{\mathrm{H_2O}} = -\alpha \nabla \mu_{\mathrm{M}}. \tag{4.29}$$

Comparing with equation (2.10), it can be observed to be analogous to a diffusion or permeability coefficient, but with the chemical potential instead of water concentration or pressure as the driving force. The correction for porosity ε_{M} in equation (2.10) is accounted for in the weighing of the liquid- and vapor-equilibrated α_{L} and α_{V} by the saturation of water in the membrane,

$$\alpha = S\alpha_{\mathrm{L}} + (1 - S)\alpha_{\mathrm{V}}. \tag{4.30}$$

As described previously, water transport in the liquid-equilibrated case can be described by Darcy's law in terms of a pressure gradient. Thus, α_{L} takes the role of a permeability coefficient

$$\boldsymbol{N}_{\mathrm{L}} = -\alpha_{\mathrm{L}} \bar{V}_{\mathrm{H_2O}} \nabla p_{\mathrm{L}} = -\frac{k_{\mathrm{L}}}{\mu \bar{V}_{\mathrm{H_2O}}} \nabla p_{\mathrm{L}}, \tag{4.31}$$

where k_{L} is the water permeability of the membrane, given by [84]

$$k_{\mathrm{L}} = k_{\mathrm{sat}} \left(\frac{f}{f_{\mathrm{L}}} \right)^2 \tag{4.32}$$

Comparing equations (4.31) and (4.32) it follows that

$$\alpha_{\mathrm{L}} = \frac{k_{\mathrm{sat}}}{\mu \bar{V}^2_{\mathrm{H_2O}}} \left(\frac{f}{f_{\mathrm{L}}} \right)^2 . \tag{4.33}$$

The vapor-equilibrated water transport coefficient similarly takes the role of a modified diffusion coefficient, [84]

$$\boldsymbol{N}_{\mathrm{V}} = -\frac{c_{\mathrm{V}} D_{\mu}}{RT\left(1 - x_{\mathrm{V}}\right)} \nabla \mu_{\mathrm{M}}, \tag{4.34}$$

where D_{μ} is a water diffusion coefficient with respect to the chemical potential driving force. Comparison with equation (4.29) readily provides the expression for α_{V},

$$\alpha_{\mathrm{V}} = \frac{c_{\mathrm{V}} D_{\mu}}{RT(1 - x_{\mathrm{V}})}. \tag{4.35}$$

The water diffusion coefficient relative to the chemical potential driving force D_{μ} has been experimentally shown to follow an Arrhenius dependence [91]

$$D_{\mu} = 2.26 \cdot 10^{-5} f \exp\left[\frac{E_{a,D}}{R} \left(\frac{1}{T_{\mathrm{ref}}} - \frac{1}{T} \right) \right], \tag{4.36}$$

where $E_{a,D}$ is the activation energy for diffusion of water in the membrane. Following equation (4.35), the vapor-equilibrated water transport coefficient is furthermore a function of the presence of water in the membrane via the concentration c_{V} and mole fraction x_{V}, which can both be expressed in terms of the water content [84]

$$c_{\mathrm{V}} = \frac{\lambda_{\mathrm{V}}}{\bar{V}_{\mathrm{H_2O}} \lambda_{\mathrm{V}} + \bar{V}_{\mathrm{M}}}, \tag{4.37}$$

$$x_{\mathrm{V}} = \frac{\lambda_{\mathrm{V}}}{\lambda_{\mathrm{V}} + 1}. \tag{4.38}$$

Product gas permeability Ψ

The permeability of hydrogen and oxygen in the membrane are a measure of the ability of the gases to penetrate and flow through the membrane. Expressions were obtained by assuming an Arrhenius dependence with temperature to experimental data for gas permeation through Nafion from Schalenbach et al. [69]. The general functional form of the Arrhenius fit is

$$\Psi = A_{\psi} \exp\left[-\frac{E_{a,\Psi}}{RT}\right], \tag{4.39}$$

where A_{ψ} is a fit coefficient and $E_{a,\Psi}$ is the activation energy of hydrogen or oxygen transport, both of which were found by curve fitting the experimental data. The coefficient values are reported in table 4.4.

Furthermore, figure 3 in Schalenbach et al. [69] shows a significant dependence of the permeability with the water content, where the permeability is strongly reduced when less water is present. The observed permeability trend indicates that a correction for the water content should be included. Based on the data, the permeability was multiplied with a correction factor ϖ between 0 and 1, determined from a 4th degree polynomial fit to the non-dimensionalized water uptake-permeability data,

$$\varpi(\bar{\lambda}) = B_0 + B_1\bar{\lambda} + B_2\bar{\lambda}^2\ B_3\bar{\lambda}^3\ B_4\bar{\lambda}^4, \tag{4.40}$$

where $\bar{\lambda}$ is the non-dimensionalized water uptake. A ϖ value of 1 corresponds to a liquid-equilibrated case, a value of about 0.97 corresponds to fully saturated water vapor, and the value of about 0.2 occurs at the percolation threshold. The same type of relation to water content is assumed to hold for the oxygen permeability. The polynomial fit is illustrated in figure 4.3, and the fit coefficients are given in appendix B.1. The polynomial fit is valid for water content between the percolation threshold and the maximum water uptake of $\lambda = 22$.

The relation for gas permeabilities do not contain a pressure dependence, as gas solubilities have been reported to be constant for pressures between 0-100 bar. [35] The membrane was assumed impermeable to nitrogen gas, which is present in the air flow, though transport of nitrogen could easily be implemented in the same fashion as for hydrogen and oxygen.

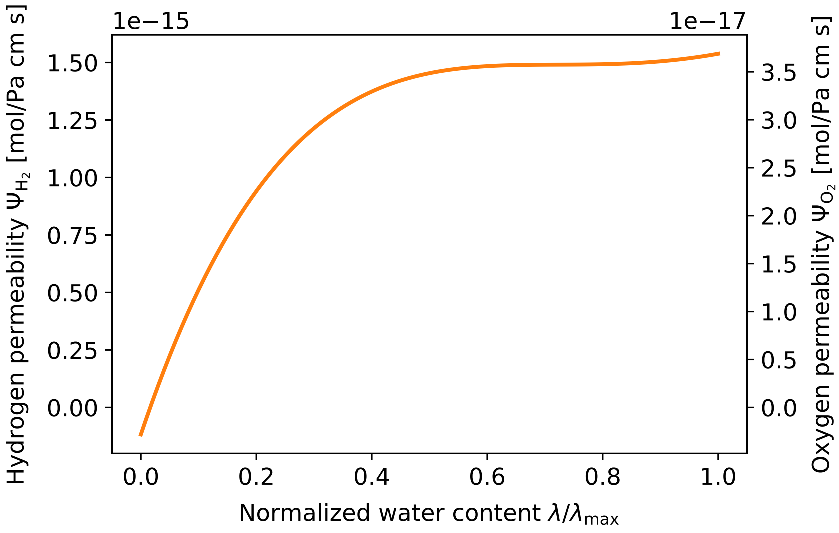

Figure 4.3: 4th order polynomial fit of normalized experimental water uptake–hydrogen permeability relation for Nafion. [69]

4.3 Catalyst layers

The CLs are modeled as 0D boundaries on either side of the membrane. The electrochemical reactions (2.2) and (2.3) take place in the anode and cathode CL, and are modeled on the right and left boundary of the PEM, respectively. To model the reaction kinetics, the Butler-Volmer equation (2.37) was taken as a starting point, and equation (2.37) is simplified to

$$i_h = i_{0,h}\left(a \exp\left[\frac{\alpha_{\mathrm{a}} F}{RT}\eta_h\right] - \exp\left[-\frac{\alpha_{\mathrm{c}} F}{RT}\eta_h\right]\right), \tag{4.41}$$

where a simple activity dependence is included for the oxidation OER. The activity of pure liquid water is set to 1. [84] The activities of the product gases are not considered. Equation (4.41) is further simplified by assuming that only the OER occurs at the anode, and only the HER at the cathode, so that one term is significantly larger than the other, and that all charge transferred from the solid matrix phase to the electrolyte phase in the single-point 0D CLs. Then, the transfer current densities i_{OER} and i_{HER} at their respective electrode can be modeled by a Tafel approximation

$$i_{\mathrm{OER}} = a i_{0,\mathrm{OER}} \exp\left[\frac{\alpha_{\mathrm{a}} F}{RT} \eta_{\mathrm{OER}}\right], \tag{4.42}$$

$$i_{\mathrm{HER}} = -i_{0,\mathrm{HER}} \exp\left[-\frac{\alpha_{\mathrm{c}} F}{RT} \eta_{\mathrm{HER}}\right]. \tag{4.43}$$

The exchange current density $i_{0,h}$ is modeled with an Arrhenius dependence [26, 44]

$$i_{0,h} = i_{0,h}^{\mathrm{ref}} \exp\left[\frac{E_h F}{R}\left(\frac{1}{T} - \frac{1}{T_{\mathrm{ref}}}\right)\right] \tag{4.44}$$

where the reference value was found empirically by data fitting the model at 60 °C against the experimental data set shown in figure 5.1.

At standard state, the activation energy of the HER is 0 V, and the activation energy of the OER is 1.23 V. However, as the computational model aims to describe electrolyser operation at differential pressure, a correction to each of the reaction energies was applied in terms of the Nernst equation (2.6) on either electrode,

$$E_{\mathrm{OER}} = E_{\mathrm{OER}}^{\mathrm{ref}} + \frac{RT}{n_{\mathrm{OER}} F} \ln\left[a\sqrt{\frac{p_{\mathrm{ref}}}{p_{\mathrm{O_2}}}}\right], \tag{4.45}$$

$$E_{\mathrm{HER}} = E_{\mathrm{OER}}^{\mathrm{ref}} + \frac{RT}{n_{\mathrm{HER}} F} \ln\left[\frac{p_{\mathrm{ref}}}{p_{\mathrm{H_2}}}\right]. \tag{4.46}$$

In equations (4.45) and (4.46), the activity of pure water is set to 1. The overpotential is defined by

$$\eta_h = \Phi_{\mathrm{S}} - \Phi_{\mathrm{E}} - E_h \tag{4.47}$$

where Φ_{S} is the potential in the solid electron-conducting phase of the CL, and Φ_{E} is the potential in the ion-conducting electrolyte phase. Equation (4.42) is applied in section 4.5 to calculate the cell potential by solving for Φ_{S}, while equation (4.43) is used to calculate a boundary condition for the membrane potential on the cathode side by solving for Φ_{E}.

4.4 Anode PTL

On the anode side, which is fed with a humidified air flow, a simple model for transport of water is included in order to provide a realistic boundary condition for the chemical potential of water on the anode CL-PEM boundary. Transport is assumed to occur via Fickian diffusion through the anode PTL,

$$\boldsymbol{N}_{\mathrm{H_2O,aPTL}} = -D_{\mathrm{aPTL}} \nabla c_{\mathrm{aPTL}}, \tag{4.48}$$

neglecting any flow due to differential pressure over the electrolyser. The general mass conservation for water in the anode PTL is on the same form as in the membrane,

$$\nabla \cdot \boldsymbol{N}_{\mathrm{H_2O,aPTL}} = S_{\mathrm{H_2O,aPTL}}, \tag{4.49}$$

yielding the governing conservation equation

$$\nabla \cdot (-D_{\mathrm{aPTL}} \nabla c_{\mathrm{aPTL}}) = S_{\mathrm{H_2O,aPTL}}. \tag{4.50}$$

The diffusion coefficient D_{aPTL} of water in the anode PTL is determined by assuming a correction for the PTL porosity, [86]

$$D_{\mathrm{aPTL}} = \varepsilon_{\mathrm{aPTL}}^{1.5} D_{\mathrm{H_2O}}^{\mathrm{ref}}, \tag{4.51}$$

where for simplicity, no dependence on saturation or temperature was considered. The source term and boundary conditions are defined in the next section.

The chemical potential μ_{aPTL} of water in the anode PTL is calculated from the resulting concentration profile using the relations of Balliet et al. [9]: Equation (4.2) for water in the vapor phase is solved for the chemical potential of water vapor, assuming a linear gradient in total pressure through the electrolyser and ideal gas.

4.5 Source terms and boundary conditions

The source terms in the conservation equations in table 4.2 must further be determined. As previously stated, there are assumed to be no reactions or phase changes within either the membrane or anode PTL, only at the anode and cathode CL boundaries with either the PEM or the anode PTL. Thus, all source terms are zero within the body of the membrane and anode PTL. The source terms derived in this section can be found summarized in table 4.3, and apply both in the steady-state and transient case.

To define the source terms for protons, water and product gases, we start from arguments made in chapter 2.3.1 and 2.4.2. Equation (2.9) provides a general source term in a mass conservation equation, and may also be applied to charged species. In the discussion of application of the conservation laws to the PEM electrolyser, it was stated that a rigorous balance of mass in the CLs should include water and gases that are consumed, produced, and depart the CLs either into the PTLs or the PEM. Sources related to bubble transport were neglected in the present model.

Water generation and consumption in the CLs is a result of phase change between membrane-bound, vapor, and liquid phase, as well as the OER on the anode side,

$$S_{\mathrm{H_2O}} = S_{\mathrm{H_2O},k\to\mathrm{M}} + S_{\mathrm{H_2O},h}. \tag{4.52}$$

Membrane-bound water is the water that is associated with the chemical potential of water as defined by the governing equations (4.7) and (4.8), while water is assumed to exist purely in the liquid form in the cathode PTL and CL, and purely in the vapor phase in the anode PTL and CL. From equation (2.9) it is clear that the source term $S_{\mathrm{H_2O},h}$ for water in terms of electrochemical reactions can be expressed as

$$S_{\mathrm{H_2O},h} = \begin{cases} 0 & \text{for } h = \mathrm{HER}, \\ -i_{\mathrm{OER}}/2F & \text{for } h = \mathrm{OER}. \end{cases} \tag{4.53}$$

The source term $S_{\mathrm{H_2O},k\to\mathrm{M}}$ describing water exchange between the CLs and the membrane can be expressed via a rate constant $k_{\mathrm{M}\to k}$, [91] which describes the rate of transfer from the membrane-bound phase to phase k,

$$S_{\mathrm{H_2O},k\to\mathrm{M}} = -k_{\mathrm{M}\to k}\left(\mu_{\mathrm{M}}|_{\mathrm{boundary}} - \mu_k|_{\mathrm{boundary}}\right), \tag{4.54}$$

where k is either liquid or vapor depending on the boundary – liquid on the cathode CL/PEM boundary, and vapor on the anode CL/PEM boundary. In total, the source term for water in equation (4.8) is therefore

$$S_{\mathrm{H_2O}} = \begin{cases} -k_{\mathrm{M}\to\mathrm{L}} \left(\mu_{\mathrm{M}}|_{x=0} - \mu_{\mathrm{L}}|_{x=0} \right) & \text{PEM/cathode CL boundary,} \\ -k_{\mathrm{M}\to\mathrm{V}} \left(\mu_{\mathrm{M}}|_{x=L_{\mathrm{M}}} - \mu_{\mathrm{V}}|_{x=L_{\mathrm{M}}} \right) - i_{\mathrm{OER}}/2F & \text{PEM/anode CL boundary.} \end{cases} \tag{4.55}$$

The same type of source term for water consumption and generation is found in the anode PTL model,

$$S_{\mathrm{H_2O,aPTL}} = \begin{cases} k_{\mathrm{M}\to\mathrm{V}} \left(\mu_{\mathrm{M}}|_{x=L_{\mathrm{PTL}}} - \mu_{\mathrm{V}}|_{x=L_{\mathrm{PTL}}} \right) & \text{anode CL/PTL boundary,} \\ 0 & \text{anode PTL/channel boundary,} \end{cases} \tag{4.56}$$

where the source term on the anode CL/PTL boundary describes the water entering the vapor phase in the CL from the membrane, and the water in the anode PTL and channel is assumed to be at electrochemical equilibrium so that no net phase change occurs. It is assumed that no electrochemical reactions occur in the PTLs.

Protons are consumed and produced in the electrolyser only by the electrochemical reactions on either side. Again following the formulation of equation (2.9), the source term for protons in terms of electrochemical reactions is a function of the reaction rate,

$$S_{\mathrm{H^+}} = S_{\mathrm{H^+},h} = \frac{i_h}{F}. \tag{4.57}$$

For the product gas source terms $S_{\mathrm{H_2}}$ and $S_{\mathrm{O_2}}$, the assumption is that all gas in the model crosses over, and is evacuated immediately out of the CLs into the PTLs upon reaching the opposite side of the membrane,

$$S_{\mathrm{H_2}} = S_{\mathrm{O_2}} = 0. \tag{4.58}$$

Finally, in order to solve the governing equations, boundary conditions must be imposed on the PDE variables Φ, $\mu_{\mathrm{H_2O}}$, $p_{\mathrm{H_2}}$, $p_{\mathrm{O_2}}$ and $c_{\mathrm{H_2O,aPTL}}$. Boundary conditions may be determined by examining in detail the electrical properties and composition of the water and gas mixture in the adjacent components in the electrolyser. A combination of Dirichlet and Neumann boundary conditions are used for the model, which are derived in the following.

Firstly, the BPPs and PTLs are assumed to have such a high electronic conductivity ($\sim \infty$) that there are no voltage losses associated with these components, and interfacial losses between all components are assumed negligible. Then, since there are no interfacial losses, $\Phi_\mathrm{M}|_{x=0} = \Phi_\mathrm{E}$ and equation (4.43) can be solved to give a boundary condition for Φ_M on the cathode boundary,

$$\Phi_\mathrm{M}|_{x=0} = \Phi_\mathrm{S}|_{x=0} + \frac{RT}{\alpha_\mathrm{c} F} \ln \left[-\frac{i_\mathrm{HER}}{i_{0,\mathrm{HER}}} \right] - E_\mathrm{HER}. \tag{4.59}$$

Considering the cathode BPP of the electrolyser to be grounded, it follows from the assumption of infinite electronic conductivity that the potential of the solid phase $\Phi_\mathrm{S} = 0$.

Charge conservation dictates that the transfer current in the CLs must be equal in magnitude to the operating current I. The current in the electron conducting phase is completely transferred into the proton conducting electrolyte in the 0D CLs, and further into the PEM, and vice versa. As the current density is related to the membrane potential Φ_M by equation (4.3), the boundary condition

$$\nabla \Phi_\mathrm{M}|_{x=L_\mathrm{M}} = -\frac{I}{\kappa} - \frac{\xi}{F} \nabla \mu_\mathrm{M}|_{x=L_\mathrm{M}} \tag{4.60}$$

is enforced on the gradient of Φ_M, where also the coefficients κ and ξ are evaluated at the anode.

The same approach as was used for the cathodic boundary condition for Φ_M is used to calculate the cell potential of the electrolyser. The cell potential V is given by solving equation (4.42) for Φ_S, with the assumption that $\Phi_\mathrm{M}|_{x=L_\mathrm{M}} = \Phi_\mathrm{E}$,

$$V = \Phi_\mathrm{S}|_{x=L_\mathrm{M}} = \Phi_\mathrm{M}|_{x=L_\mathrm{M}} + \frac{RT}{\alpha_\mathrm{a} F} \ln \left[\frac{i_\mathrm{OER}}{a i_{0,\mathrm{OER}}} \right] + E_\mathrm{OER}. \tag{4.61}$$

The use of equation (4.61) for the cell voltage implies that the water transport in the anode PTL is not associated with any voltage losses in the electrolyser.

The boundary condition for μ_{M} on the cathode CL/PEM boundary is calculated by assuming that the cathode PTL and CL are both fully saturated with liquid water, so that the membrane chemical potential can be assumed liquid-equilibrated at the boundary,

$$\mu_{\mathrm{M}}|_{x=0} = \mu_{\mathrm{L}}. \tag{4.62}$$

The chemical potential is then calculated using equation (4.1), where the liquid pressure equals the total pressure as there is only liquid water and no gas present, i.e. the gas pressure from crossover gases is assumed negligible. Note that as the chemical potential of water on the cathode side of the PEM is equal to the chemical potential of pure liquid water, the source term on the cathode side in (4.55) becomes zero.

The humidified air flow in the anode flow channel is delivered at a certain relative humidity (RH), which is given as either a percentage or fraction of the maximum possible humidity. The boundary condition for the concentration c_{aPTL} of water in the anode PTL is calculated using

$$c_{\mathrm{M}}|_{x=L_{\mathrm{PTL}}} = c_{\mathrm{V,flow}} = x_{\mathrm{V,flow}} \frac{\rho_{\mathrm{flow}}}{\bar{M}_{\mathrm{air}}}, \tag{4.63}$$

where the mole fraction of water vapor x_{V} is calculated from the RH as

$$x_{\mathrm{V,flow}} = \frac{p_{\mathrm{V,flow}}}{p_{\mathrm{tot,a}}} = RH \frac{p_{\mathrm{sat}}}{p_{\mathrm{tot,a}}}, \tag{4.64}$$

and the density of moist air as determined by Picard et al. [65], which is shown in B.

For hydrogen and oxygen gas, it was assumed that the partial pressure of each gas at the opposite PEM-CL boundary to where it was produced (anode for hydrogen, cathode for oxygen) was zero as a result of immediate evacuation from the cell. On the cathode side, the gas pressure of hydrogen was taken to be equal to the liquid pressure, as otherwise there would be a pressure gradient present; and on the anode side the oxygen pressure was calculated based on the oxygen concentration in the humidified air stream, where first the amount of water vapor in the stream was subtracted and oxygen assumed to make up 21% of the remaining mixture.

4.6 Conversion from steady-state to transient model

As mentioned in the introduction, electrolysers are especially interesting as a means of energy storage for intermittent renewable energy sources, where more hydrogen could be produced at a time when energy is available in abundance, such as on days with strong sun or wind. The stored hydrogen may then either be converted back to energy when conditions are less beneficial, or put to use elsewhere such as transport and industry.

When operated in this way, the operating conditions of the electrolyser will vary depending on time of day, weather, and demand. Since the various processes in the electrolyser are not instantaneous, changing the operating conditions will not result in immediate change of the output of the electrolyser. Capturing the behaviour of the electrolyser under varying operating conditions can help with identifying the beneficial or limiting operational conditions, and improving the lifetime of the electrolyser.

In order to capture transient effects in the electrolyser model, accumulation terms were added to the governing equations following the formulations in equations (2.8) and (2.13), so that the governing equations for water, proton and gas transport in the membrane became

$$\begin{aligned}
\frac{\partial\left(\varepsilon_{\mathrm{M}} c_{\mathrm{M}}\right)}{\partial t} &= -\nabla \cdot\left(-\frac{\kappa \xi}{F} \nabla \Phi_{\mathrm{M}}\right)-\nabla \cdot\left(-\left(\alpha+\frac{\kappa \xi^{2}}{F^{2}}\right) \nabla \mu_{\mathrm{M}}\right)+S_{\mathrm{H_2O}}, &(4.65)\\
\frac{\partial \rho_{\mathrm{e}}}{\partial t} &= -\nabla \cdot\left(-\kappa \nabla \Phi_{\mathrm{M}}\right)-\nabla \cdot\left(-\frac{\kappa \xi}{F} \nabla \mu_{\mathrm{M}}\right)+S_{\mathrm{H}^{+}}, &(4.66)\\
\frac{\partial\left(\varepsilon_{\mathrm{M}} p_{\mathrm{H_2}}\right)}{\partial t} &= -R T\, \nabla \cdot\left(-\Psi_{\mathrm{H_2}} \nabla p_{\mathrm{H_2}}\right)+S_{\mathrm{H_2}}, &(4.67)\\
\frac{\partial\left(\varepsilon_{\mathrm{M}} p_{\mathrm{O_2}}\right)}{\partial t} &= -R T\, \nabla \cdot\left(-\Psi_{\mathrm{O_2}} \nabla p_{\mathrm{O_2}}\right)+S_{\mathrm{O_2}}, &(4.68)
\end{aligned}$$

and the governing equation for water transport in the anode PTL became

$$\frac{\partial\left(\varepsilon_{\mathrm{aPTL}} c_{\mathrm{aPTL}}\right)}{\partial t}=-\nabla \cdot\left(-D_{\mathrm{aPTL}} \nabla c_{\mathrm{aPTL}}\right)+S_{\mathrm{H_2O,aPTL}}. \qquad (4.69)$$

As can be seen from equation (4.66) in combination with the source term for protons in equation (4.57), double layer charging of the CLs, which gives the electrolyser its capacitive electrical behaviour, is not described by the model. double layer charging is added to the model by including a transient source term for surface charge accumulation $\partial\left(\mathsf{a}_{1,2}q\right)/\partial t$ as described in equation (2.38). The electric double layer is on the nm scale, while the spatial resolution of the model membrane is on the ~ 10 nm scale, so the double layer is not included in the present model.

As before, the porosity of the membrane ε_{M} was taken to be equal to the volume fraction of water in the membrane. The concentration c_{M} of membrane-bound water was calculated from equation (4.37) with the water content λ inserted instead of λ_{V}, and the volumetric charge density ρ_{e} was calculated from Poisson's equation (2.17). An estimate of the value of the dielectric constant ε_{M} of the membrane was obtained based on a cubic spline interpolation of experimental data for Nafion from Paddison et al. [64] for varying water content.

The conversion from steady-state to transient is fairly simple on paper, but added significant complexity to the model implementation. The nature of the challenges that arose and how they were dealt with is described in sections 4.7.3 and 4.7.4.

Table 4.2: Steady-state and transient model equations summary. The transient accumulation term appears on the left side in the conservation equations.

Quantity	**Transient term**	**Steady-state equation**	**Domain**
Charge conservation	$\partial \rho_{\mathrm{e}} / \partial t$	$\nabla \cdot (-\kappa \nabla \Phi) + \nabla \cdot \left(-\frac{\kappa \xi}{F} \nabla \mu_{\mathrm{H_2O}}\right) = S_{\mathrm{H^+}}$	PEM
Mass conservation	$\partial \left(\varepsilon_{\mathrm{M}} c_{\mathrm{M}}\right) / \partial t$	$\nabla \cdot \left(-\frac{\kappa \xi}{F} \nabla \Phi\right) + \nabla \cdot \left(-\left(\alpha + \frac{\kappa \xi^2}{F^2}\right) \nabla \mu_{\mathrm{H_2O}}\right) = S_{\mathrm{H_2O}}$	PEM
	$\partial \left(\varepsilon_{\mathrm{M}} p_{\mathrm{H_2}} / RT\right) / \partial t$	$\nabla \cdot \left(-\Psi_{\mathrm{H_2}} \nabla p_{\mathrm{H_2}}\right) = S_{\mathrm{H_2}}$	PEM
	$\partial \left(\varepsilon_{\mathrm{M}} p_{\mathrm{O_2}} / RT\right) / \partial t$	$\nabla \cdot \left(-\Psi_{\mathrm{O_2}} \nabla p_{\mathrm{O_2}}\right) = S_{\mathrm{O_2}}$	PEM
	$\partial \left(\varepsilon_{\mathrm{aPTL}} c_{\mathrm{aPTL}}\right) / \partial t$	$\nabla \cdot \left(-D_{\mathrm{H_2O,aPTL}} \nabla c_{\mathrm{H_2O,aPTL}}\right) = S_{\mathrm{H_2O,aPTL}}$	anode PTL
Reaction kinetics		$\eta_{\mathrm{HER}} = -\left(RT/\alpha_{\mathrm{c}} F\right) \ln\left[-i_{\mathrm{HER}}/i_{0,\mathrm{HER}}\right]$	cathode CL
		$\eta_{\mathrm{OER}} = \left(RT/\alpha_{\mathrm{a}} F\right) \ln\left[i_{\mathrm{OER}}/i_{0,\mathrm{OER}}\right]$	anode CL

Table 4.3: Steady-state and transient model source terms.

Source term	**Cathode CL**	**PEM**	**Anode CL**	**Anode PTL**
	$\boldsymbol{x = 0}$	$\boldsymbol{0 < x < L_{\mathrm{M}}}$	$\boldsymbol{x = L_{\mathrm{M}}}$	$\boldsymbol{L_{\mathrm{M}} < x < L_{\mathrm{M}} + L_{\mathrm{PTL}}}$
$S_{\mathrm{H^+}}$	i_{HER}/F	0	i_{OER}/F	
$S_{\mathrm{H_2O}}$	$-k_{\mathrm{ML}}\left(\mu_{\mathrm{M}} - \mu_{\mathrm{L}}\right)$	0	$-k_{\mathrm{MV}}\left(\mu_{\mathrm{M}} - \mu_{\mathrm{V}}\right) - i_{\mathrm{OER}}/2F$	
$S_{\mathrm{H_2}}$	0	0	0	
$S_{\mathrm{O_2}}$	0	0	0	
$S_{\mathrm{H_2O,aPTL}}$			$k_{\mathrm{MV}}\left(\mu_{\mathrm{M}} - \mu_{\mathrm{V}}\right)$	0

4.7 Numerical methods

The model framework of governing PDEs, shown in table 4.2, consists of a set of coupled differential equations with a mutual dependence between the PDE variables and coefficients due to the dependence of the transport parameters of the membrane water saturation. This mutual dependence introduces a strong non-linearity to the system. The remaining task is implementation of the system in the computational model, which is described in this chapter, starting with software and methods, and then describing the specific method of implementation for the steady-state and dynamic simulations.

4.7.1 Software

In order to investigate the validity of the claims of advantages associated with open-source software listed earlier, the model was implemented using Python and the FiPy PDE solver package developed at the US National Institute of Standards and Technology (NIST) by Guyer et al. [32]. The theoretical foundations presented in chapter 2 provide the necessary in-depth understanding of the system, and the objective is to investigate whether advantages of using open-source software really outweigh disadvantages, when applied to modeling of complex electrochemical systems.

FiPy was originally developed for materials science purposes, but has also been applied in several other areas of research such as solid state physics [30] and radiation physics [50]. The reason that FiPy is widely applicable is that it can solve an arbitrary number of PDEs on the highly general form [32]

$$\frac{\partial\left(\rho\psi\right)}{\partial t} = \left[\nabla\cdot\left(\Gamma_i\nabla\right)\right]^n\psi + \nabla\cdot\left(\boldsymbol{v}\psi\right) + S_\psi, \tag{4.70}$$

which is essentially equation (2.7) with n^{th} order diffusion and advection of the general property ψ inserted in place of the general flux $\boldsymbol{N}$, by discretizing the equations and applying the finite volume method to solve for the system variables. Furthermore, implementation of the governing equations in FiPy is relatively easy even for an untrained programmer, with equation (4.70) represented in the intuitive way [32]

```
    TransientTerm(...) == (DiffusionTerm(...)
```

```
                        + <...>ConvectionTerm(...) + <...>SourceTerm(...))
```

In the preceding chapters, governing modeling equations have been consciously derived on the same form, so that it is readily seen how they may be implemented using FiPy. An arbitrary number of such equations may be coupled together. The residual (the L^2-norm of the solution matrix equation, $||\mathbf{L}\boldsymbol{x} - \boldsymbol{b}||$) is used as a criterion for convergence. Using FiPy to implement the governing equations removes labor associated with rigorously discretizing the system manually, and leaves capacity to focus on model development, integration of more phenomena, and processing and analysis of model results.

4.7.2 Finite difference methods in 1D

FiPy relies on the finite volume method to solve the set of coupled PDEs in table 4.2. Variables and coefficients are discretized on a uniform grid, for which the method reduces to the finite difference method. [32] In the finite difference method, the system of equations is discretized on a grid where the value of the variable at each grid point is determined from a discrete amount of its neighbors. Common types of difference methods are forward, central, and backward differences, where the neighbors used to calculate the cell value are oriented as specified by the method title with regards to the cell being approximated. The PDE variables are calculated in the regions between grid points, or cells, and the derivatives are calculated on grid points, or cell faces. In FiPy, fluxes are calculated using a two-point central difference scheme, [32] which exemplified in 1D on a Cartesian grid looks like

$$\frac{d\psi}{dx}(x) = \frac{\psi(x - \frac{1}{2}) - \psi(x + \frac{1}{2})}{\Delta x}. \tag{4.71}$$

The two-point central finite difference approximation to the derivative $d\psi(x)/dx$ has an approximation error of $\mathcal{O}(\Delta x)$.

For the present model, two grids are employed – one for the PEM and CLs, and one for the anode PTL. As both the steady-state and transient system models require iteration to convergence, the anode PTL model is solved separately in each iteration, with the membrane chemical potential of water from the previous iteration used in the source term given by equation (4.56). The resulting anode PTL chemical potential of water is then included in the source term for water in the membrane/CLs, equation (4.55).

4.7.3 Dealing with instabilities

The conversion to transient model resulted in a significant increase in complexity of the modeling endeavors. In order to calculate the volumetric charge density, defined by the Poisson equation (2.17), the second derivative of the potential Φ_{M} is needed. Due to the weighted-average representation of the membrane, a discontinuity appears in Φ_{M} where the membrane starts to become more vapor-equilibrated. Common numerical difference approaches such as the finite-difference method employed by FiPy, are famously ineffective and noise-amplifying when applied to data that is not smooth and continuous. [17] Significant stability and divergence issues arise when attempting to implement the Poisson equation (2.17) in the "easy" FiPy way, or using manually computed finite difference methods.

Computing the derivative, and second derivative, of Φ_{M} thus presents a challenge. Commonly, attempts are made to smooth or interpolate unsatisfactory values so that they may be differentiated using finite differences. However, as exemplified by Chartrand [17], these approaches also result in an inaccurate derivative which is still highly sensitive to noise and discontinuity. For the second derivative, further smoothing and interpolating causes significant loss of data, and any such method would be highly unpredictable as the operating current is varied.

As a solution to the problem of differentiation of the discontinuous Φ_{M}, a total-variation regularization scheme is implemented, as outlined by Vogel [79] and Chartrand [17]. By regularizing the differentiation process, the computed derivative is guaranteed a certain degree of regularity and accordance with the data, depending on adjustable tuning parameters. [17] Such a scheme was implemented, the details of which are given in the next section.

4.7.4 Differentiation by total-variation regularization

The process described here for total-variation regularization is the same as described by Vogel [79] and Chartrand et al. [17]. The concept behind total-variation regularization of the differentiation process is to perform Tikhonov regularization of the corresponding inverse process. The problem to solve is to find the function $\boldsymbol{u}$ which minimizes the functional

$$F(\boldsymbol{u}) = \varphi R(\boldsymbol{u}) + DF(\mathbf{A}\boldsymbol{u} - \boldsymbol{f}) \tag{4.72}$$

on the interval $[0, L]$, where φ is regularization tuning parameter, $\mathbf{A}$ is the antidifferentiation operator, and $\boldsymbol{f}$ is the data to be differentiated. In equation (4.72), $R(\boldsymbol{u})$ is a regularization term that causes the functional to increase with irregularity in u, and $DF(\mathbf{A}\boldsymbol{u} - \boldsymbol{f})$ is a "data fidelity" term that causes the functional to increase when the computed antiderivative $\mathbf{A}\boldsymbol{u}$ is not in agreement with the function data $\boldsymbol{f}$. The $\boldsymbol{u}$ that minimizes $F(\boldsymbol{u})$ is then the approximation to the derivative of $\boldsymbol{f}$. In the case of the particular application of the method to the Poisson equation (2.17), $\boldsymbol{f} = \Phi_{\mathrm{M}}(x)$, defined in the N cell centers of the interval $x \in [0, L_{\mathrm{M}}]$. Furthermore, the derivative $\partial \boldsymbol{f}/\partial x$ and $\boldsymbol{u}$ are defined on the N+1 cell faces, i.e. grid points.

Analytically, the various terms were defined as follows [17]

$$R(\boldsymbol{u}) = \int_0^L |\boldsymbol{u}'| \, dx, \tag{4.73}$$

$$DF(\mathbf{A}\boldsymbol{u} - \boldsymbol{f}) = \frac{1}{2} \int_0^L |\mathbf{A}\boldsymbol{u} - \boldsymbol{f}|^2 \, dx, \tag{4.74}$$

$$\mathbf{A}\boldsymbol{u}(x) = \int_0^x \boldsymbol{u} \, dx. \tag{4.75}$$

For φ, many different definitions can be applied, but for simplicity reasons φ was chosen to be defined as a floating-point number.

The functional to be minimized then takes the form

$$F(\boldsymbol{u}) = \varphi \int_0^L |\boldsymbol{u}'| \, dx + \frac{1}{2} \int_0^L |\mathbf{A}\boldsymbol{u} - \boldsymbol{f}|^2 \, dx, \tag{4.76}$$

In accordance with Vogel [79] and Chartrand et al. [17], the method of lagged diffusivity was applied in order to improve convergence. Minimizing the functional corresponds to solving to convergence a PDE resulting from applying the Euler-Lagrange equation. [17] The system is then solved using matrix formalism, and the steps of the algorithm are given below.

1. Define the differentiation matrix **D** and antidifferentiation matrix **A**, where the matrix elements are given by the equations

$$\mathbf{D}\boldsymbol{u}(x_i + \frac{\Delta x}{2}) = \left(\boldsymbol{u}(x_{i+1}) - \boldsymbol{u}(x_i)\right), \tag{4.77}$$

$$\mathbf{A}\boldsymbol{u}(x_i + \frac{\Delta x}{2}) = \left(\boldsymbol{u}(x_{i+1}) + \boldsymbol{u}(x_i)\right), \tag{4.78}$$

   Both **A** and **D** are N × (N+1) matrices, which when applied to the (N+1) × 1 $\boldsymbol{u}$ constitute transformations from the N × 1 to (N) × 1 dimension. These matrices only need to be calculated once for a given electrolyser model, as they rely only on the grid spacing, which is constant throughout. As can be seen from the definitions in equations (4.77) and (4.78), the matrices perform differentiation and integration by centered differences and the trapezoid method, respectively.

2. Perform fixed point iterations until the system is converged by repeating the following steps for each iteration n. The algorithm for this step was given by Vogel [79]:

   (a) Compute $\mathbf{E}_n$ as the N × N diagonal matrix defined by

$$\mathbf{E}_n = \mathrm{diag}\left[\left(\left(\boldsymbol{u}_n(x_i) - \boldsymbol{u}_n(x_{i-1})\right)^2 + \epsilon\right)^{-1/2}\right], \tag{4.79}$$

   where ϵ is some small parameter which is introduced to avoid division by zero.

   (b) Compute the discretized diffusion operator $\mathbf{L}_n$ as the (N+1) × (N) matrix

$$\mathbf{L}_n = \Delta x \mathbf{D}^{\mathrm{T}} \mathbf{E}_n \mathbf{D}. \tag{4.80}$$

   (c) Compute the approximate (N + 1) × (N + 1) Hessian matrix $\mathbf{H}_n$ as

$$\mathbf{H}_n = \mathbf{A}^{\mathrm{T}}\mathbf{A} + \varphi \mathbf{L}_n. \tag{4.81}$$

(d) Calculate the $(\mathrm{N}+1) \times 1$ gradient $\boldsymbol{g}_n$ as

$$\boldsymbol{g}_n = \mathbf{A}^{\mathrm{T}} \left(\mathbf{A}\boldsymbol{u}_n - \boldsymbol{f} + \alpha \mathbf{L}_n \mathbf{u}_n \right). \tag{4.82}$$

(e) Take a quasi-Newtonian step by solving the matrix equation

$$\mathbf{H}_n \boldsymbol{s}_{n+1} = -\boldsymbol{g}_n, \tag{4.83}$$

where $\boldsymbol{s}_{n+1} = \boldsymbol{u}_{n+1} - \boldsymbol{u}_n$.

(f) From the current approximation and the computed step s_{n+1}, calculate the new approximate derivative

$$\boldsymbol{u}_{n+1} = \boldsymbol{u}_n + \boldsymbol{s}_{n+1}. \tag{4.84}$$

3. The final $\boldsymbol{u}_n$ at the end of the fixed point iteration is the approximated derivative of $\partial \boldsymbol{f}/\partial x$, in the case of this thesis $\partial \Phi_{\mathrm{M}}/\partial x$.

4.8 Model implementation and usage

The model as described so far is first implemented for the steady-state case, in order to validate it against experimental polarization curves for various gauge pressures. The steady-state model is further used to simulate how different operating conditions affect the simulated voltage losses and transport in the membrane. Then, the model is modified for the transient case, adding accumulation terms to the equations as shown in section 4.6, or equivalently, table 4.2. Due to convergence issues, the accumulation terms in equations (4.65) and (4.66) could not be implemented using the notation described in section 4.7.1, but required instead manual discretization as transient sources. [32] Convergence is further discussed in section 5.4.

Constants and parameter values used are given in table 4.4, and the empirical relations for thermodynamical properties of water and various curve fit coefficients are given in appendix B. This section further describes specific details regarding the implementation of each simulation case.

Due to the dependence of the various transport parameters on the PDE variables, the computational model requires iteration to convergence. Any occurrence of the PDE variables Φ, μ, $p_{\mathrm{H_2}}$, and $p_{\mathrm{O_2}}$ in the calculation of the transport parameters as described above utilizes the value from the previous iteration (or initial guess). The PDE solution algorithm is shown below.

For the steady-state simulation:

1. Assert initial guesses for PDE variables and transport parameters, and a tolerance criterion for the residual. Set the initial residual to be higher than the tolerance criterion.
2. While the residual is higher than the tolerance criterion, repeat the following steps.
    (a) Solve the steady-state PDEs using coefficient values from the previous iteration.
    (b) Update the value of the PDE coefficients, boundary conditions and source terms using PDE variable values from the current iteration.
3. The final solution of the PDEs is reached when the convergence loop is broken.

For the dynamic simulation:

1. Solve steady-state system as described above to achieve initial guesses for system, corresponding to having run the system for a while in steady-state.
2. Set $t = 0$, and determine the time step length Δt and the number of steps.
3. Define the operating current as a function of t.
4. For each time step, repeat the following.
    (a) Set the initial residual to be higher than the tolerance criterion.
    (b) While the residual is higher than the tolerance criterion, repeat the following steps.
        i. Solve the transient PDEs using coefficient values from the previous iteration.

      ii. Update the value of PDE coefficients, boundary conditions and source terms using PDE variable values from the current iteration.

   (c) The PDE solution for the current time step is reached when the convergence loop is broken.

   (d) Update the `old` value of the PDE variables and coefficients to the current value.

   (e) Save a copy of the value of the operating current and cell potential at the current time step.

   (f) Increment t by Δt and calculate new value of operating current.

5. The resulting values of operating current and cell voltage may be used for analysis or further processed.

4.8.1 Steady-state simulations

The steady-state simulations are performed for a range of operating currents, applied cathode pressures, and anode air flow stochiometries. For the purposes of comparison to experimental data, a polarization curve is first calculated by solving the model to convergence, and then applying equation (4.60) to calculate the cell voltage, for a range of applied current densities. The coefficients κ, $i_{0,\mathrm{HER}}^{\mathrm{ref}}$, and $i_{0,\mathrm{OER}}^{\mathrm{ref}}$ are used as curve fitting coefficients in order to obtain better agreement with experimental polarization curves. Polarization curve validation results are presented in section 5.1.1

The effect of differential pressure operation on water transport in the model is then examined by studying the saturation profile in the membrane for a range of cathode gauge pressures. The results are used to elucidate aspects of how the amount of water in the membrane affects other model parameters. Simulations are similarly performed for varying humidification of the anode air stream, in order to examine how varying the RH of the air stream affects transport and losses in the electrolyser, by examining the simulated water saturation and polarization curves for a varying anode air stream RH. Results are presented in section 5.1.2 and 5.1.3, respectively.

Lastly for the steady-state case, the combined effect of variations in gauge pressure and RH on water transport in the membrane are investigated by studying their effect on the saturation of liquid water in the membrane. The results for combined effect of gauge pressure and RH are presented in section 5.1.4.

4.8.2 Dynamic simulation

The DC response of the model is investigated by applying a sudden perturbation to the operating current. Before and after the perturbation, the computational model is left to stabilize to a steady-state. The results of the simulation are presented in section 5.2.

The use of time steps below 0.1 ms caused numerical issues in terms of singularities in the model. This problem was not resolved, and so the simulation is performed with a time step of 0.1 ms. As a result, the model will not be able to simulate effects with a characteristic time constant < 0.1 ms, even if they are included in the analytical model described above.

Table 4.4: Model constants.

Symbol	**Value**	**Unit**	**Description**	**Ref.**
$A_{\Psi_{H_2}}$	$7.19 \cdot 10^{-13}$	mol/cm s Pa	Pre-exponential hydrogen permeability factor	This work
$A_{\Psi_{O_2}}$	$7.28 \cdot 10^{-14}$	mol/cm s Pa	Pre-exponential oxygen permeability factor	This work
$\bar{C}_{\mathrm{p,L}}$	75.97	J/mol K	Liquid water molar heat capacity at constant pressure	[9]
$\bar{C}_{\mathrm{p,V}}$	33.40	J/mol K	Water vapor molar heat capacity at constant pressure	[9]
$D_{\mathrm{H_2O}}^{\mathrm{ref}}$	1.54	$\mathrm{cm^2/s}$	Diffusion coefficient in anode PTL	[86]
$E_{a,D}$	20 000	J/mol	Water diffusion activation energy, $f \leq 0.45$	[91]
$E_{a,\kappa}$	15 000	J/mol	Proton conduction activation energy, $f \leq 0.45$	[84]
$E_{a,\xi}$	4 000	J/mol	Electroosmotic drag activation energy	[84]
$E_{a,\Psi_{H_2}}$	21 010	J/mol	Hydrogen transport activation energy	This work
$E_{a,\Psi_{O_2}}$	17 022	J/mol	Oxygen transport activation energy	This work
$E_{\mathrm{HER}}^{\mathrm{ref}}$	0	V	Standard state activation energy for HER	[23]
$E_{\mathrm{OER}}^{\mathrm{ref}}$	1.23	V	Standard state activation energy for OER	[23]
$\bar{H}_{\mathrm{L,t}}$	0	J/mol	Liquid water molar enthalpy	[9]
$\bar{H}_{\mathrm{V,t}}$	45 045.3	J/mol	Liquid water molar enthalpy	[9]
$k_{\mathrm{M \to L}}$	$27.75 \cdot 10^{-3}$	$\mathrm{mol/J\,cm^3\,s}$	Rate constant, membrane-bound to liquid phase	[91]
$k_{\mathrm{M \to V}}$	$5.55 \cdot 10^{-5}/M_{\mathrm{H_2O}}$	$\mathrm{mol/J\,cm^3\,s}$	Rate constant, membrane-bound to vapor phase	[91]
k_{sat}	$1.8 \cdot 10^{-14}$	$\mathrm{cm^2}$	Water permeability for completely saturated membrane	[84]
p_{ref}	1	bar	Reference pressure	This work
p_{t}	611.2	Pa	Triple point pressure of water	[9]
T_{ref}	303.15	K	Reference temperature	[84, 91]
T_{t}	273.16	K	Triple point temperature of water	[9]
γ	0.076	N/m	Water liquid-gas surface tension	[9]
$\varepsilon_{\mathrm{aPTL}}$	0.4		Anode PTL porosity	[86]
θ	90.02	°	Water contact angle	[84]

Chapter 5

Model results and analysis

Electrolyser operation was simulated both for steady-state and dynamic electrolyser operation. Model properties of interest in both cases were:

1. The predictive abilities of the model for measurable phenomena, such as simulated polarization curve accuracy, under a range of different operating conditions.
2. The diagnostic abilities of the model for various phenomena that are difficult to measure, such as water saturation profiles in the membrane under a range of different operating conditions.
3. Limitations of the model in terms of e.g. simplifications made to reduce computational complexity and numerical accuracy.

5.1 Steady-state simulations

In this section, the results of the simulations for the steady-state case are presented. To validate the model, simulated and experimental polarization curves are compared, and the model is curve fitted to match experimental data. Then, simulated effects of elevated cathode gauge pressure and varying anode air stream RH on water transport in the membrane are presented and discussed. Finally, the combined effect of varying gauge pressure and RH on water transport in the membrane is examined.

5.1.1 Polarization curve validation

Simulated polarization curves after curve fitting are shown in figure 5.1 and 5.2. Figure 5.1 shows the simulated polarization curve for the steady-state case, for varying cathode gauge pressure, with superimposed experimental data from measurements carried out at the Norwegian Fuel Cell and Hydrogen Centre, SINTEF, in 2022. The experimental measurements were taken for a PEM electrolyser of 25 cm^2, at an operating temperature of 333 K, with an applied gauge pressure of 0, 2, and 5 bar. The experimental electrolyser did not use a Nafion membrane, but rather a Gore-Select membrane: a reinforced composite membrane with an additional mechanically stable porous matrix, helping to alleviate structural membrane issues for high temperature operation.

Figure 5.2a shows simulated polarization curves for the specific three gauge pressures corresponding to the experimental cases, plotted together with the experimental data. The simulated polarization curves have the typical form where the cell voltage is dominated by the reaction energies for low current densities, and linear resistive losses dominate for increasing current densities. However, it is evident from figures 5.1 and 5.2a that the model after curve fitting does not completely agree with experimental results.

It is a well-known phenomenon that elevated pressure increases cell voltage, an effect which appears to be captured by the model for lower current densities, but for increasing current densities, the elevated cathode pressure appears to have the opposite effect. For low current densities where transport and ohmic losses are less significant, the simulated polarization curves follow the predicted behaviour, however the polarization curves slope downward with increasing pressure. In both figure 5.1 and 5.2a, the polarization curves slope increasingly downward for higher current densities, intersecting the 0 barg curve for a current density of ~ 2 A/cm^2. Thus it appears that the model is estimating a lower net resistance for increasing pressure, a behaviour which is not observed in the experimental results.

Figure 5.2b and 5.2c show the simulated voltage losses separately in the electrodes and membrane. From figure 5.2b it is clear that the voltage loss in each electrode, which in the model is associated only with reaction kinetics, agrees with the state-

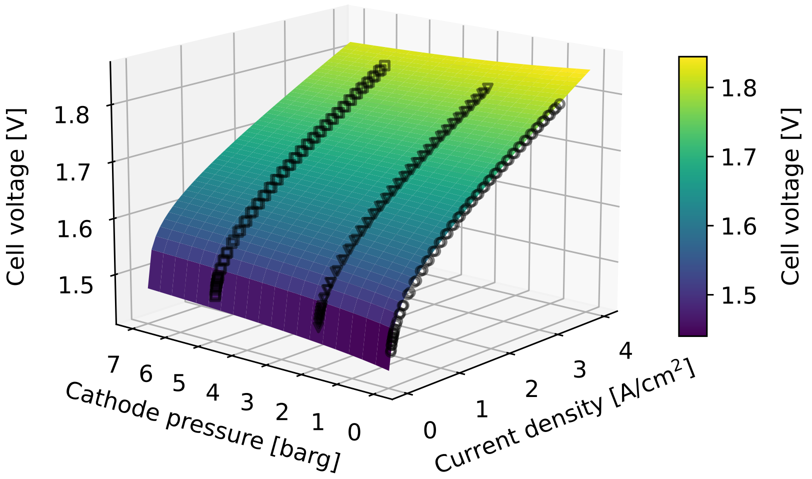

Figure 5.1: Simulated polarization curves for a range of cathode gauge pressures, at 333 K and 100% RH. Experimental data for 0, 2, and 5 barg are superimposed over the simulation plot in black.

ment above that elevated pressure increases voltage loss. The simulated voltage loss in the membrane as shown in figure 5.2c, however, decreases with increasing pressure. Based on the two figures it may then be concluded that the error lies within the membrane model, with the transport of protons being overestimated for elevated gauge pressures. Further discussion of possible causes of this error is performed in section 5.1.2.

Since the model predicted an erroneous trend for elevated pressures, the simulated polarization curve for 0 barg in figure 5.2a was curve fitted to the experimental data, and the pressure kept ambient in the simulations in the remainder of the paper where pressure effects were not the main point of interest. In simulations where a varying differential pressure was necessary, a current density of 1 A/cm^2 was applied, to ensure that the pressure effect on system performance corresponded to that observed experimentally.

Curve fitting of the steady-state model was performed via the conductivity prefactor κ_0, and the exchange current densities $i_{0,\mathrm{HER}}$ and $i_{0,\mathrm{OER}}$, and a good fit of experimental data was found for the coefficient values in table 5.1. The curve fit values

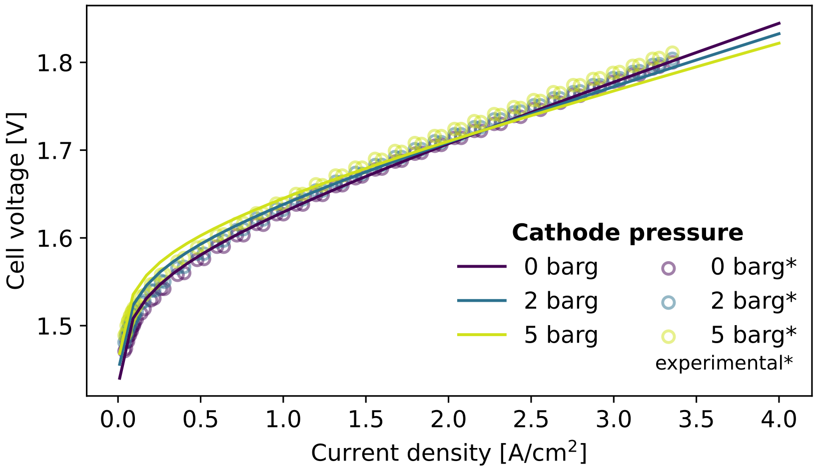

(a) Simulated polarization curves for differential pressure operation, with cathode gauge pressure of 0, 2, and 5 barg. Experimental data is plotted as empty circles, with the same color as the corresponding simulated curve.

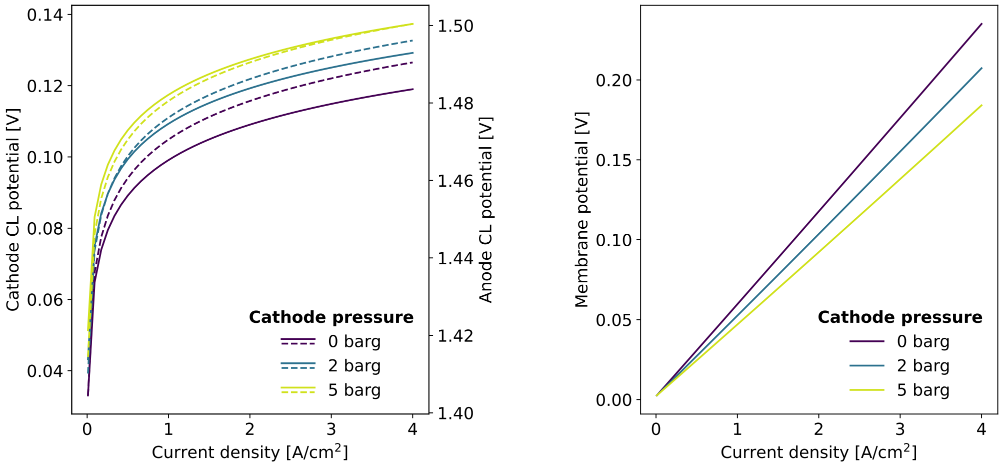

(b) Effect of elevated pressure on voltage losses in the cathode (solid line) and anode (stippled line) CLs.

(c) Effect of elevated pressure on voltage losses in membrane.

Figure 5.2: Effect of elevated pressure on the polarization curve, and the voltage losses in the electrodes and membrane, for 0, 2, and 5 barg, at 333 K and 100% RH.

for both exchange current densities are slightly on the higher side, though within the range of values reported by other studies. [15] Furthermore, values reported in literature are often curve fit values depending on the model in question, and can range over several orders of magnitude. [1]

Table 5.1: Empirical fit coefficients for model polarization curve, for fitting to experimental data at 333 K, 0 barg cathode gauge pressure, and 100% RH anode air stream.

Symbol	**Value**	**Unit**	**Description**
κ_0	0.128	S/cm	Membrane proton conductivity prefactor
$i_{0,\mathrm{HER}}^{\mathrm{ref}}$	1	$\mathrm{mA/cm^2}$	HER reference transfer current density
$i_{0,\mathrm{OER}}^{\mathrm{ref}}$	25	$\mathrm{nA/cm^2}$	OER reference transfer current density

The conductivity prefactor depends on the microstructure of the membrane, and will therefore vary depending on the membrane used in the experiment. The obtained value is of the same order of magnitude as the prefactors used by Weber & Newman [84] and Zenyuk et al. [91], though it holds a lower value. Though the experimental polarization curves were not obtained using a Nafion membrane, the properties of the Gore-Select membrane were assumed to be comparable to Nafion. The presence of the porous matrix is known to cause a significant decrease in membrane conductivity and hydraulic permeability, [28] therefore a lower conductivity prefactor is physically justifiable.

5.1.2 Elevated pressure effect on water penetration in the membrane

Figure 5.3 shows simulated saturation profiles and membrane conductivities for a range of linearly spaced gauge pressures between 0 and 7 barg, with the experimental cases of 0, 2, and 5 barg plotted as stippled black lines. The saturation profile for 0 barg in figure 5.3a shows that for all the tested gauge pressures, all of the channels in the membrane are able to expand with liquid water on the cathode side. For increasing pressure, a larger portion of the membrane becomes fully saturated with water, though as can be seen by the spacing of the saturation profiles, the fraction of the membrane which is fully liquid-saturated does not increase linearly with pressure. This can be attributed to the resistance posed by the then displaced water vapor of the air stream. Membrane proton conductivity in figure 5.3b is simulated to vary with pressure in a similar fashion as the local water saturation, which naturally follows from the model definition of the conductivity in equation (4.24).

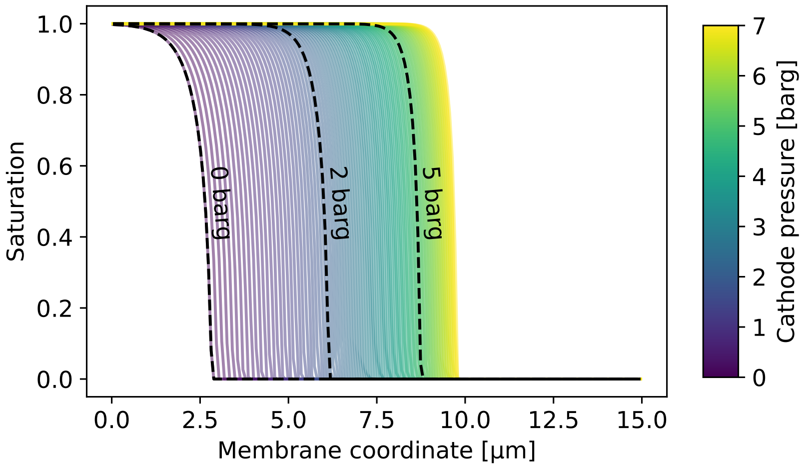

(a) Simulated effects of varying the gauge pressure on local membrane water saturation.

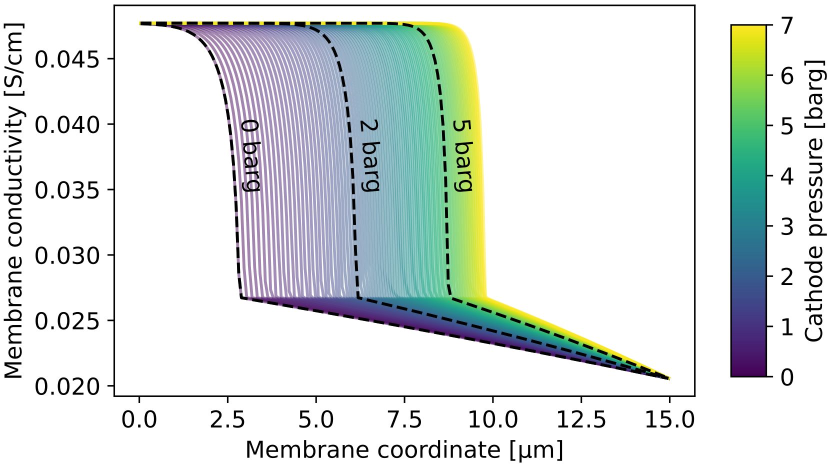

(b) Simulated effects of varying the gauge pressure on local membrane proton conductivity.

Figure 5.3: Simulated effects of varying the gauge pressure on local membrane water saturation and conductivity, with a constant operating temperature of 333 K, current density of 1 A/cm^2 and 100 % RH anode air stream.

The effect of elevated pressure on water saturation and proton conductivity may provide some insight into the cause of the discrepancy between model and experimental polarization curves in figure 5.1 and 5.2. In the model, elevated pressure affects both the reaction kinetics via the activation energies E_{HER} and E_{OER}, and the transport processes. Kinetic effects are modeled only in the CLs while transport takes place only in the membrane.

It is apparent from figure 5.3a that the rising pressure gradient causes liquid water to penetrate further into the membrane from cathode to anode. The presence of liquid water in a larger part of the membrane results, as shown in figure 5.3b, in a lowered resistance to transport of protons, via the saturation dependence in the transport parameter model equations. A lowered resistance in turn leads to a decreasing voltage loss over the membrane with increasing pressure, leading to the results in figure 5.2c. When the influence of water saturation on the model conductivity is large enough, the elevated pressure effect of increased reaction activation energies is negated by the facilitation of transport.

Observations of decreased mass transport losses in the membrane with increased pressure have been recently reported in literature, by Martin et al. [49] who reported a significant decrease in the mass transfer overpotential for increasing pressure between 1 and 15 bar, and by Garbe et al. [25] who report that several recent studies have observed increased membrane performance with increasing pressure, attributed to the concentration and retention of water in the membrane.

Conductivity of Nafion membranes has been observed to be highly dependent on water content in the membrane. [92] Based on the assumption that the Gore-Select membrane has a similar general structure as Nafion except for the reinforcing matrix, and the proton conduction mechanisms are the same, the water content dependence was assumed to hold for the Gore-Select membrane, so that the functional form of the dependence on water content in the model expression for proton conductivity κ remains valid.

However, though there appears to be a wide consensus regarding the effect of water content on membrane conductivity, some contradictory results are to be found in literature. Mališ et al. [47] report that the observed conductivity of the membrane did not follow the expected Arrhenius dependence, and suggest the existence of a low-temperature (30°C to 70°C) regime where the activation energy of proton conduction is much lower than for higher temperatures.

For the water transport coefficient, there are fewer reported findings as this parameter represents a modified diffusion or permeability coefficient, as described in the previous chapter. Though the model value is based on empirical relations for the water permeability and water diffusion coefficient of the membrane, it was not considered as a fitting parameter during the curve fitting of the model. It is therefore possible that an adjustment of the expression for the water transport coefficient would provide better agreement with the experimental data.

To summarize, as the simulated membrane water uptake with increasing pressure appears to agree well with the findings of other researchers, it is suggested that the cause of the erroneous high-pressure behavior in figures 5.1 and 5.2a is that some parameter associated with the effect of pressure on water penetration, or of water penetration on proton conductivity, has been overestimated in the model. The most likely candidates are the proton conductivity κ and the water transport coefficient α, where the water transport coefficient was not treated as a curve fitting parameter in the present study and should be re-evaluated in future work.

5.1.3 Relative humidity effect on voltage losses in the electrolyser

In order to ensure the efficiency of the electrolyser, it is important that there is a sufficient amount of water available on the anode, to avoid inhibiting the OER. With the novel method of supplying water on the cathode and humidified air on the anode, it is therefore interesting to try to predict the transport of water from cathode to anode, for a varying humidification of the anode air stream.

Simulated polarization curves for varying RH of the anode air stream are shown in figure 5.4a. The model predicts an increasing cell voltage with decreasing humidification, and the effect is most significant for higher current densities. Figure 5.4b-i shows saturation profiles in the membrane for anode air stream RH between 60% and 100%, at an operating current density of 1 A/cm^2 and ambient pressure. Figure 5.4b-ii provides an enlarged view of the first quarter of the membrane, allowing closer examination of the saturation profiles close to the cathode boundary.

The modeled mechanisms of water transport under varying RH conditions can be

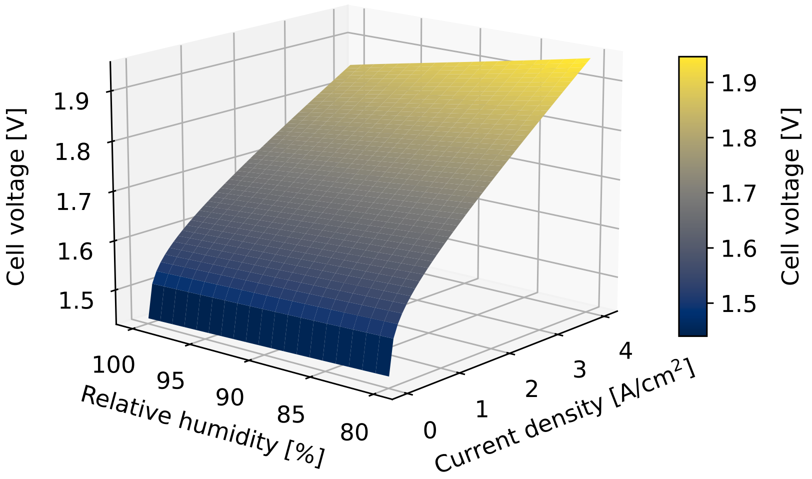

(a) Simulated polarization curves for a range of anode air stream RH.

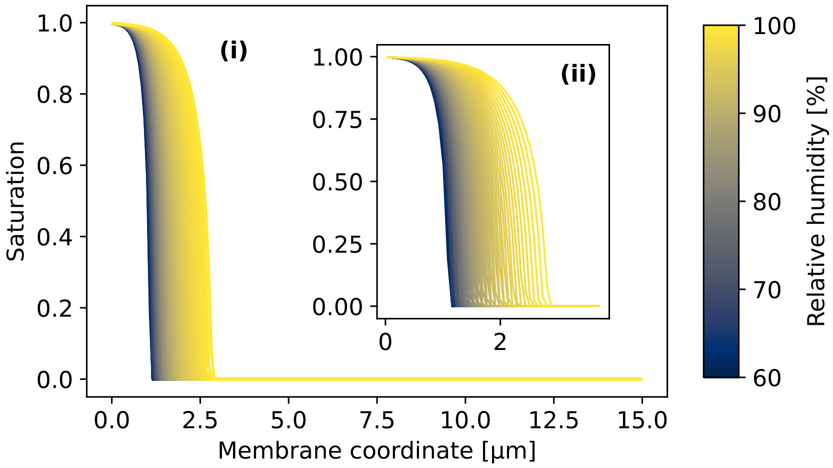

(b) Simulated effects of varying RH on local membrane saturation, at an operating current density of 1 A/cm^2.

Figure 5.4: Simulated effects of varying the RH of the anode air stream on polarization curves and membrane saturation, with a constant operating temperature of 333 K and ambient pressure.

explained as follows: Decreased RH leads to a lower concentration of water on the anode CL-PTL boundary, as there is less water available to diffuse through the anode PTL. The decrease in anode PTL water concentration in turn leads to less water transferring from vapor phase in the anode PTL to the PEM on the boundary, as the difference between the chemical potential of water in the membrane and anode PTL decreases. The increased water concentration gradient within the membrane then induces an increased flux of water towards the anode.

However, the simulated results predict less liquid water in the membrane with reduced RH. From figure 5.4b it is evident that the fraction of the membrane which is fully liquid-saturated diminishes with decreasing saturation. This indicates that the effect of electroosmotic drag of water by protons becomes stronger than the effect of the diffusive driving force when more of the membrane is vapor-equilibrated, leading to a shift of the saturation profile towards the cathode. The suggested explanation agrees with other modeling efforts: Electroosmotic drag was found to be significant also by Myles et al. [53], as it dictates the flux of water from cathode to anode that is necessary to avoid membrane dehydration at the anode. The water flux through the membrane has been experimentally found to decrease by a factor of 2 between 100% and 80% for PEM fuel cells, [46] further supporting the validity of the model results.

With less liquid water in the membrane, the model assumes that transport of protons will be significantly inhibited, raising the cell voltage. Conductivity of Nafion membranes has been shown to depend significantly on RH for hydrogen PEM fuel cells, [92] which again agrees with the simulated results, providing knowledge of proton transport mechanisms is transferable between fuel cells and electrolysers, and between Nafion and Gore-Select membranes.

However, the simulated increase in cell voltage does not match that which was observed experimentally for the thin-membrane cathode-feed electrolyser during in-house measurements: While there is a clear increase in simulated cell voltage for a decrease in RH, previous in-house experiments demonstrated a reduction of the anode air flow RH all the way down to 36% without a significant effect on the polarization curve. The lack of change in voltage loss for the in-house experimental polarization curve suggests that there is was all times a sufficient amount of water so that reactions and transport are not impeded.

Due to the conflicting results from literature and in-house measurements, it is hard state conclusively whether or not the simulated effect of RH agrees with expected results. On one hand, the predicted results agree with findings of several other authors, who report that lower RH has a significant effect on cell voltage and membrane saturation. However, at least for the specific thin-membrane cathode-feed electrolyser, the model appears to overestimate the effect of RH on the ability of water to penetrate the membrane.

5.1.4 Combined effect of pressure and relative humidity on membrane water penetration

Finally, as both gauge pressure and the RH of the anode air stream can be varied under electrolyser operation, it is interesting to investigate the interplay of varying the two operating conditions simultaneously. Figure 5.5 shows the fraction of the membrane fully saturated with water for a range of gauge pressures and anode air stream RH, with a cutoff limit of 1% so that any point in the membrane with a saturation larger than 99% was considered to be fully saturated. With the applied operating current of 1 A/cm^2, the simulated cell voltage of the electrolyser follows the experimentally observed trend with increasing cathode gauge pressure, so the uncertainty associated with pressure-driven transport and losses for varying pressure discussed in section 5.1.1 need not be considered when analysing the results of this simulation.

From figure 5.5, it can be observed that both pressure and RH are expected to have a significant effect on the water penetration in the membrane. The effect of pressure is more dominant than that of RH, as there is little variation with decreasing RH at low pressures, but a significant variation with increasing pressure at lower RH, indicating that elevated pressure operation can compensate for small variations in air flow RH and keep the membrane well hydrated, so long as the variations are small.

As previously discussed, there are both experimental data and modeling results in literature that supports the model results for varying cathode gauge pressure and RH. However, taking into account the experimentally observed independence of the membrane saturation on the RH during in-house measurements, the expected result for the thin-membrane electrolyser under consideration would be an invariant saturation in the direction of the RH-axis, while changes in saturation are dominated by changes in pressure.

The validity of the predicted water penetration of the membrane is subject to the same discussion presented earlier in this chapter, for the case of varying pressure and RH. Due to the lack of experimental results to compare to the simulation, an experimental investigation into the interplay of these two operating conditions is identified as a potential future area of research, both for conventional and the thin-membrane cathode-feed electrolyser.

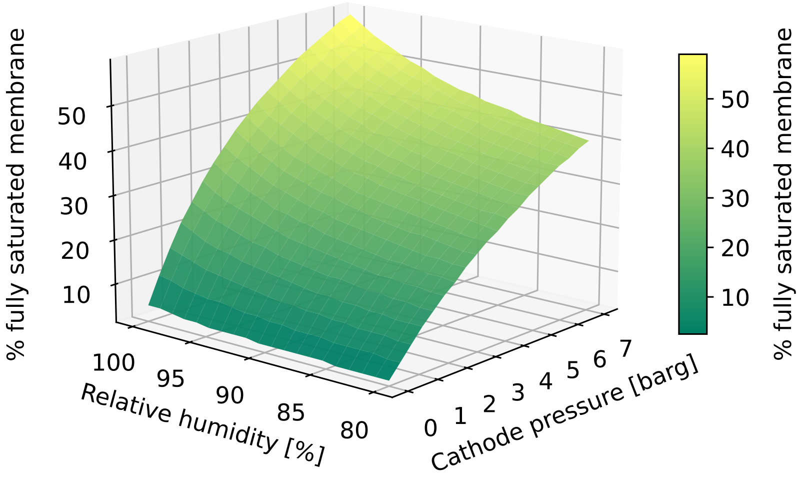

Figure 5.5: Simulated fraction of membrane fully saturated with liquid water, for a range of gauge pressures and anode air stream RH, at 333 K and operating current density of 1 A/cm^2.

5.2 Dynamic simulation

The curve fitted steady-state model was converted to a transient model as described in section 4.6. Based on the results for the steady-state case, the applied current was kept around 1 A/cm^2 for all simulations, and the gauge pressure and anode air stream RH at 0 barg and 100% respectively. As mentioned in the previous chapter, the lower limit of time step that was possible in the model, 0.1 ms, results in a predicted inability to model several electrical phenomena in the electrolyser, and thus a larger focus was placed on mass-transfer, low-frequency effects.

The model voltage response to a sudden step change in operating current density is shown in figure 5.6. Before the perturbation, the applied current density was 1 A/cm^2, and the step increase was of the magnitude 0.1 A/cm^2. For comparison, the operating current density is superimposed onto the voltage response.

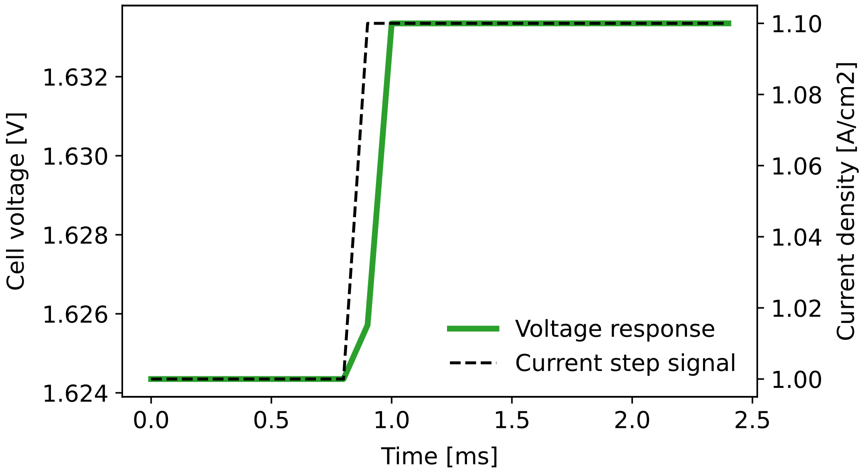

Figure 5.6: Electrolyser voltage response (green solid line) to an applied current step perturbation (black stippled line) of 0.1 A/cm^2 to operation at 1 A/cm^2, at ambient pressure, 333 K and 100% RH.

By comparing the applied current signal to the simulated voltage response, it is evident that the model predicts a small delay after the perturbation, before the system reaches a state of approximate stability. The delay visible in figure 5.6 is around 0.2 ms, but a close inspection of the data shows that the system is not completely stabilized until the 3.6 ms mark, i.e. 2.7 ms after the perturbation.

Various time constants related to charge and mass-transfer have been reported across literature, and indicate that the processes are not always easily distinguished based on time constants alone. For example, water sorption into the membrane has been reported to have a characteristic time of $\sim$ 0.5 ms, [46] electrochemical time constants have been reported as 0.5 – 5.5 ms, [34] and diffusion time constants of between 0.05 – 0.25 s [34] can be found in literature.

While the simulated time delay is on the order of magnitude of the former of these, mass-transfer processes are expected to have a larger effect on the time delay than electrical effects. Furthermore, as the modeling equations indicate, the time response of the HER and OER is instantaneous in the 0D CLs even for transient simulations, and only transient effects related to transport in the membrane is included in the model. Thus it is concluded that the time delay for the most part can be attributed to mass-transfer effects in the membrane and/or anode PTL.

5.3 Convergence

Besides the application of a multiphysical modeling approach to PEM electrolyser modeling, an objective of the thesis was to examine implications of using exclusively open-source software for modeling with regards to the complexity of the modeling problem. This section presents the discussion of some key model insights and takeaways which may help to highlight advantages and disadvantages of the approach for this particular modeling task.

Due to the mutual dependence of PDE variables on transport parameters and vice versa, the model required iteration to convergence. Figure 5.7 shows the result of a convergence test, performed by letting the steady-state model system evolve for a large number of iterations, and tracking the value of the residual as a function of the number of iterations.

Convergence tests were performed for a cathode gauge pressure of test cases 0 and 5 barg, both with applied current densities of 1 and 4 A/cm^2. Figure 5.7 shows that the model struggled significantly more with convergence for elevated pressure than ambient pressure, where the model required around 50 iterations more to reach convergence, but only slightly more for elevated current density in both cases. Convergence was slowest for the case of both elevated cathode pressure and current density. The residual for any case does not reach a value of less than 10^{-9}.

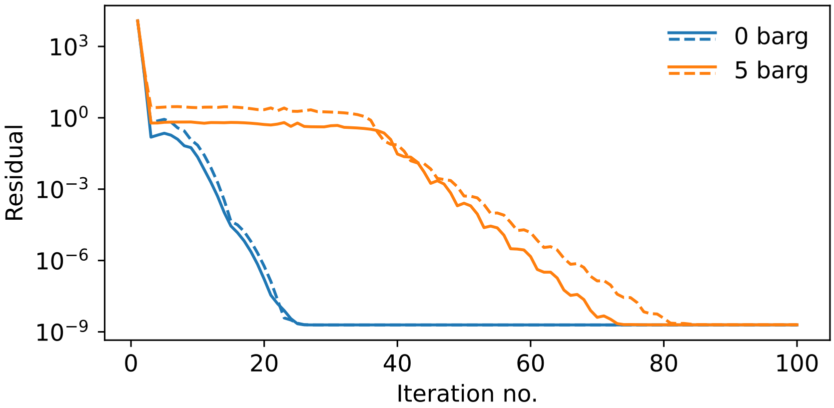

Figure 5.7: Steady-state model convergence in terms of residual from solution sweep, for gauge pressures of 0 (blue) and 5 barg (orange), and operating current densities of 1 (solid line) and 4 A/cm^2 (stippled line).

In the dynamic simulation, the system was first solved to steady-state convergence before applying any perturbation. When applying current density perturbations, the model consistently required only one iteration to solve the system to convergence for each time step, indicating a linear behaviour of the system for the applied perturbations.

As the system was able to converge fast for both the steady-state and dynamic simulation, it is concluded that the open-source software is powerful enough for the modeling of electrochemical systems of a certain complexity. However, with attempts to add more mutually dependent parameters than presently included, a significant effect on convergence and computation time was noted. As previously mentioned, the accumulation terms in equations (4.65) and (4.66) required manual discretization and treatment as transient sources. Attempts to include more complicated boundary conditions resulted in convergence to no less than the order of ~ 1, even with several hundred iterations. Furthermore, introducing more mutual dependencies caused the residual not to converge as in figure 5.7, but to oscillate around some higher value. It appears then that the complexity of the model implemented in this thesis is nearing the practical limit of such software.

5.4 Model limitations

In addition to agreement with experimental results, convergence, and computation time, issues such as range of validity and difficulty of implementation are of interest in order to provide satisfactory answers to the key points of interest stated at the beginning of this chapter.

The CLs and PTLs were significantly simplified in the computational model. As described in section 2.4, the PTLs, CLs and membrane are significant in terms of their contributions to electrolyser performance, in large part due to impacts of their hydration, and their micro-scale geometry, on transport of reactants and products to and from the reactive sites. The anode PTL model provides a highly simplified picture of transport of water through the porous structure, neglecting both convective flow, and product gas diffusion and flow, while the CLs are even further simplified.

As argued in chapter 3, reducing the CLs to a single point in space leaves no possibility for insight into processes such as transport in each phase, reaction distributions, or the effect of the presence of water. Furthermore, though several of the models in table 3.1 represented the CLs as 0D boundaries between the PEM and PTLs, the justification for this simplification was that the CLs were much thinner than the other components. In other models, a CL with a thickness of ~ 10 μm made up usually less than 10% of the width of the membrane, but for this simulation where the thickness of the membrane is comparable to the thickness of the CLs, the justification does not carry the same weight.

Due to both the length of the time step which was necessary, and the lack of any surface charge term in the transient charge conservation equation (4.66), the computational model does not satisfactorily simulate transient electrical effects. Thus, it must also necessarily be termed a "dynamic steady-state" model as defined in chapter 3, though it differs from most other such models in literature in that usually dynamic temperature is considered in order to examine heat flow in and out of the system, while the present model considers dynamic mass-transfer effects occurring on a smaller time scale than heat transfer. [81]

The use of open-source software was found to have both advantages and disadvantages. As described in chapter 4.8, most of the labor associated with manual discretization of the system was taken care of by the software, in a similar manner to specialized software. Little added modeling complexity, other than the need for a non-finite-difference differentiation for discontinuous variables, was experienced during the course of these modeling efforts. The main challenge was associated with the lack of built-in controls which ensure the correct input type is given to built-in modules. Another issue was the lower limit that appeared on the minimum time step, though in the end the cause of this limitation was not discovered, and is not a general feature of the software.

In conclusion, the use of open-source software for complex electrochemical systems modeling can certainly be comparable to specialized commercial software, though considerations will have to be made for each modeling case. For example, this particular implementation did not permit modeling of transient electrical phenomena, which were originally of interest for the modeling work.

Chapter 6

Conclusions

This thesis discusses the application of multiphysical modeling principles, originally developed for PEM fuel cells, to the field of PEM electrolysers. The objective was to demonstrate how a multiphysical treatment may provide insight into how processes within the electrolyser affects its performance. A secondary objective was to implement the model using exclusively open-source software in order to test the applicability of freely available open-source technology to modeling of the complex electrolysis process.

Specifically, a 1D multiphysical computational model was developed for a PEM electrolyser of a novel, promising type. The electrolyser configuration is unusual in that the water is supplied on the cathode, humidified air is supplied on the anode, and the PEM itself is significantly thinner than in conventional electrolysers.

Key physical, thermodynamical, and electrochemical foundations were presented, and a previous review of computational modeling approaches in literature was revisited in order to provide an understanding of the state of the art for modeling of PEM electrolysers. The review concluded that while most electrolyser modeling efforts to date have been concerned with 0D models, researchers have begun increasingly to apply multi-dimensionality in their modeling efforts. Some areas of interest for further development of PEM electrolyser modeling were identified, particularly the introduction of transient electrolyser operation with regards to capacitive electrical effects, and the capabilities and simplicity of use of open-source software.

The predictive abilities of the steady-state model were tested via the simulation of a polarization curve for cases corresponding to in-house experiments. The model was found to predict a polarization behavior which agrees with experimentally observed data for the case of ambient pressure, but for increasing cathode gauge pressure and higher current densities, the model predicted an improvement of electrolyser performance with increasing pressure which was not observed in experiments. Curve fitting of the model to experimental data was therefore performed for the baseline case of ambient pressure.

The diagnostic abilities of the model for internal phenomena were demonstrated by examining in detail the contributions of the CLs and membrane to the voltage losses in the model electrolyser, and water saturation profiles through the membrane, for varying cathode gauge pressure. It was found that the voltage loss contributions from the electrochemical reactions increased, while the membrane predicted lower overall voltage loss, with increasing pressure. The saturation profile simulation predicted increased penetration of liquid water through the membrane with increasing pressure, providing an explanation for simulated increase in the conductivity and subsequent lowering of the voltage loss over the membrane. The simulated results were qualitatively in agreement with reports from the literature. However, an overestimation of the effect of water penetration on voltage losses within the membrane was identified, proving the need for further tuning of the model.

Predicted polarization curves and saturation profiles were also simulated for varying anode air stream RH, and for this case the model was found to predict increased cell voltage with decreasing RH, an effect which has been reported in literature, but again was not observed for the thin-membrane electrolyser during in-house experiments. Studying the corresponding simulated saturation profiles, the model behavior was traced to a decline in the fraction of membrane saturated with liquid water with decreasing RH, and it was stipulated that the model is likely to overestimate the effect of electroosmotic drag of water towards the cathode when the water in the membrane comes from water vapor.

During analysis of the sensitivity study, it became evident that there is some disagreement between various experimental observations, both published and in-house. The 1D multiphysical modeling of internal phenomena and local conditions in the membrane enabled not only a physical representation of processes occurring within the electrolyser, but by studying the simulated local behaviour in comparison to the theory it was possible to provide suggestions, based on a physical intuition, for how and why the model predicted results in disagreement with observations, and to identify areas for further research.

For dynamic electrolyser operation, system response for perturbation of the applied current were studied. The model predicted a small delay in the voltage response of the electrolyser to a current step perturbation, which was attributed to transport of water in the membrane. However, computational limitations on the time step length caused an inability of the model to predict the behavior of processes with shorter characteristic times.

The use of open-source instead of commercial software was concluded to contribute both advantages and disadvantages to the modeling work. Significant benefits included that as quite powerful, freely available solvers have now been developed, research becomes more accessible and transparent even for those with less computational experience. Providing that the syntax is simple enough to implement and read, time and resources can be spent on research rather than on programming. Drawbacks of the open-source software were that the lack of user interface resulted in less transparency, when encountering issues not described thoroughly in the documentation.

6.1 Future work

The case was made in the introduction for the importance of computational modeling for furthering research and accelerating the green energy transition. This thesis has presented advantages of a multi-dimensional, multi-phase modeling for complex electrochemical systems such as the PEM electrolyser, and provided some tools in terms of the discussion of the physics behind the processes, and how to approach making simplifications to reduce the complexity of modeling efforts.

As multiphysical modeling and model validation can greatly add to the understanding of emerging technologies, such as the PEM electrolyser considered in this paper, they should constitute a natural part of research and development. In this final section, selected suggestions for future work are listed. The topics mentioned here do not constitute a comprehensive list, but are intended as a summary of some specific findings associated with the present work.

6.1.1 Model improvements

The modeling work identified some disagreement between simulated and experimental polarization curves, which was attributed to an overestimation of the effect of a cathode gauge pressure on the penetration of water in the membrane. A natural continuation of this work is to further develop the model to achieve better agreement between simulated and experimentally observed behavior, by further tuning of modeling parameters and/or incorporating more detailed water management in the membrane model.

The electrolyser model included a comprehensive multiphysical implementation of the membrane, while CLs were simplified as 0D boundaries. Fully saturated cathode PTL and diffusive non-interacting water vapor transport only in the anode PTL were assumed. Based on the argument for the advantages of multi-dimensional modeling compared to 0D, which has been made several times throughout the thesis, future improvements to the model could thus involve expanding the model with multi-dimensional multiphysical representations of also the CLs and PTLs.

Furthermore, product gas crossover in the membrane was implemented in the model but not studied in detail as the thesis focused more on the effects of internal phenomena on electrolyser performance, and computational aspects of multiphysical electrolyser modeling. As one of the key advantages of the cathode liquid-, anode air-feed electrolyser is the alleviation of crossover issues, further studies should include the effect of variable operating conditions on anode hydrogen concentration.

Several meaningful additions to the phenomena considered could further be implemented, among them the incorporation of transient capacitive electrical effects, energy transport and thermal effects in the cell components, degradation mechanisms and lifecycle of the electrolyser, and integration with intermittent energy production systems. Many of these features may be implemented taking as a starting point the general physical, thermodynamical, and electrochemical framework which has been presented. In order to implement transient electrical effects, the issue of the lower limiting time step of the model must first be remedied.

With the implementation of more detailed transient phenomena in the electrolyser, further analysis of the system, e.g. electrochemical impedance spectroscopy (EIS) in order to examine rate-limiting processes in the electrolyser, becomes interesting. In EIS, the complex impedance of the system is analysed by first measuring the voltage response of the electrolyser to a sinusoidal current over a range of frequencies, converting the signal and response to the frequency domain, and calculating the impedance via Ohm's law. The method can help to deconvolute the various processes and sources of resistance within the electrolyser based on their characteristic time scale. A prerequisite for EIS modeling is linearity of the system, which has been concluded to be satisfied by the model, for perturbations of low amplitude.

6.1.2 Other studies

In addition to improvements to the computational model, some areas of interest have been identified as suggested topics of future research for the field of PEM electrolysers and computational modeling in general. Several of the studies mentioned here may be useful also to other fields, especially PEM fuel cell research and modeling.

Modes of transport in the PEM

The general consensus regarding water transport in PEMs is that there are three main modes of water transport: diffusion, pressure-driven and electroosmotic. Many modeling frameworks in literature, both for electrolysers and fuel cells, are based on this consensus for pressure-driven flow. However, as indicated by findings from both this thesis and other works [21], the extent of pressure-driven water flow in PEMs can in certain cases be drawn into question. For development of this and future computational models, both computational and experimental research into water penetration at elevated pressures would be of great use.

Interplay between pressure and relative humidity

A further need for experimental studies into the interplay between elevated cathode gauge pressure and RH of the anode air flow was pointed out in section 5.1.4. The need for this research is founded in the conflict between the simulated performance of the model and in-house measurements on the thin-membrane cathode-feed electrolyser, in order to investigate the agreement between established conventions in the field of electrolyser modeling, and the performance of the novel electrolyser.

Transient electrical effects during electrolyser operation

The emergence of electrolysers as a promising method of energy production in connection to intermittent renewable energy sources provides motivation for further studies into transient electrolyser response to changing operating conditions. Electrical effects have so far received the least attention, though some work has been performed for fuel cells. [37, 86, 87] Furthermore, many experimental methods involve some sort of transient operation of the electrolyser, however corresponding simulations are rarely seen in literature. By working to give computational models the ability to reliably predict the outcome of experiments, time-consuming and expensive research could in many cases be avoided.

Development of open-source software

Though there are certain challenges associated with the use of open-source software, continued efforts in development, improvement and documentation of powerful, publicly available software and solvers is key in lowering the threshold for the inclusion of electrolyser models with a higher complexity in research and development. For the continued advancement of multiphysical electrolysis modeling, one of the important measures will be to increase the accessibility of tools to facilitate the computational process in a reliable way. This includes development of new packages and solvers which are powerful enough to solve complex systems with circular dependencies, integrable with one another, and well documented. As demonstrated in this paper, computational tools do not need to be specifically developed for electrochemical systems modeling to be applicable.

Appendices

Appendix A

Nomenclature

A.1 Abbreviations

0D, 1D, 2D, 3D	Zero-, one-, two-, or three-dimensional
BPP	Bipolar plate
CC	Current collector
CCM	Catalyst-coated membrane
CCS	Catalyst-coated substrate
CFD	Computational fluid dynamics
CL	Catalyst layer
DFM	Dusty fluid model
EIS	Electrochemical impedance spectroscopy
EMR	Energetic macroscopic representation
GDL	Gas diffusion layer
HER	Hydrogen evolution reaction
MEA	Membrane-electrode assembly
MPL	Micro-porous layer
OER	Oxygen evolution reaction
PDE	Partial differential equation
PEM	Proton exchange membrane
PFSA	Perfluorinated sulfonic acid
PTL	Porous transport layer
RH	Relative humidity
SPE	Solid polymer electrolyte

A.2 Symbols

A.2.1 Latin

Symbol	**Description**	**Unit**
a	Activity	
a	Interfacial volumetric surface area	1/cm
$\mathbf{A}$	Antidifferentiation matrix operator	
c	Concentration	mol/cm^3
$\bar{C}$	Heat capacity	J/mol K
D	Diffusion coefficient	cm^2/s
$\mathbf{D}$	Differentiation matrix operator	
E	Open circuit voltage	V
	Activation energy	J/mol
$\mathbf{E}$	Error penalty matrix	
f	Water volume fraction	
$\boldsymbol{f}$	Original data in Tikhonov regularization	
F	Faraday's constant	s A/mol
ΔG	Gibbs reaction energy	J/mol
$\boldsymbol{g}$	Gradient vector	
$\bar{H}$	Molar enthalpy	J/mol
$\mathbf{H}$	Approximate Hessian matrix	
ΔH	Heat/enthalpy of reaction	J/mol
i	Transfer current density of reaction	A/cm^2
	Volumetric charge transfer rate	A/cm^3
$\tilde{I}$	AC current density amplitude	A/cm^2
$\boldsymbol{i}$	Current density	A/cm^2
I	Cell current	A/cm^2
$\boldsymbol{J}$	Flux density relative to mass-average velocity	mol/cm^2 s
k	Thermal conductivity	J/cm^2 K
	Hydraulic permeability	cm^2
	Rate constant of chemical reactions	mol/cm^3 s
	Rate constant of phase change	mol^2/J cm^3 s
L	Thickness	cm
$\mathbf{L}$	Discretized diffusion operator	

Symbol	**Description**	**Unit**
m	Frequency no.	
$\bar{M}$	Molar mass	g/mol
n	Number of electrons transferred	
$\boldsymbol{N}$	Flux	$\mathrm{mol/cm^2\,s}$
p	Total pressure	Pa
q	Surface charge density	$\mathrm{C/m^2}$
$\boldsymbol{q}$	Superficial heat flux	$\mathrm{J/cm^2\,s}$
Q	Heat flux transferred between phases	$\mathrm{J/cm^3\,s}$
r	Rate of reaction per unit of phase interfacial area	$\mathrm{mol/cm^2\,s}$
r	Pore radius	cm
R	Molar gas constant	J/K mol
$\mathcal{R}$	Rate of homogeneous reaction	$\mathrm{mol/cm^3\,s}$
$\Re$	Total reaction rate	$\mathrm{mol/cm^3\,s}$
S	Source term	
	Saturation	
ΔS	Entropy change of reaction	J/K mol
t	Time	s
T	Temperature	K
u	Mobility	$\mathrm{cm^2\,mol/J\,s}$
$\boldsymbol{u}$	Approximated derivative	
$\boldsymbol{v}$	Superficial molar-averaged velocity	cm/s
V	Cell voltage	V
$\bar{V}$	Molar volume	$\mathrm{cm^3/mol}$
W	Compressibility factor	
x	Mole fraction	
	Coordinate	cm
z	Charge number	
Z	Impedance	Ω

A.2.2 Greek

Symbol	Description	Unit
α	Charge transfer coefficient	
	Water transport coefficient	$\mathrm{mol^2/J\,cm\,s}$
β	Reaction symmetry factor	
γ	Water surface tension	N/cm
Γ	General n^{th} order diffusion coefficient	
ϵ	Permittivity	F/cm
ε	Volume fraction	
η	Electrode overpotential	V
	Exergy efficiency	
κ	Protonic conductivity	S/cm
λ	Water content	
$\lambdabar$	Normalized water content	
$\uplambda$	Pore size distribution index	
μ	(Thermodynamic electro-)chemical potential	J/mol
$\upmu$	Viscosity	$\mathrm{Pa\,s}$
ν	Stochiometric coefficient	
ξ	Electroosmotic drag coefficient	
θ	Contact angle	$^\circ$
ϖ	Permeability correction factor for water content	
Π	Peltier coefficient for charge-transfer reaction	V
ρ	Density	$\mathrm{g/cm^3}$
σ	Electronic conductivity	S/cm
$\boldsymbol{\tau}$	Viscous stress tensor	kPa
φ	Regularization tuning parameter	
Φ	Electric potential	V
ψ	General property of system	
Ψ	Gas permeation coefficient	$\mathrm{mol/Pa\,cm\,s}$
ω	Angular frequency	rad/s

A.3 Subscripts and superscripts

0	Medium, solvent
	Standard state
1	Electron conducting phase
2	Proton conducting phase
a	Activation
a	Anode
c	Critical
c	Cathode
C	Capillary
e	Electric charge
E	Electrolyte
f	Final
g	Homogeneous reaction
g	Gauge
G	Gas
h	Electron-transfer reaction
i, j	Species
k, p	Thermodynamic phase
$k \rightarrow p$	Transfer process between phases
K_i	Knudsen (diffusivity)
l	Heterogeneous reaction
L	Liquid water
m	Mixture
n	Iteration no.
ref	Reference value
t	Triple-point of water
T	Thermal
T	Transpose matrix
V	Water vapor
ψ	Related to property ψ
$\circ$	Temperature in °Celsius

Appendix B

Supporting constants and parameters

B.1 Empirical relations for thermodynamical properties of water

Symbol	Equation/value	Unit	Description	Ref.
p_{sat}	$\exp\left[AT^2 + BT + C + D/T\right]$	Pa	Water saturation pressure	[65]
$\bar{M}_{\mathrm{air,corr}}$	$\bar{M}_{\mathrm{air}} + 12.011\left(x_{\mathrm{CO_2}} - 0.0004\right)$	g/mol	Molar mass of air, corrected for mole fraction of CO_2	[65]
W	$1 - \frac{p}{T}(a_0 + a_1 T^{\circ}\ a_2 T^{\circ 2} + (b_0 + b_1)x_{\mathrm{V}} + (c_0 + c_1 T^{\circ})x_{\mathrm{V}}^2) + \frac{p^2}{T^2}\left(d + e x_{\mathrm{V}}^2\right)$		Compressibility factor	[65]
$x_{\mathrm{CO_2}}$	0.004		Reference value for mole fraction of CO_2	[65]
μ	$D_0 \exp\left[\frac{D_1}{T} + D_2 T + D_3 T^2\right]$	Pa s	Viscosity of water	[67]
ρ_{flow}	$\frac{p_{\mathrm{tot,a}}\bar{M}_{\mathrm{air,corr}}}{WRT}\left(1 - x_{\mathrm{V,flow}}\left(1 - \frac{\bar{M}_{\mathrm{H_2O}}}{M_{\mathrm{air,corr}}}\right)\right)$	g/cm^3	Density of moist air	[65]

B.2 Empirical curve fit coefficients

Symbol	**Value**	**Unit**	**Description**	**Ref.**
a_0	$1.58123 \cdot 10^{-6}$	K/Pa	Empirical coefficients for compressibility factor W as a function of pressure p and temperature T.	[65]
a_1	$-2.9331 \cdot 10^{-8}$	1/Pa		[65]
a_2	$1.1043 \cdot 10^{-10}$	1/K Pa		[65]
b_0	$5.707 \cdot 10^{-6}$	K/Pa		[65]
b_1	$-2.051 \cdot 10^{-8}$	1/Pa		[65]
c_0	$1.9898 \cdot 10^{-4}$	K/Pa		[65]
c_1	$-2.376 \cdot 10^{-6}$	1/Pa		[65]
d	$1.83 \cdot 10^{-11}$	K^2/Pa^2		[65]
e	$-0.765 \cdot 10^{-8}$	K^2/Pa^2		[65]
A	$1.2378847 \cdot 10^{-5}$	$1/K^2$	Empirical coefficients for water saturation pressure p_{sat} as a function of temperature T.	[65]
B	$-1.9121316 \cdot 10^{-2}$	1/K		[65]
C	33.93711047			[65]
D	$-6.3431645 \cdot 10^3$	K		[65]
B_0	-0.07636218		Empirical coefficients for correction factor for water uptake effects to gas permeability Ψ_i Arrhenius dependence with temperature T.	This work
B_1	4.85136218			This work
B_2	-8.1441594			This work
B_3	5.74855761			This work
B_4	-1.37877222			This work
C_1	35.12		Empirical coefficients for water content λ vs. water activity a in Nafion.	[24]
C_2	-43.49			[24]
C_3	21.96			[24]
D_0	$1.856 \cdot 10^{-14}$	Pa s	Empirical coefficients for a four-parameter exponential fit of water viscosity μ vs. temperature T.	[67]
D_1	4209	K		[67]
D_2	0.04527	1/K		[67]
D_3	$-3.376 \cdot 10^{-5}$	$1/K^3$		[67]

Bibliography

[1] Z. Abdin, C.J. Webb, and E.MacA. Gray. Modelling and simulation of a proton exchange membrane (PEM) electrolyser cell. *International Journal of Hydrogen Energy*, 40(39):13243–13257, October 2015.

[2] Abdulrahman M. Abomazid, Nader A. El-Taweel, and Hany E. Z. Farag. Novel Analytical Approach for Parameters Identification of PEM Electrolyzer. *IEEE Transactions on Industrial Informatics*, 18(9):5870–5881, September 2022.

[3] K.S. Agbli, M.C. Péra, D. Hissel, O. Rallières, C. Turpin, and I. Doumbia. Multiphysics simulation of a PEM electrolyser: Energetic Macroscopic Representation approach. *International Journal of Hydrogen Energy*, 36(2):1382–1398, January 2011.

[4] F.Z. Aouali, M. Becherif, H.S. Ramadan, M. Emziane, A. Khellaf, and K. Mohammedi. Analytical modelling and experimental validation of proton exchange membrane electrolyser for hydrogen production. *International Journal of Hydrogen Energy*, 42(2):1366–1374, January 2017.

[5] F. Arbabi, H. Montazeri, R. Abouatallah, R. Wang, and A. Bazylak. Three-Dimensional Computational Fluid Dynamics Modelling of Oxygen Bubble Transport in Polymer Electrolyte Membrane Electrolyzer Porous Transport Layers. *Journal of The Electrochemical Society*, 163(11):F3062–F3069, 2016.

[6] F. Aubras, J. Deseure, J.-J.A. Kadjo, I. Dedigama, J. Majasan, B. Grondin-Perez, J.-P. Chabriat, and D.J.L. Brett. Two-dimensional model of low-pressure PEM electrolyser: Two-phase flow regime, electrochemical modelling and experimental validation. *International Journal of Hydrogen Energy*, 42(42):26203–26216, October 2017.

[7] A. Awasthi, Keith Scott, and S. Basu. Dynamic modeling and simulation of a proton exchange membrane electrolyzer for hydrogen production. *International Journal of Hydrogen Energy*, 36(22):14779–14786, November 2011.

[8] Katherine Ayers, Nemanja Danilovic, Ryan Ouimet, Marcelo Carmo, Bryan Pivovar, and Marius Bornstein. Perspectives on Low-Temperature Electrolysis and Potential for Renewable Hydrogen at Scale. *Annual Review of Chemical and Biomolecular Engineering*, page 23, 2019.

[9] Ryan James Balliet. *Modeling Cold Start in a Polymer-Electrolyte Fuel Cell.* PhD thesis, UC Berkeley, 2010.

[10] Frano Barbir. Chapter three - fuel cell electrochemistry. In Frano Barbir, editor, *PEM Fuel Cells (Second Edition)*, pages 33–72. Academic Press, Boston, second edition edition, 2013.

[11] Allen J. Bard and Larry R. Faulkner. Kinetics of electrode reactions. In *Electrochemical Methods: Fundamentals and Applications*, chapter 3, pages 87–136. Wiley, 2nd edition, 2000.

[12] Jose M. Bermudez, Stavrola Evangelopoulou, and Francesco Pavan. Hydrogen. Tracking report, International Energy Agency, 9 rue de la Fédération, 75739 Paris Cedex 15, France, sep 2022. License: CC BY 4.0.

[13] Karel Bouzek. Electroosmosis. In Gustavo F. Wiley, Diane asnd Weihs, editor, *Encyclopedia of Membranes*, page 649. Springer Berlin Heidelberg, Berlin, Heidelberg, 2016.

[14] Justin C. Bui, Eric W. Lees, Lalit M. Pant, Iryna V. Zenyuk, Alexis T. Bell, and Adam Z. Weber. Continuum Modeling of Porous Electrodes for Electrochemical Synthesis. *Chemical Reviews*, 122(12):11022–11084, June 2022.

[15] Marcelo Carmo, David L. Fritz, Jürgen Mergel, and Detlef Stolten. A comprehensive review on PEM water electrolysis. *International Journal of Hydrogen Energy*, 38(12):4901–4934, April 2013.

[16] M. Chandesris, V. Médeau, N. Guillet, S. Chelghoum, D. Thoby, and F. Fouda-Onana. Membrane degradation in PEM water electrolyzer: Numerical modeling and experimental evidence of the influence of temperature and current density. *International Journal of Hydrogen Energy*, 40(3):1353–1366, January 2015.

[17] Rick Chartrand. Numerical differentiation of noisy, nonsmooth data. *International Scholarly Research Notices*, page 11, 2011.

[18] Zhichao Chen, Xueye Wang, Cong Liu, Lingli Gu, Likun Yin, Chao Xu, Zhirong Liao, and Zhiming Wang. Numerical investigation of PEM electrolysis cell with the new interdigitated-jet hole flow field. *International Journal of Hydrogen Energy*, 47(78):33177–33194, September 2022.

[19] Mariana Corengia and Ana I. Torres. Two-phase Dynamic Model for PEM Electrolyzer. In *Computer Aided Chemical Engineering*, volume 44, pages 1435–1440. Elsevier, 2018.

[20] G. Correa, P. Marocco, P. Muñoz, T. Falagüerra, D. Ferrero, and M. Santarelli. Pressurized PEM water electrolysis: Dynamic modelling focusing on the cathode side. *International Journal of Hydrogen Energy*, 47(7):4315–4327, January 2022.

[21] Jian Dang, Fuyuan Yang, Yangyang Li, Yingpeng Zhao, Minggao Ouyang, and Song Hu. Experiments and microsimulation of high-pressure single-cell PEM electrolyzer. *Applied Energy*, 321:119351, September 2022.

[22] D.S. Falcão and A.M.F.R. Pinto. A review on PEM electrolyzer modelling: Guidelines for beginners. *Journal of Cleaner Production*, 261:121184, July 2020.

[23] Julie C. Fornaciari, Michael R. Gerhardt, Jie Zhou, Yagya N. Regmi, Nemanja Danilovic, Alexis T. Bell, and Adam Z. Weber. The Role of Water in Vapor-fed Proton-Exchange-Membrane Electrolysis. *Journal of The Electrochemical Society*, 167(10):104508, jan 2020.

[24] Kevin G Gallagher, Bryan S Pivovar, and Thomas F Fuller. Electro-osmosis and Water Uptake in Polymer Electrolytes in Equilibrium with Water Vapor at Low Temperatures. *Journal of The Electrochemical Society*, page 10, 2009.

[25] Steffen Garbe, Jonas Futter, Thomas J. Schmidt, and Lorenz Gubler. Insight into elevated temperature and thin membrane application for high efficiency in polymer electrolyte water electrolysis. *Electrochimica Acta*, 377:138046, May 2021.

[26] R. García-Valverde, N. Espinosa, and A. Urbina. Simple PEM water electrolyser model and experimental validation. *International Journal of Hydrogen Energy*, 37(2):1927–1938, January 2012.

[27] Michael R. Gerhardt, Lalit M. Pant, Justin C. Bui, Andrew R. Crothers, Victoria M. Ehlinger, Julie C. Fornaciari, Jiangjin Liu, and Adam Z. Weber. Method—Practices and Pitfalls in Voltage Breakdown Analysis of Electrochemical Energy-Conversion Systems. *Journal of The Electrochemical Society*, 168(7):074503, July 2021.

[28] Robert Gloukhovski, Viatcheslav Freger, and Yoed Tsur. Understanding methods of preparation and characterization of pore-filling polymer composites for proton exchange membranes: a beginner's guide. *Reviews in Chemical Engineering*, 34(4):455–479, 2018.

[29] H Gorgun. Dynamic modelling of a proton exchange membrane (PEM) electrolyzer. *International Journal of Hydrogen Energy*, 31(1):29–38, January 2006.

[30] László Gránásy, Tamás Pusztai, David Saylor, and James A. Warren. Phase field theory of heterogeneous crystal nucleation. *Physical Review Letters*, 98:035703, Jan 2007.

[31] S. A. Grigoriev, A. A. Kalinnikov, P. Millet, V. I. Porembsky, and V. N. Fateev. Mathematical modeling of high-pressure PEM water electrolysis. *Journal of Applied Electrochemistry*, 40(5):921–932, May 2010.

[32] Jonathan E. Guyer, Daniel Wheeler, and James A. Warren. FiPy: Partial Differential Equations with Python. *Computing in Science & Engineering*, 11(3):6–15, May 2009.

[33] Bo Han, Jingke Mo, Zhenye Kang, Gaoqiang Yang, William Barnhill, and Feng-Yuan Zhang. Modeling of two-phase transport in proton exchange membrane electrolyzer cells for hydrogen energy. *International Journal of Hydrogen Energy*, 42(7):4478–4489, February 2017.

[34] Alfredo Iranzo, Sergio J. Navas, Felipe Rosa, and Mohamed R. Berber. Determination of time constants of diffusion and electrochemical processes in polymer electrolyte membrane fuel cells. *Energy*, 221:119833, 2021.

[35] Hiroshi Ito, Tetsuhiko Maeda, Akihiro Nakano, and Hiroyasu Takenaka. Properties of nafion membranes under pem water electrolysis conditions. *International Journal of Hydrogen Energy*, 36(17):10527–10540, 2011. International Conference on Hydrogen Production (ICH2P)-2010.

[36] Hiroshi Ito, Naoki Miyazaki, Shota Sugiyama, Masayoshi Ishida, Yuka Nakamura, Shinya Iwasaki, Yasuo Hasegawa, and Akihiro Nakano. Investigations on electrode configurations for anion exchange membrane electrolysis. *Journal of Applied Electrochemistry*, 48:305–316, 2018.

[37] Frédéric Jaouen, Göran Lindbergh, and Katarina Wiezell. Transient Techniques for Investigating Mass-Transport Limitations in Gas Diffusion Electrodes. *Journal of The Electrochemical Society*, 150(12):A1711, 2003.

[38] A.A. Kalinnikov, S.A. Grigoriev, D.G. Bessarabov, and K. Bouzek. Two-phase mass transfer in porous transport layers of the electrolysis cell based on a polymer electrolyte membrane: Analysis of the limitations. *Electrochimica Acta*, 387:138541, August 2021.

[39] Huiyong Kim, Mikyoung Park, and Kwang Soon Lee. One-dimensional dynamic modeling of a high-pressure water electrolysis system for hydrogen production. *International Journal of Hydrogen Energy*, 38(6):2596–2609, February 2013.

[40] Anthony Laconti, Han Liu, Cortney Mittelsteadt, and Robert McDonald. Polymer electrolyte membrane degradation mechanisms in fuel cells - findings over the past 30 years and comparison with electrolyzers. *ECS Transactions*, 1(8):199, jun 2006.

[41] M.E. Lebbal and S. Lecœuche. Identification and monitoring of a PEM electrolyser based on dynamical modelling. *International Journal of Hydrogen Energy*, 34(14):5992–5999, July 2009.

[42] J.K. Lee, Ch. Lee, and A. Bazylak. Pore network modelling to enhance liquid water transport through porous transport layers for polymer electrolyte membrane electrolyzers. *Journal of Power Sources*, 437:226910, October 2019.

[43] Nan Lin and Jochen Zausch. 1D multiphysics modelling of PEM water electrolysis anodes with porous transport layers and the membrane. *Chemical Engineering Science*, 253:117600, May 2022.

[44] Vincenzo Liso, Giorgio Savoia, Samuel Simon Araya, Giovanni Cinti, and Søren Knudsen Kær. Modelling and experimental analysis of a polymer electrolyte membrane water electrolysis cell at different operating temperatures. *Energies*, 11(12), 2018.

[45] Z. Liu. *What Is Multiphysics*, chapter 2, pages 9–20. Springer International Publishing, Cham, 2018.

[46] Paul W. Majsztrik, M. Barclay Satterfield, Andrew B. Bocarsly, and Jay B. Benziger. Water sorption, desorption and transport in nafion membranes. *Journal of Membrane Science*, 301(1):93–106, 2007.

[47] Jakub Mališ, Petr Mazúr, Martin Paidar, Tomas Bystron, and Karel Bouzek. Nafion 117 stability under conditions of pem water electrolysis at elevated temperature and pressure. *International Journal of Hydrogen Energy*, 41(4):2177–2188, 2016.

[48] F Marangio, M Santarelli, and M Cali. Theoretical model and experimental analysis of a high pressure PEM water electrolyser for hydrogen production. *International Journal of Hydrogen Energy*, 34(3):1143–1158, February 2009.

[49] Agate Martin, Patrick Trinke, Markus Stähler, Andrea Stähler, Fabian Scheepers, Boris Bensmann, Marcelo Carmo, Werner Lehnert, and Richard Hanke-Rauschenbach. The Effect of Cell Compression and Cathode Pressure on Hydrogen Crossover in PEM Water Electrolysis. *Journal of The Electrochemical Society*, 169(1):014502, January 2022.

[50] J. Mazur. Numerical simulation of temperature field in soil generated by solar radiation. *Journal de Physique IV France*, 137:317–320, Dec 2007.

[51] G.R. Molaeimanesh and M.H. Akbari. Agglomerate modeling of cathode catalyst layer of a PEM fuel cell by the lattice Boltzmann method. *International Journal of Hydrogen Energy*, 40(15):5169–5185, April 2015.

[52] Faeze Moradi Nafchi, Ebrahim Afshari, Ehsan Baniasadi, and Nader Javani. A parametric study of polymer membrane electrolyser performance, energy and exergy analyses. *International Journal of Hydrogen Energy*, 44(34):18662–18670, July 2019.

[53] Timothy D. Myles, George J. Nelson, Aldo A. Peracchio, Robert J. Roy, Bryan L. Murach, Gary A. Adamson, and Wilson K.S. Chiu. Species transport in a high-pressure oxygen-generating proton-exchange membrane electrolyzer. *International Journal of Hydrogen Energy*, 37(17):12451–12463, September 2012.

[54] John Newman and Karen E. Thomas-Alyea. *Electrochemical Systems*, chapter 22, pages 517–565. Wiley, 3rd edition, 2004.

[55] John Newman and Karen E. Thomas-Alyea. *Electrochemical Systems*, chapter 8, pages 203–239. Wiley, 3rd edition, 2004.

[56] John Newman and William Tiedemann. Porous-electrode theory with battery applications. *AIChE Journal*, 21(1):25–41, January 1975.

[57] Meng Ni, Michael K.H. Leung, and Dennis Y.C. Leung. Energy and exergy analysis of hydrogen production by a proton exchange membrane (PEM) electrolyzer plant. *Energy Conversion and Management*, 49(10):2748–2756, October 2008.

[58] L.J. Nuttall, A.P. Fickett, and W.A. Titterington. Hydrogen Generation by Solid Polymer Electrolyte Water Electrolysis. In Turhan N. Veziroğlu, editor, *Hydrogen Energy*, pages 441–455, Boston, MA, 1975. The Hydrogen Economy Miami Energy (THEME) Conference, Springer, US.

[59] Emile Tabu Ojong, Jason Tai Hong Kwan, Amin Nouri-Khorasani, Arman Bonakdarpour, David P. Wilkinson, and Tom Smolinka. Development of an experimentally validated semi-empirical fully-coupled performance model of a PEM electrolysis cell with a 3-D structured porous transport layer. *International Journal of Hydrogen Energy*, 42(41):25831–25847, October 2017.

[60] Luiz F.L. Olivieira, Christian Jallut, and Alejandro A. Franco. A multiscale physical model of a polymer electrolyte membrane water electrolyzer. *Electrochimica Acta*, 110:363–374, 2013.

[61] Pierre Olivier, Cyril Bourasseau, and Belkacem Bouamama. Dynamic and multiphysic PEM electrolysis system modelling: A bond graph approach. *International Journal of Hydrogen Energy*, 42(22):14872–14904, June 2017.

[62] Pierre Olivier, Cyril Bourasseau, and Pr. Belkacem Bouamama. Low-temperature electrolysis system modelling: A review. *Renewable and Sustainable Energy Reviews*, 78:280–300, October 2017.

[63] Kazuo Onda, Toshio Murakami, Takeshi Hikosaka, Misaki Kobayashi, Ryouhei Notu, and Kohei Ito. Performance Analysis of Polymer-Electrolyte Water Electrolysis Cell at a Small-Unit Test Cell and Performance Prediction of Large Stacked Cell. *Journal of The Electrochemical Society*, 149(8):A1069, 2002.

[64] Stephen J. Paddison, David W. Reagor, and Thomas A. Zawodzinski Jr. High frequency dielectric studies of hydrated nafion®. *Journal of Electroanalytical Chemistry*, 459(1):91–97, 1998.

[65] A Picard, R S Davis, M Gläser, and K Fujii. Revised formula for the density of moist air (CIPM-2007). *Metrologia*, 45(2):149–155, April 2008.

[66] A. Rajora and J.W. Haverkort. An Analytical Model for Liquid and Gas Diffusion Layers in Electrolyzers and Fuel Cells. *Journal of the Electrochemical Society*, 168:034506, 2021.

[67] R C Reid, J M Prausnitz, and B E Poling. *The properties of gases and liquids.* U.S. Department of Energy, Office of Scientific and Technical Information, 4 edition, 1 1987.

[68] Markus Sartory, Eva Wallnöfer-Ogris, Patrick Salman, Thomas Fellinger, Markus Justl, Alexander Trattner, and Manfred Klell. Theoretical and experimental analysis of an asymmetric high pressure PEM water electrolyser up to 155 bar. *International Journal of Hydrogen Energy*, 42(52):30493–30508, December 2017.

[69] Maximilian Schalenbach, Tobias Hoefner, Paul Paciok, Marcelo Carmo, Wiebke Lueke, and Detlef Stolten. Gas Permeation through Nafion. Part 1: Measurements. *The Journal of Physical Chemistry C*, 119(45):25145–25155, November 2015.

[70] Maximilian Schalenbach, Michael A. Hoeh, Jeff T. Gostick, Wiebke Lueke, and Detlef Stolten. Gas Permeation through Nafion. Part 2: Resistor Network Model. *The Journal of Physical Chemistry C*, 119(45):25156–25169, November 2015.

[71] S. Siracusano, N. Van Dijk, R. Backhouse, L. Merlo, V. Baglio, and A.S. Aricò. Degradation issues of PEM electrolysis MEAs. *Renewable Energy*, 123:52–57, August 2018.

[72] Tom Smolinka, Emile Tabu Ojong, and Thomas Lickert. Fundamentals of PEM Water Electrolysis. *PEM Electrolysis for Hydrogen Production*, page 23, 2016.

[73] Camillo Spöri, Jason Tai Hong Kwan, Arman Bonakdarpour, David P. Wilkinson, and Peter Strasser. The stability challenges of oxygen evolving catalysts: Towards a common fundamental understanding and mitigation of catalyst degradation. *Angewandte Chemie International Edition*, 56(22):5994–6021, 2017.

[74] Michel Suermann, Boris Bensmann, and Richard Hanke-Rauschenbach. Degradation of Proton Exchange Membrane (PEM) Water Electrolysis Cells: Looking Beyond the Cell Voltage Increase. *Journal of The Electrochemical Society*, 166(10):F645–F652, 2019.

[75] Pang-Chieh Sui, Xun Zhu, and Ned Djilali. Modeling of PEM Fuel Cell Catalyst Layers: Status and Outlook. *Electrochemical Energy Reviews*, 2(3):428–466, September 2019.

[76] Magnus S. Thomassen and Alejandro Oyarce Barnett. A method for producing hydrogen in a pem water electrolyser system, pem water electrolyser cell, stack and system, jan 2019.

[77] Magnus S. Thomassen, Anita H. Reksten, Alejandro O. Barnett, Thulile Khoza, and Kathy Ayers. Chapter 6 - pem water electrolysis. In Tom Smolinka and Jurgen Garche, editors, *Electrochemical Power Sources: Fundamentals, Systems, and Applications*, pages 199–228. Elsevier, 2022.

[78] Cécile Vallieres, Dirk Winkelmann, Denis Doizard, Eric Favre, Philip Scharfer, and Matthias Kind. On Schroeder's paradox. *Journal of Membrane Science*, 278(1–2):357–364, 2006.

[79] Curtis R. Vogel. Chapter 8 - total variation regularization. In *Computational Methods for Inverse Problems*. Society for Industrial and Applied Mathematics, 2002.

[80] C Y Wang and P Cheng. A multiphase mixture model for multiphase, multicomponent transport in capillary porous media I. Model development. *International Journal of Heat Mass Transfer*, 1996.

[81] Adam Z. Weber, Ryan Balliet, Haluna P. Gunterman, and John Newman. *Modeling Water Management in Polymer-Electrolyte Fuel Cells*, pages 273–415. Springer New York, New York, NY, 2009.

[82] Adam Z. Weber, Rodney L. Borup, Robert M. Darling, Prodip K. Das, Thomas J. Dursch, Wenbin Gu, David Harvey, Ahmet Kusoglu, Shawn Litster, Matthew M. Mench, Rangachary Mukundan, Jon P. Owejan, Jon G. Pharoah, Marc Secanell, and Iryna V. Zenyuk. A Critical Review of Modeling Transport Phenomena in Polymer-Electrolyte Fuel Cells. *Journal of The Electrochemical Society*, 161(12):F1254–F1299, 2014.

[83] Adam Z. Weber and John Newman. Modeling Transport in Polymer-Electrolyte Fuel Cells. *Chemical Reviews*, 104(10):4679–4726, October 2004.

[84] Adam Z Weber and John Newman. Transport in Polymer-Electrolyte Membranes. *Journal of The Electrochemical Society*, page 15, 2004.

[85] Adam Z Weber and John Newman. Transport in Polymer-Electrolyte Membranes. *Journal of The Electrochemical Society*, page 9, 2004.

[86] Katarina Wiezell, Peter Gode, and Göran Lindbergh. Steady-State and EIS Investigations of Hydrogen Electrodes and Membranes in Polymer Electrolyte Fuel Cells. *Journal of The Electrochemical Society*, page 11, 2006.

[87] Katarina Wiezell, Nicklas Holmström, and Göran Lindbergh. Studying Low-Humidity Effects in PEFCs Using EIS II. Modeling. *Journal of The Electrochemical Society*, 159(8):F379–F392, 2012.

[88] Lei Xing. An agglomerate model for PEM fuel cells operated with non-precious carbon-based ORR catalysts. *Chemical Engineering Science*, 179:198–213, April 2018.

[89] Qingrong Xiong, Todor G. Baychev, and Andrey P. Jivkov. Review of pore network modelling of porous media: Experimental characterisations, network constructions and applications to reactive transport. *Journal of Contaminant Hydrology*, 192:101–117, September 2016.

[90] H.L. Yeager and A. Steck. Cation and Water Diffusion in Nafion Ion Exchange Membranes: Influence of Polymer Structure. *Journal of the Electrochemical Society*, 128:1880–1884, 1981.

[91] Iryna V. Zenyuk, Prodip K. Das, and Adam Z. Weber. Understanding Impacts of Catalyst-Layer Thickness on Fuel-Cell Performance via Mathematical Modeling. *Journal of The Electrochemical Society*, 163(7):F691–F703, 2016.

[92] Li-Yu Zhu, Yu-Cheng Li, Jing Liu, Jing He, Lu-Ying Wang, and Jian-Du Lei. Recent developments in high-performance nafion membranes for hydrogen fuel cells applications. *Petroleum Science*, 19(3):1371–1381, 2022.

[93] S.S. Zumdahl. Factors affecting solubility. In Cathy Labresh Brooks, editor, *Chemical Principles*, pages 855–856. Brooks/Cole, New York, NY, 2009.

NTNU

Norwegian University of
Science and Technology